



# Politecnico di Bari

Repository Istituzionale dei Prodotti della Ricerca del Politecnico di Bari

Study of thermo-acoustic instability in gas turbine combustion system fueled by methane enriched with hydrogen

This is a PhD Thesis

*Original Citation:*

Study of thermo-acoustic instability in gas turbine combustion system fueled by methane enriched with hydrogen / Ceglie, Vito. - ELETTRONICO. - (2023). [10.60576/poliba/iris/ceglie-vito\_phd2023]

*Availability:*

This version is available at <http://hdl.handle.net/11589/254940> since: 2023-06-21

*Published version*

<http://hdl.handle.net/11589/254940>  
DOI: 10.60576/poliba/iris/ceglie-vito\_phd2023

*Terms of use:*

Altro tipo di accesso

(Article begins on next page)



Politecnico  
di Bari

DEPARTMENT OF MECHANICS, MATHEMATICS AND  
MANAGEMENT

MECHANICAL AND MANAGEMENT ENGINEERING  
PH.D. PROGRAM

SSD: ING-IND/08 - FLUID MACHINERY

Final dissertation

---

**Study of thermo-acoustic instability in  
gas turbine combustion system fueled by  
methane enriched with hydrogen**

---

by  
VITO CEGLIE

Supervisors:  
Prof. Sergio Mario CAMPOREALE  
Prof. Marco TORRESI

*Coordinator of the Ph.D. Program:*  
*Prof. Giuseppe P. Demelio*

---

*Course XXXV, 01/11/2019 - 31/01/2023*

LIBERATORIA PER L'ARCHIVIAZIONE DELLA TESI DI DOTTORATO

Al Magnifico Rettore  
del Politecnico di Bari

Il sottoscritto VITO CEGLIE nato a BARI il 07/12/1986 residente a BARI in VIA GIUSEPPE DE MARINIS, 123 e-mail vito.ceglie@poliba.it iscritto al 3° anno di Corso di Dottorato di Ricerca in INGEGNERIA MECCANICA E GESTIONALE ciclo XXXV ed essendo stato ammesso a sostenere l'esame finale con la prevista discussione della tesi dal titolo:

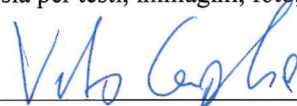
**Study of thermo-acoustic instability in a gas turbine combustion system fueled by methane enriched with hydrogen.**

**DICHIARA**

- 1) di essere consapevole che, ai sensi del D.P.R. n. 445 del 28.12.2000, le dichiarazioni mendaci, la falsità negli atti e l'uso di atti falsi sono puniti ai sensi del codice penale e delle Leggi speciali in materia, e che nel caso ricorressero dette ipotesi, decade fin dall'inizio e senza necessità di nessuna formalità dai benefici conseguenti al provvedimento emanato sulla base di tali dichiarazioni;
- 2) di essere iscritto al Corso di Dottorato di ricerca INGEGNERIA MECCANICA E GESTIONALE ciclo XXXV corso attivato ai sensi del "Regolamento dei Corsi di Dottorato di ricerca del Politecnico di Bari", emanato con D.R. n.286 del 01.07.2013;
- 3) di essere pienamente a conoscenza delle disposizioni contenute nel predetto Regolamento in merito alla procedura di deposito, pubblicazione e autoarchiviazione della tesi di dottorato nell'Archivio Istituzionale ad accesso aperto alla letteratura scientifica;
- 4) di essere consapevole che attraverso l'autoarchiviazione delle tesi nell'Archivio Istituzionale ad accesso aperto alla letteratura scientifica del Politecnico di Bari (IRIS-POLIBA), l'Ateneo archiverà e renderà consultabile in rete (nel rispetto della Policy di Ateneo di cui al D.R. 642 del 13.11.2015) il testo completo della tesi di dottorato, fatta salva la possibilità di sottoscrizione di apposite licenze per le relative condizioni di utilizzo (di cui al sito <http://www.creativecommons.it/Licenze>), e fatte salve, altresì, le eventuali esigenze di "embargo", legate a strette considerazioni sulla tutelabilità e sfruttamento industriale/commerciale dei contenuti della tesi, da rappresentarsi mediante compilazione e sottoscrizione del modulo in calce (Richiesta di embargo);
- 5) che la tesi da depositare in IRIS-POLIBA, in formato digitale (PDF/A) sarà del tutto identica a quelle **consegnate**/inviata/da inviarsi ai componenti della commissione per l'esame finale e a qualsiasi altra copia depositata presso gli Uffici del Politecnico di Bari in forma cartacea o digitale, ovvero a quella da discutere in sede di esame finale, a quella da depositare, a cura dell'Ateneo, presso le Biblioteche Nazionali Centrali di Roma e Firenze e presso tutti gli Uffici competenti per legge al momento del deposito stesso, e che di conseguenza va esclusa qualsiasi responsabilità del Politecnico di Bari per quanto riguarda eventuali errori, imprecisioni o omissioni nei contenuti della tesi;
- 6) che il contenuto e l'organizzazione della tesi è opera originale realizzata dal sottoscritto e non compromette in alcun modo i diritti di terzi, ivi compresi quelli relativi alla sicurezza dei dati personali; che pertanto il Politecnico di Bari ed i suoi funzionari sono in ogni caso esenti da responsabilità di qualsivoglia natura: civile, amministrativa e penale e saranno dal sottoscritto tenuti indenni da qualsiasi richiesta o rivendicazione da parte di terzi;
- 7) che il contenuto della tesi non infrange in alcun modo il diritto d'Autore né gli obblighi connessi alla salvaguardia di diritti morali od economici di altri autori o di altri aventi diritto, sia per testi, immagini, foto, tabelle, o altre parti di cui la tesi è composta.

Bari, 17/04/2023

Firma



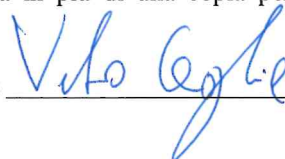
Il sottoscritto, con l'autoarchiviazione della propria tesi di dottorato nell'Archivio Istituzionale ad accesso aperto del Politecnico di Bari (POLIBA-IRIS), pur mantenendo su di essa tutti i diritti d'autore, morali ed economici, ai sensi della normativa vigente (Legge 633/1941 e ss.mm.ii.),

**CONCEDE**

- al Politecnico di Bari il permesso di trasferire l'opera su qualsiasi supporto e di convertirla in qualsiasi formato al fine di una corretta conservazione nel tempo. Il Politecnico di Bari garantisce che non verrà effettuata alcuna modifica al contenuto e alla struttura dell'opera.
- al Politecnico di Bari la possibilità di riprodurre l'opera in più di una copia per fini di sicurezza, back-up e conservazione.

Bari, 17/04/2023

Firma





Politecnico  
di Bari

DEPARTMENT OF MECHANICS, MATHEMATICS AND  
MANAGEMENT

MECHANICAL AND MANAGEMENT ENGINEERING  
PH.D. PROGRAM

SSD: ING-IND/08 - FLUID MACHINERY

Final dissertation

---

## Study of thermo-acoustic instability in gas turbine combustion system fueled by methane enriched with hydrogen

---

by  
VITO CEGLIE

Referees:

Prof. Maria Cristina CAMERETTI  
Prof. Aldo BONFIGLIOLI

Supervisors:

Prof. Sergio Mario CAMPOREALE

Prof. Marco TORRESI

*Coordinator of the Ph.D. Program:*  
Prof. Giuseppe P. Demelio

---

Course XXXV, 01/11/2019 - 31/01/2023



# Sommario

Negli ultimi anni si sta tentando sempre più di utilizzare l'idrogeno come combustibile nei bruciatori progettati per funzionare con miscele di aria e metano. L'uso dell'idrogeno nelle turbine a gas è una delle soluzioni tecniche più promettenti per ottenere una combustione sostenibile durante la transizione verso un futuro carbon-free. L'interesse della ricerca accademica e industriale per l'idrogeno deriva dal fatto che è un combustibile privo di carbonio e per le sue proprietà, quali un LHV più elevato e limiti di infiammabilità maggiori rispetto agli altri idrocarburi convenzionali. Nonostante questi aspetti, ci sono ancora diverse questioni tecniche fondamentali che devono essere affrontate, come il potenziale ritorno di fiamma e l'autoaccensione a causa delle velocità di fiamma significativamente più elevata e dei tempi di autoaccensione più brevi. Inoltre, con l'idrogeno possono verificarsi instabilità di combustione in corrispondenza di punti di funzionamento ultra-lean. È importante poter prevedere in fase di progettazione il comportamento di un bruciatore alimentato a idrogeno per evitare questi fenomeni deleteri. L'obiettivo di questa tesi è quello di simulare il comportamento termoacustico di bruciatori di turbine a gas alimentati con combustibili arricchiti con idrogeno. Le simulazioni numeriche vengono realizzate risolvendo il problema nel dominio delle frequenze con l'approccio del solutore di Helmholtz. Inizialmente, è stata sviluppata una procedura numerica basata sulla combinazione di un solutore di Helmholtz e di una legge di fiamma lineare con l'introduzione del flusso medio. In questo contesto, è stato condotto uno studio di sensibilità dell'instabilità termoacustica variando il numero di Mach ( $M$ ), che rappresenta la velocità impostata all'inlet del bruciatore. La seconda parte di questa tesi confronta le simulazioni CFD di vari blend di combustibili eseguite su bruciatori di turbine a gas in scala di laboratorio e sul bruciatore della microturbina a gas (mGT) AE-T100. Come bruciatori in scala di laboratorio sono stati scelti il bruciatore premixed swirlato sviluppato alla Louisiana State University e il bruciatore premixed stabilizzato tramite bluff body studiato alla Vanderbilt University. Questi due bruciatori di laboratorio, che presentano ciascuno un metodo di stabilizzazione della fiamma differente, sono risultati i più adatti all'aggiunta di idrogeno alla miscela. Sul primo bruciatore, sono state sviluppate simulazioni URANS per confrontare la miscela aria metano e la miscela metano arricchita di idrogeno in termini di distribuzione del rapporto di equivalenza, della velocità e degli inquinanti. Le simulazioni RANS del bruciatore Vanderbilt alimentato con miscele di metano puro e idrogeno puro sono state effettuate per confrontare le risposte fluidodinamiche dei due sistemi. Quest'ultima attività è stata svolta in collaborazione con Ansaldo Energia. La simulazione CFD sul bruciatore della microturbina a gas AE-T100 è stata eseguita con miscele metano-aria,  $90\%_v CH_4 - 10\%_v H_2$  e  $70\%_v CH_4 - 30\%_v H_2$ . Le simulazioni sul bruciatore della microturbina a gas AE-T100 sono state sviluppate, durante il periodo di visiting research del mio corso di dottorato, in collaborazione con la "Thermal Engineering and Combustion Unit" dell'Università di MONS, in partico-



# Abstract

In recent years, more and more efforts are being made toward the use of hydrogen as a fuel in burners designed to work with methane-air mixtures. The use of hydrogen in gas turbines is one of the most promising technical solutions to obtain sustainable combustion during the transition toward a carbon-free future. Interest by academic and industrial research in hydrogen derives from its being a carbon-free fuel and its properties such as higher Lower Heating Value (LHV) and wider flammability limits with respect to other conventional hydrocarbons. Despite these aspects, there are still several challenging technical issues that must be addressed such as the potential flashback and autoignition due to the significantly higher flame speeds and shorter autoignition times. Furthermore, combustion instabilities may occur toward ultra-lean operating points with hydrogen. It is important to be able to predict the behavior of a burner fueled with hydrogen in order to avoid these deleterious phenomena during the design phase. The objective of this thesis is to predict the thermo-acoustic behavior of gas turbine burner with hydrogen enriched fuels. The numerical simulations are performed by solving the problem in the frequency domain using the Helmholtz solver approach. At first, the numerical procedure relying on the combination of a Helmholtz solver and a linear flame law with the introduction of the mean flow has been developed. In this framework, a sensitivity study of the thermo-acoustic instability by varying the Mach number ( $M$ ), which represents the velocity set at the burner inlet, has been carried out. The second section compares CFD simulations of various fuel combinations performed on laboratory-scale gas turbine burners and on the burner of the micro gas turbine (mGT) AE-T100. The swirled premixed burner developed at Louisiana State University and the bluff body stabilized premixed burner investigated at Vanderbilt University have been selected as laboratory-scale burners. These two laboratory burners, each with its own flame stabilization mechanism, have been demonstrated to be the most effective for adding hydrogen to the mixture. On the first burner, URANS simulations were used to compare the methane-air mixture and the methane enriched with hydrogen blend in terms of equivalence ratio distribution, velocities, and pollutants. RANS simulations of the Vanderbilt burner fueled by pure methane and pure hydrogen mixtures have been developed in order to compare the fluid-dynamic responses of two systems. This last activity has been performed in collaboration with Ansaldo Energia. The CFD simulation on the burner of the AE-T100 micro gas turbine has been performed with methane-air mixtures of  $90\%_v CH_4 - 10\%_v H_2$  and  $70\%_v CH_4 - 30\%_v H_2$ . The simulations on the burner of AE-T100 micro gas turbine have been performed, during the visiting research period of my PhD course, in partnership with the Thermal Engineering and Combustion Unit of the University of MONS, and in particular with professor Ward De Paepe, and researchers Jérémy Bompas, and Alessio Pappa. Finally, the results of CFD simulations of Vanderbilt burner and AE-T100 burner, namely gaseous thermodynamic



properties and time delay fields, have been used to perform a FEM analysis with the commercial code COMSOL Multiphysics<sup>®</sup> by applying a general flame response function ( $n$ - $\tau$  model). In this framework, an analysis of the physics that leads the thermoacoustic driving mechanism for each burner has been carried out with particular attention on the method of estimation of the time delay  $\tau$ .

# Contents

<b>List of Figures</b>	<b>xiii</b>
<b>List of Tables</b>	<b>xvi</b>
<b>List of Symbols</b>	<b>xvii</b>
<b>Introduction</b>	<b>1</b>
<b>1 Hydrogen as a green fuel in gas turbines</b>	<b>5</b>
1.1 Hydrogen in carbon-free economy . . . . .	5
1.2 Hydrogen - methane blend in gas turbine . . . . .	5
1.2.1 Influence of Hydrogen on structure and flame position . . . . .	6
1.2.2 Effect on Thermo-acoustic stability of the system . . . . .	7
1.2.3 Effect on Flashback . . . . .	9
<b>2 Description of thermo-acoustic instability</b>	<b>11</b>
2.1 Rayleigh Criterion . . . . .	11
2.1.1 Thermodynamic Rayleigh Criterion . . . . .	12
2.2 Driving mechanisms . . . . .	13
2.3 Instability damping mechanism . . . . .	15
2.4 Linear and nonlinear stability . . . . .	16
<b>3 Thermo-acoustic mathematical models of combustion instability</b>	<b>19</b>
3.1 Time domain equations . . . . .	19
3.2 Frequency domain equations . . . . .	21
3.3 Flame Response Function (FRF) . . . . .	22
3.3.1 Eigenvalue analysis . . . . .	22
3.4 Mathematical models and Solutions procedures . . . . .	23
3.4.1 Low-order model approach . . . . .	24
3.4.2 Finite Elements method approach . . . . .	25
3.4.3 Computational Fluid Dynamic approach . . . . .	25
3.5 Influence of mean flow . . . . .	26
3.5.1 Mean flow in Low Order solver . . . . .	27
3.5.2 Numerical setup in Helmholtz solver . . . . .	28
3.5.3 Numerical validation on simple cylinder . . . . .	30
3.5.4 Numerical setup on annular combustor . . . . .	32
3.5.5 Results of the annular combustor . . . . .	33

<b>4</b>	<b>Computational Fluid Dynamic (CFD) mathematical models</b>	<b>35</b>
4.1	Computational Fluid Dynamic (CFD) simulations . . . . .	35
4.1.1	Mathematical basis of CFD . . . . .	35
4.1.2	Solution approach to turbulent flows . . . . .	38
4.1.3	Combustion Model: Partially premixed . . . . .	38
4.1.4	Turbulent flame speed: Zimont model . . . . .	42
<b>5</b>	<b>CFD Simulations of burners fueled by methane and hydrogen</b>	<b>43</b>
5.1	Premixed Louisiana Laboratory burner . . . . .	43
5.1.1	Numerical setup . . . . .	44
5.1.2	Boundary conditions of non reacting flow . . . . .	47
5.1.3	Boundary conditions of reacting flow . . . . .	47
5.1.4	Grid refinement . . . . .	48
5.1.5	Non reacting flow results . . . . .	50
5.1.6	Comparison between 100% $CH_4$ mixture vs 70% $CH_4$ - 30% $H_2$ blends	54
5.2	Premixed Vanderbilt Bluff body stabilized Laboratory Burner . . . . .	64
5.2.1	Numerical setup . . . . .	64
5.2.2	Boundary conditions . . . . .	65
5.2.3	Grid refinement . . . . .	66
5.2.4	Turbulence model assessment . . . . .	67
5.2.5	Comparison between 100% $CH_4$ vs 100% $H_2$ mixture . . . . .	69
<b>6</b>	<b>Thermo-acoustic analysis</b>	<b>75</b>
6.1	Boundary conditions and Grid refinement . . . . .	75
6.2	Numerical setup of Helmholtz solver Simulations . . . . .	77
6.3	Comparison between 100% $CH_4$ vs 100% $H_2$ mixture . . . . .	82
<b>7</b>	<b>Application on micro-turbine AE-T100</b>	<b>87</b>
7.1	AE T100 Micro-Turbine Burner . . . . .	87
7.2	Numerical setup of CFD Simulations . . . . .	89
7.2.1	CFD Grid refinement . . . . .	90
7.3	CFD comparison between 100% $CH_4$ mixture vs $H_2$ - $CH_4$ blends . . . . .	92
7.4	Natural frequencies of the AE-T100 burner . . . . .	93
7.5	Numerical setup of Low Order solver . . . . .	95
7.6	Validation of Helmholtz solver . . . . .	97
7.7	Numerical setup of Helmholtz solver Simulations . . . . .	100
7.8	Thermo-acoustic comparison between 100% $CH_4$ mixture vs $H_2$ - $CH_4$ blends . . . . .	102
	<b>Conclusions</b>	<b>105</b>
	<b>References</b>	<b>116</b>
	<b>Publications</b>	<b>117</b>
	<b>Acknowledgment</b>	<b>119</b>

# List of Figures

1.1	$CH^*$ chemiluminescence flame images and stability map for (a) natural gas and (b) 25% $H_2 - CH_4$ mixtures cases. Inlet temperature is 200 °C and inlet bulk velocity is 75 m/s for each case (reprinted from [31]). . . .	6
1.2	Comparison flame shape transition between pure methane 10% and 20% hydrogen by volume blend in function of equivalence ratio (reprinted from [33]). . . . .	7
1.3	Sensibility on hydrogen enrichment of gain (a) and phase (b) of FTF at low forcing amplitude. Operating conditions: bulk velocity = 60 m/s, inlet temperature = 200°C and equivalence ratio = 0.6 (reprinted from [37]).	8
1.4	Spectra of heat release, pressure and flashback at $\phi = 0.7$ . Flashback was induced by combustion instabilities (reprinted from [47]). . . . .	9
2.1	The principal feedback process responsible of thermo-acoustic combustion instabilities (reprinted from [49]). . . . .	11
2.2	Thermodynamic interpretation of the Rayleigh criterion. . . . .	13
2.3	Driving mechanism of thermoacoustic instability in gas turbine burner (reprinted from [49]). . . . .	14
2.4	Influence of delayed responses of various combustor processes to a periodic pressure disturbance (reprinted from [49]). . . . .	15
2.5	Energy gain and acoustic losses in a thermoacoustic system forced with a sinusoidal signal of frequency $\omega$ and increasing amplitude $ u'/u $ (reprinted from [64]). . . . .	16
3.1	Classification of tools to solve the thermo-acoustic problem (inspired by [71]). . . . .	23
3.2	Detail of one-dimensional bench-mark geometry adapted by [63]. The gray section represents the flame sheet. . . . .	28
3.3	Settings of OSCILOS Simulator.(a) Geometry of bench-mark burner (b) trend of temperature and velocity with length . . . . .	28
3.4	Comparison between COMSOL and OSCILOS of unstable mode: (a) Frequency, (b) Growth Rate . . . . .	31
3.5	Comparison between COMSOL and OSCILOS of stable mode: (a) Frequency, (b) Growth Rate . . . . .	31
3.6	Geometry of annular combustor . . . . .	32
3.7	Unstructured grid of Annular combustor: (a) 68601 tetrahedron elements, (b) 131671 tetrahedron elements, (c) 183515 tetrahedron elements . . . .	33
3.8	Trend of Frequency and Growth Rate in Annular Model . . . . .	34

4.1	Graphical representation of a generic volume $V$ and the generic conservation equation of an extensive physical quantity $\Psi$ . . . . .	36
4.2	Visual Representation of a Look-Up Table for the Scalar $\bar{\psi}_i$ as a Function of $\bar{\xi}$ and $\bar{\xi}'^2$ and $\bar{h}$ in Non-Adiabatic in chemical equilibrium Systems. . .	41
5.1	Isometric view of the Louisiana State University swirled premixed burner.	44
5.2	Axial section of the Louisiana State University swirled premixed burner. .	45
5.3	Axial swirler of the Louisiana State University swirled premixed burner. .	45
5.4	Louisiana burner: (a) fuel injection holes (dimension in [mm]) (b) Isometric view center body. The injection holes are located backward of the cross section restriction. . . . .	46
5.5	Computational domain Louisiana burner (a) isometric computational geometry (b) axial section computational geometry with combustion zone dimensions . . . . .	46
5.6	Boundary condition inlet section non reacting flow Louisiana burner . . .	47
5.7	Boundary conditions used when simulating non reacting flow Louisiana burner (a) outlet section (b) combustion zone surface . . . . .	47
5.8	Pathlines tangential velocity in the duct of center body in the case of reacting flow. . . . .	49
5.9	Refinement in swirler zone. . . . .	50
5.10	Inflation (a) in the duct of center body downstream the swirler (b) details of inflation on longitudinal variations of section . . . . .	50
5.11	Face size injectors. . . . .	50
5.12	Comparison for different meshes between numerical and experimental normalized mean axial velocity profiles, $u/u_0$ , for non-reacting flow, at different axial locations ( $x = 20$ mm (a), $x = 30$ mm (b), $x = 40$ mm (c)) . . . . .	51
5.13	Monitoring points downstream dump plane. . . . .	52
5.14	Comparison between numerical and experimental normalized mean axial velocity profiles, $u/u_0$ for non-reacting flow, at different axial locations ( $x = 20$ mm (a), $x = 30$ mm (b), $x = 40$ mm (c)). . . . .	52
5.15	Comparison between numerical and experimental normalized mean tangential velocity profiles, $u/u_0$ for non-reacting flow, at different axial locations ( $x = 20$ mm (a), $x = 30$ mm (b), $x = 40$ mm (c)). . . . .	53
5.16	Contours on longitudinal plane of:(a) Mean axial velocity, $u$ , with identification of Wake Recirculation Zone (WRZ), Corner Recirculation Zone (CRZ) and Toroidal Recirculation Zone (CTRZ) and the zero-axial velocity isolines in the longitudinal plane of the burner; (b) Vorticity magnitude.	53
5.17	Power Spectral Density (PSD) for the axial velocity signals at different axial locations. . . . .	54
5.18	Iso-vorticity magnitude surface( $\omega = 1000$ s <sup>-1</sup> ). . . . .	54
5.19	Comparison of the mean contours of the equivalence ratio, $\phi$ , between pure methane (left) and methane-hydrogen mixture (right) combustion case (evaluated at the cross section located at 1 mm upstream of the dump plane. . . . .	56

5.20	Mean radial distribution (sampling time= 3 s) of equivalence ratio $\phi$ (cyan line is equal to $\phi = 0.7$ ) in burner's cross section located at 1 mm upstream the dump plane: (a) burner fueled by 100%v $CH_4$ , (b) burner fueled by 70%v $CH_4 + 30\%v H_2$ . . . . .	56
5.21	Burner fueled by 100%v $CH_4$ -air mixture. Comparison of the mean profiles, normalized with respect to the bulk velocity $u_0 = 11.826$ m/s, of axial velocities $u/u_0$ (sampling time $T = 2$ s), between URANS simulations with and without radiation model (DO) and LES and experimental results of [106] at different axial locations ( $x = 20$ mm (a), $x = 30$ mm (b), $x = 40$ mm (c)) . . . . .	58
5.22	Burner fueled by 100%v $CH_4$ mixture. Comparison of the mean profiles, normalized with respect to the bulk velocity $u_0 = 11.826$ m/s, of tangential velocities $w/u_0$ (sampling time $T = 2$ s), between URANS simulations with and without radiation model (DO) and LES and experimental results of [106] at different axial locations ( $x = 20$ mm (a), $x = 30$ mm (b), $x = 40$ mm (c)) . . . . .	59
5.23	Comparison of axial velocity distribution, $u$ , into the longitudinal plane of the burner between pure methane (left) and methane-hydrogen mixture (right) combustion case. . . . .	60
5.24	Comparison of mean static temperature field of combustion case into the longitudinal plane of the burner between pure methane (100%v $CH_4$ ) without (a) and with (b) DO and methane-hydrogen mixture (70%v $CH_4 + 30\%v H_2$ ) without (c) and with (d) DO. . . . .	61
5.25	Comparison of $OH$ mean mass fraction field of combustion case into the longitudinal plane of the burner between pure methane (100%v $CH_4$ ) without (a) and with (b) DO and methane-hydrogen mixture (70%v $CH_4 + 30\%v H_2$ ) without (c) and with (d) DO. . . . .	62
5.26	Comparison of $CO_2$ mean mass fraction field of combustion case into the longitudinal plane of the burner between pure methane (100%v $CH_4$ ) without (a) and with (b) DO and methane-hydrogen mixture (70%v $CH_4 + 30\%v H_2$ ) without (c) and with (d) DO. . . . .	63
5.27	Representation of the numerical domain of the Vanderbilt University lab-scale burner . . . . .	65
5.28	Boundary condition reacting flow Vanderbilt University burner: (a) inlet section, (b) combustion chamber surface, (c) outlet section. . . . .	66
5.29	View of the Mesh #3 with the zones partition for the grid refinement . . . . .	66
5.30	Mesh refinement: comparison between the exp. Nandula et al. [111] and the numerical results in terms of axial velocity profiles at different axial positions ((a) $y/D = 0.1$ , (b) $y/D = 0.3$ , (c) $y/D = 0.6$ , (d) $y/D = 1$ ) - reacting case . . . . .	67
5.31	Study on turbulent closure: comparison between the exp. Nandula et al. [111] and the numerical results in terms of axial velocity profiles for different turbulence models ( $k-\varepsilon$ , $k-\omega$ SST, RSM) at different axial positions ((a) $y/D = 0.1$ , (b) $y/D = 0.3$ , (c) $y/D = 0.6$ , (d) $y/D = 1$ ) - reacting case . . . . .	68

5.32	Study on turbulent closure: comparison between the exp. Nandula et al. [111] and the numerical results in terms of temperature profiles for different turbulence models ( $k-\varepsilon$ , $k-\omega$ SST, RSM) at different axial positions ((a) $y/D = 0.1$ , (b) $y/D = 0.3$ , (c) $y/D = 0.6$ , (d) $y/D = 1$ ) - reacting case	69
5.33	Comparison of progress variable $\theta$ for burner fueled by methane-air mixture respect with the RANS simulation developed by Andrein et al. in [113]	70
5.34	Contours of Heat Release Rate for the two different mixtures: methane-air and hydrogen-air	71
5.35	Contours of progress variable $\theta$ for the two different mixtures: methane-air and hydrogen-air	71
5.36	Comparison between axial velocity profiles for two different mixtures (red line 100% $CH_4$ , blue line 100% $H_2$ ) for reacting flow, at different axial positions ((a) $y/D = 0.1$ , (b) $y/D = 0.3$ , (c) $y/D = 0.6$ , (d) $y/D = 1$ )	72
5.37	Comparison between axial velocity contours for two different mixtures. Transversal lines represent the cross sections where the axial velocity profiles have been compared in Fig. 5.36	72
5.38	Comparison between temperature contours for two different mixtures. Transversal lines represent the cross sections where the temperature profiles have been compared in Fig. 5.36	73
5.39	Comparison between temperature profiles for two different mixtures (red line 100% $CH_4$ , blue line 100% $H_2$ ), at different axial positions ( $y/D = 0.1$ , $y/D = 0.3$ , $y/D = 0.6$ , $y/D = 1$ )	73
5.40	Comparison between density profiles for two different mixtures (red line 100% $CH_4$ , blue line 100% $H_2$ ), at different axial positions ((a) $y/D = 0.1$ , (b) $y/D = 0.3$ , (c) $y/D = 0.6$ , (d) $y/D = 1$ )	74
6.1	Numerical domain and relative boundary conditions used in COMSOL Multiphysics <sup>®</sup> (dimension in mm). The area in light blue represents the domain of Vanderbilt University burner object of the aforementioned CFD simulation (see section 5.2)	75
6.2	Comparison between eigenmodes obtained by using different mesh refinements in COMSOL	76
6.3	Comparison between Rayleigh Index obtained by using different mesh refinements in COMSOL	77
6.4	Sensitivity analysis on interaction index $n$ for benchmark $CH_4$ -air mixture	78
6.5	Sensitivity analysis on interaction index $n$ for $H_2$ -air mixture	79
6.6	Comparison between the CFD solutions and the same fields interpolated on the COMSOL mesh. Vanderbilt University burner fueled by $CH_4$ -air mixture	79
6.7	Schematic view of vortical structures downstream the bluff body for two different mixtures.	80
6.8	Schematic of flame for two different mixtures. The solid line denotes the flame front and $H$ represents the length of the flame for the two mixtures.	81
6.9	Heat release rate trends against time for Vanderbilt University burner: (a) $CH_4$ -air mixture, (b) $H_2$ -air mixture	81
6.10	Comparison of the Time delay vs. heat release rate for Vanderbilt University burner fueled by methane-air and hydrogen-air mixtures	82

6.11	Comparison of the real part of Rayleigh index of Vanderbilt University burner fueled by (a) methane-air and (b) hydrogen-air mixtures. . . . .	83
6.12	Comparison of the Time Delay $\tau$ of Vanderbilt University burner fueled by methane-air and hydrogen-air mixtures. . . . .	84
6.13	Comparison of frequencies and growth-rates for the two cases fueled with $CH_4$ -air and $H_2$ -air . . . . .	84
6.14	Comparison of the acoustic pressure of the first four modes when the two mixtures ( $CH_4$ -air and $H_2$ -air) are employed . . . . .	85
7.1	Cycle and component of the Turbec T100 mGt system are: (1) centrifugal compressor, (2) recuperator, (3) low- $NO_x$ burner, (4) radial turbine, (5) high speed generator, (6) economizer. (inspired by [124]) . . . . .	88
7.2	Burner AE-T100: (a) Longitudinal view. The air enters in counter-current in the gap between the outer casing and inner walls. The pilot and main fuel enter through injector on the external surface of the inner walls (inspired by [125]), (b) isometric cut the view (reprinted from [126]). . . . .	88
7.3	Fuel injection system main and pilot through plane highlighting the counter-flow air inlet, the pilot (1) and main (2,2') swirlers, and the dilution holes. . . . .	89
7.4	2D geometry of AE-T100 burner. The red line highlights the section $0.19D$ downstream the pilot injector on which the mesh sensitivity analysis has been carried out. . . . .	91
7.5	Burner AE-T100: 3D hexahedral mesh of AE-T100 burner. The mesh is made up of 4.3M cells, with refinement in the injectors, counter-flow air channel, first part of the primary flame zone, pilot and zone around the dilution holes, (b) mesh sensitivity analysis on temperature and velocity field in the flame zone, in the plane of the pilot combustion chamber $0.19D$ downstream the pilot injectors section (see the arrow in Fig. 7.5a and the red line in Fig. 7.4) (inspired by [126]). . . . .	91
7.6	Comparison between three mixtures on longitudinal plane in terms of: (a) axial velocity contours, (b) temperature contours. . . . .	92
7.7	Comparison between three mixtures in terms of equivalence ratio contours: (a) in the longitudinal plane, (b) in the plane of the combustion chamber $0.30D$ downstream of the pilot injectors section. . . . .	93
7.8	First four natural frequencies of AE-T100 burner. . . . .	94
7.9	Settings of AE-T100 burner in OSCILOS Simulator:(a) Geometry (b) thermal proprieties. . . . .	95
7.10	Settings of AE-T100 burner in OSCILOS Simulator:(a) $n - \tau$ parameters (b) inlet boundary (c) outlet boundary. . . . .	96
7.11	First four frequencies of AE-T100 burner calculated by OSCILOS code. . . . .	97
7.12	Geometry and boundary conditions for the AE-T100 burner validation scenario in COMSOL Multiphysics <sup>®</sup> . . . . .	98
7.13	Comparison between first four modes of AE-T100 burner fueled by methane-air mixture calculated by: (a)(c)(e)(g) OSCILOS code, (b)(d)(f)(h) COMSOL Multiphysics <sup>®</sup> solver. . . . .	99
7.14	Geometry and boundary conditions of the AE-T100 burner in thermoacoustic simulation in COMSOL Multiphysics <sup>®</sup> . . . . .	100
7.15	Frequency and Growth Rate for the AE-T100 burner fueled by three different mixtures. . . . .	102





# List of Tables

3.1	Geometric parameters of the numerical Model . . . . .	27
3.2	Boundary conditions and settings for cylindrical combustor in module Acoustic Pressure and Frequency Domain of COMSOL Multiphysics® . .	30
3.3	Grid influence on Frequencies and Growth Rate . . . . .	33
3.4	Frequency and Growth Rate of the third stable mode by varying the Mach Number in the plenum. . . . .	34
5.1	Louisiana burner parameters of the non reacting flow. . . . .	46
5.2	Louisiana burner reacting flow parameters for pure methane and methane enriched with hydrogen case. . . . .	48
5.3	Louisiana burner mesh parameters. . . . .	49
5.4	Calculation parameters of reacting flow simulations. . . . .	55
5.5	$CO_2$ emissions computed for both pure methane and methane-hydrogen mixture cases . . . . .	60
5.6	Comparison of the main parameters characterizing the two mixtures em- ployed in this work: $CH_4$ -air and $H_2$ -air . . . . .	65
5.7	Summary of the grid refinement strategy applied for Vanderbilt University burner. For each zone, the cell dimension is reported ( $D$ is the bluff body diameter) . . . . .	67
6.1	Mesh refinement for FEM simulations in COMSOL of Vanderbilt Univer- sity test-rig . . . . .	76
6.2	Sensitivity analysis on interaction index $n$ for Vanderbilt University burner fueled by $CH_4$ -air and $H_2$ -air mixtures . . . . .	78
6.3	Eigenmodes comparison between Vanderbilt University burner fueled by $H_2$ -air and $CH_4$ -air mixture . . . . .	83
7.1	Air supply in burner AE-T100 . . . . .	89
7.2	Boundary and inlet conditions of the simulated cases - inlet fuel: $T_{fuel} =$ 288 K, inlet air: $\dot{m}_{air} = 690$ g/s, $T_{air} = 865$ K . . . . .	89
7.3	Natural frequencies calculated by matlab code. . . . .	94
7.4	Comparison between natural modes calculated by Matlab code and modes calculated by OSCILOS code. . . . .	97
7.5	Parameters of COMSOL Multiphysics® simulations of AE-T100 burner by using the flame sheet model. . . . .	98
7.6	Comparison between modes calculated by two code. . . . .	98

7.7	Parameters of COMSOL Multiphysics <sup>®</sup> simulations of AE-T100 burner by using the field of fluid-dynamic quantities as parameters in main combustion chamber. . . . .	100
7.8	Fields of fluid-dynamic properties of the AE-T100 main combustion chamber interpolated on COMSOL Multiphysics <sup>®</sup> . . . . .	101
7.9	First five modes of AE-T100 fueled by three mixtures. . . . .	103

# List of Symbols

## Acronyms

CFD	Computational Fluid Dynamics	
LES	Large Eddy Simulation	
RANS	Reynolds-Averaged Navier-Stokes	
URANS	Unsteady Reynolds Averaged Navier-Stokes	
FEM	Finite Element method	
GR	Growth Rate	$1/s$
LHS	Left-Hand side	
LHS	Right-Hand side	
LHV	Lower Heating Value	$MJ/kg$
FRF	Flame response function	
FTF	Flame transfer function	
PDF	Probably Density Function	
PFR	Product Formation Rate	
HRR	Heat Release Rate	
PVC	Precessing Vortex Core	
CTRZ	Central Toroidal Recirculation Zone	
CRZ	Corner Recirculation Zone	
WRZ	Wake Recirculation Zone	
PSD	Power Spectral Density	
DO	Discrete Ordinates	
TIT	Turbine inlet temperature	
CHP	Combined Heat and Power	

## Roman symbols

$A$	area	$m^2$
$b$	axial location of flame sheet	$m$
$C_p$	specific heat at constant pressure	$J/(molK)$
$C_v$	specific heat at constant volume	$J/(molK)$
$c$	speed of sound	$m/s$
$D$	diameter	$m$
$E_d$	wave energy dissipation	$J/s$
$f$	frequency	$Hz$
$M$	Mach number	
$MW$	molecular weight	$g/mol$
$n$	acoustic-combustion interaction index	
$P$	thermal power	$W$
$p$	pressure	$Pa$

$\dot{q}$	specific heat release rate	$W/m^2$
$\dot{Q}$	global heat release rate	$W/m^2$
$T$	temperature	$K$
$Ra$	Rayleigh index	
$x$	x coordinate	
$y$	y coordinate	
$u$	velocity	
$V$	control volume	$m^3$
$z$	z coordinate	
$\mathbf{x}$	x spatial coordinate	
$\mathbf{n}$	unit vector	
$D_\psi$	diffusion coefficient of intensive physical quantity $\psi$	
$S_\psi$	source term that take into account generation of $\psi$ in $V$	
$Z$	elemental mass fraction	
$Y$	mass fraction of generic species $k$ in mixture	
$Sc$	Schmidt number	
$\mathbf{g}$	gravity vector	$m/s^2$
$\mathbf{F}$	external body force	$N$
$\bar{\bar{I}}$	unit tensor	
$E$	total internal energy for unit of mass	$J/kg$
$e$	internal energy for unit of mass	$J/kg$
$h$	static enthalpy	$J$
$J$	diffusive flux	$kg/m^2$
$D$	diffusive coefficient	
$X$	molar fraction	
$S_m$	source term due to transfer of mass into gas phase from fluid droplets or reacting particles	
$S_{user}$	user-defined source term	
$k_t$	turbulent kinetic energy	$J$
$S_{h,rad}$	heat losses due to the radiation	$W/m^3$
$S_{chem}$	heat losses due to the chemical reaction	$W/m^3$
$S_g$	swirl number	
$H$	flame length	$m$
$s$	thickness of heat release zone	$m$
$H_{comb}$	lower heating value of fuel	$MJ/kg$
$R_g$	gas constant	$J/(kgK)$
$k$	laminar thermal conductivity	$W/(mK)$
$S$	entropy	$J/K$
$l$	length	$m$
$\Re$	real part	
$\Im$	imaginary part	
<b>Greek symbols</b>		
$\alpha$	air-fuel ratio	
$\beta$	factor provides a measure of the intensity of heat release	
$\gamma$	ratio between specific heat	
$\lambda$	$-i\omega$	$rad/s$
$\rho$	density	$kg/m^3$
$\varphi$	phase	$rad$

---

$\phi$	equivalence ratio	
$\omega$	angular frequency	$rad/s$
$\tau$	time delay	$s$
$\partial$	partial derivative	
$\theta$	progress variable	
$\psi$	intensive physical quantity	
$\Psi$	extensional physical quantity	
$\bar{\tau}$	stress tensor	
$\xi$	mixture fraction	
$\chi$	scalar dissipation	
$\sigma$	viscous stress tensor	
$\mu$	dynamic viscosity	$Pa\ s$
$\delta$	Dirac delta	
$\zeta$	swirl angle	$deg$
$\eta$	damping	$s^{-1}$
<b>Sub- and Super-scripts</b>		
$-$	mean	
$\wedge$	acoustic quantity	
$'$	fluctuation	
<i>air</i>	air	
<i>ax</i>	axial component	
<i>burner</i>	burner	
<i>fuel</i>	fuel	
1	upstream flame sheet	
2	downstream flame sheet	
<i>m</i>	harmonic order	
<i>h</i>	hydraulic	
<i>j</i>	reference position	
<i>in</i>	inner diameter	
<i>out</i>	outer diameter	
<i>sw</i>	swirler	
<i>mix</i>	fuel mix	
<i>st</i>	stoichiometric	
<i>ra</i>	restriction area	
<i>k</i>	generic species in mixture	
<i>t</i>	turbulent	
<i>l</i>	laminar	
<i>i</i>	i-th species	
<i>tan</i>	tangential	
<i>rad</i>	radial	
<i>ad</i>	adiabatic	
<i>pilot</i>	pilot	
<i>th</i>	thermal	
<i>int</i>	internal	
<i>ext</i>	external	
<i>P</i>	plenum	
<i>CC</i>	combustion chamber	
<i>B</i>	burner	



# Introduction

## Background

The use of hydrogen methane mixtures in energy production by gas turbines is going to play a key role in the transition towards a carbon-free economy. The higher LHV of hydrogen and wider flammability limits than the conventional hydrocarbons lead to make hydrogen very interesting as fuel in gas turbine. On the other hand, the flame speed increases and the autoignition times decrease by using the hydrogen in fuel mix. These aspects lead to several problems in combustion process because they could be cause the flashback phenomena and autoignition in the burners. Furthermore, the use of hydrogen increases the thermoacoustic instabilities in the burner. The studies that first led to a physical model able to justify the origin of combustion instabilities were carried out by Crocco and Cheng [1] who published in 1956 a technical report on combustion instabilities in liquid propellant rocket engines. Crocco and Cheng formulated a mechanism based on time elapsed between the fuel injection and the sudden conversion into hot gases that they called “time lag”. They recognized analogies to the dynamic behavior of closed loop systems with time delay. The system is unstable if, under certain conditions, any small perturbation applied to the system in smooth operation, such as to pressure distribution or fuel flow, tends to amplify; otherwise, if the initial state is re-established after the external perturbation, the system is stable. At the onset of the instability the pressure fluctuations are small and can be treated like acoustic waves. Therefore, the onset of the instability can be considered as the interaction of heat release oscillations that occur in proximity of the flame and acoustic waves; this is the reason why they are often referred to as thermo-acoustic combustion instabilities. The mechanism proposed by Crocco and Cheng for rocket engines is still the basis of the mechanisms that are mostly adopted to model combustion instabilities in modern lean burn premixed combustion systems fueled by natural gas or in lean premixed pre-vaporized liquid fueled systems where combustion instabilities are still an issue. Starting from this model, a comparison between instability that occurs in laboratory burner fueled by methane and hydrogen mixtures will be carried out.

## Overview of modeling approaches

The study of thermo-acoustic combustion instability is a very complex issue and, over the years, several different approaches have been developed to model this phenomenon. In the last decades many research groups have devoted significant efforts in studying experimentally and numerically this phenomenon [1–4]. The main methodologies are based on: Low-order numerical models [5–7], CFD (Computational Fluid Dynamics) models [8–12] and Helmholtz solver models [3, 4, 13–15]. The low-order models divide the thermoacous-



tic system into a network of elementary acoustic domains (e.g., pipes, burner, flame, etc.), where the acoustic field is represented as the solution of the Helmholtz's equation. The CFD models (e.g., solving URANS, LES approaches) allow the analysis of the thermo-fluid dynamic flow fields inside the combustor, in a more realistic configuration, requiring high computational costs. By using Helmholtz solver, differential equation problems in the time domain can be transformed into eigenvalue problems in the frequency domain by using the Fourier transform. The Finite Element Method (FEM) thermoacoustic simulation is more accurate than the low order simulation due to the possibility of simulating 3D geometry based on the fluid-dynamic properties obtained by CFD simulation. The CFD simulation is able to predict only dominant mode that characterizes the combustion chamber. On the contrary, by using the Helmholtz solver a list of stable or unstable modes can be obtained. FEM approaches require information on the heat release, time delays, flow fields, pressure, and temperature distributions, in order to correctly model instabilities during the combustion process. For this reason, appropriate CFD simulations can be useful not only to investigate the combustion process but also to determine the suitable information, which is required by the FEM models.

## Present contribution

While there is an increasing number of experimental and numerical investigations on the gas turbine burner fueled by pure hydrogen and blend methane hydrogen. The investigations on the thermoacoustic behavior of these mixtures are very few. Experimental investigations on burners are being carried out but these tests are usually conducted with limited instrumentation whose results are insufficient to perform a complete validation of the numerical analysis. Furthermore, these results are usually proprietary and not discussed in scientific papers. On the numerical level, a linear analysis of the flame acoustic perturbation and a detailed modeling of the acoustic damping of the system is required in order to predict correctly the thermoacoustic behavior of burner designed for methane-air mixture in case that hydrogen is used as fuel. The numerical analysis by using Helmholtz solver has been carried out in order to predict the thermoacoustic behavior of a burner fueled by hydrogen-air mixture. CFD and thermoacoustic comparison between burner fueled by methane-air and hydrogen-air mixture have been carried out. In this framework, the lab-scale bluff body stabilized premixed burner of the Vanderbilt University and swirled premixed Louisiana laboratory burner have been investigated by means of a fully 3D RANS approach. The choice of these two burners is due to the presence of many numerical and experimental studies on it when fueled by methane-air mixture. In the case of  $\text{CH}_4$ -air mixture, the numerical setup has been validated with experimental results. Moreover, the influence of the turbulence models has been investigated. A study of the burner fueled with  $\text{H}_2$ -air mixture has been carried out in order to compare the flame shape with those of the case fueled by  $\text{CH}_4$ -air mixture. Finally, a study of acoustic modes (frequencies and the growth rates) by using FEM approach (COMSOL Multiphysics<sup>®</sup>) is carried out in the case of two fuel mixtures in order to understand the influence of hydrogen on thermoacoustic behavior. At last, the thermoacoustic comparison between several mixtures has been carried out also on the burner of micro gas turbine AE-T100.

## Outline

The thesis is organized as follows. In Chapter 1 the role of hydrogen as carbon green fuel in gas turbine combustor is presented. The dissertation analyzes the role of hydrogen methane blends in burner of gas turbine with particular focus on the structure and flame position, thermo-acoustic stability of the system, and the effect of flashback. In Chapter 2 a description of the phenomenon of thermo-acoustic instability is presented. Chapter 3 describes the thermo-acoustic mathematical model that can be used in order to analyze this phenomenon. Chapter 4 describes the mathematical models used in this thesis in order to develop a Computational Fluid Dynamic (CFD) study of the burners analyzed. In Chapter 5 the CFD analysis of two laboratory burners fueled by methane enriched with hydrogen is presented. The first model is the Louisiana laboratory burner on which the comparison between 100% CH<sub>4</sub> and 70% CH<sub>4</sub>-30% H<sub>2</sub> mixtures is studied. The second model is the Vanderbilt laboratory burner on which the comparison between 100% CH<sub>4</sub> and 100% H<sub>2</sub> mixtures is presented. In Chapter 6 the thermo-acoustic instabilities are studied by coupling a Helmholtz solver with a numerical Flame Response Function (FRF) in order to analyze the behavior of Vanderbilt burner fueled by 100% CH<sub>4</sub> and 100% H<sub>2</sub> mixtures. Finally, chapter 7 compares the thermo-acoustic behavior of micro gas turbine AE-T100 fueled by 100% CH<sub>4</sub>, 10% H<sub>2</sub> - 90% CH<sub>4</sub> and 30% H<sub>2</sub> 70% - CH<sub>4</sub> mixtures.



# Chapter 1

## Hydrogen as a green fuel in gas turbines

### 1.1 Hydrogen in carbon-free economy

To reduce global warming in recent years, considerable decarbonization of power generation has been required [16–20]. In this framework, hydrogen became the main actor in carbon-free economy [21–26]. This role is due, in particular, to a no  $CO_2$  production when it is burned [27, 28]. The main problem is that it is produced, in bigger fraction, using fossil fuel with respect than that produced by electrolysis. Indeed, the latter is the way that could lead to substitute the fossil fuels in order to make the combustion systems more sustainable. The production of  $H_2$  offers a most promising solution in order to store peaks of renewable electricity production [29]. In particular, it represents a solution in order to eliminate the intermittent outputs of wind and solar energy. Due to the higher cost of energy production the use of renewable energy is increased. As a consequence, the attention of industry on low-carbon hydrogen production is increased. This kind of storage of excess renewable energy through the production of hydrogen is called power-to-gas [30]. This stored hydrogen can be used as fuel in burners of gas turbine in order to product energy.

### 1.2 Hydrogen - methane blend in gas turbine

The use of hydrogen or a blend of methane-hydrogen in burner of turbo gas designed for methane fuel offers several advantages compared to conventional fuel hydrocarbons. Combustion of pure hydrogen would eliminate the emissions of carbon dioxide ( $CO_2$ ), and carbon monoxide ( $CO$ ). Furthermore, the minimum energy to ensure the mixture ignition is lower with respect the typical one of the hydrocarbons. Instead, the high adiabatic flame temperature, 2380 K, in the case of use pure hydrogen in gas turbine, leads to problems with the materials of component and, in general, makes necessary dilution before entering the fluid into the turbine. The adiabatic flame temperature for pure hydrogen is over 150 K higher than for methane at conventional Lean Premixed (LPM) burner stoichiometry. If the operating conditions are not adjusted, for example by switching to a leaner equivalency ratio, this will lead to greater  $NO_x$  emissions for a fixed gas turbine configuration. The speed of flame propagation in a mixture of hydrogen and air is very high with respect the hydrocarbon-based fuels. This is primarily due to

the higher reaction speed of the  $H_2 - O_2$  mixtures. This could create serious control problems and flashback phenomenon (propagation of the front of flame in the opposite direction to that of origin of the premixed reagents). As result, it could be originated the risk of explosions or in any case serious damage to the “reactor”. The short ignition delay of hydrogen-air mixture allows for more compact burners, characterized by shorter residence times and therefore by lower thermal  $NO_x$  production. Finally, hydrogen has a high LHV per unit mass in the combustion process compared to hydrocarbon-based fuels. This means large storage capacities are required for hydrogen gas.

### 1.2.1 Influence of Hydrogen on structure and flame position

In [31] chemiluminescence images show a similar flame shape position of the “centre of heat release” for natural gas and 25% hydrogen 85% methane mixtures, Fig. 1.1. The “centre of heat release” is a complex function of flame length, flame shape, flow velocity, and frequency [32].

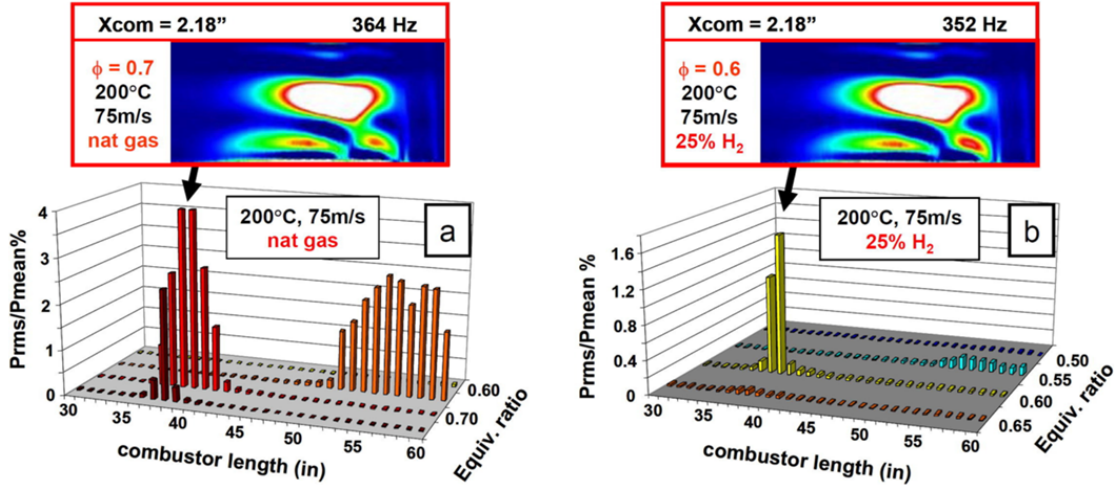


Figure 1.1:  $CH^*$  chemiluminescence flame images and stability map for (a) natural gas and (b) 25%  $H_2 - CH_4$  mixtures cases. Inlet temperature is 200 °C and inlet bulk velocity is 75 m/s for each case (reprinted from [31]).

From these studies it is clear that the flames in stable condition with the same “centre of heat release” present similar dynamic responses and flame structure. The change in flame shape at the same equivalence ratio ( $\phi$ ), is highlighted by Shanbhugue et al. [33]. Fig. 1.2 shows that with the increase of hydrogen content there is a flame shape transition for lower equivalence ratio. Furthermore, from Fig. 1.2 it is possible to notice that for  $\phi = 0.58$  the 100%  $CH_4$  mixture exhibits V-shape flame, while in the case fueled by 10% and 20% hydrogen by volume blend a M-shape (flame shape in which the combustion takes place between outer and inner recirculation zone) is observed. Also, [34–37] observed that the addition of hydrogen to natural gas leads to transition from V-shape to M-shape flame. This transition is due to the higher diffusivity of hydrogen that causes higher extinction strain rates. Lantz et al. in [35] investigated industrial gas turbine burners employed by Siemens Energy (SGT-700 and SGT-800) fueled by natural gas enriched with up to 80% hydrogen by volume at atmospheric pressure. The flame shape and size variations were shown as a consequence of the


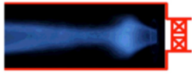





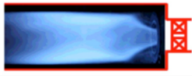







$\phi$	100% CH <sub>4</sub>	90% CH <sub>4</sub> / 10% H <sub>2</sub>	80% CH <sub>4</sub> / 20% H <sub>2</sub>
0.48			
0.51			
0.53			
0.56			
0.58			
0.62			
0.63			

Figure 1.2: Comparison flame shape transition between pure methane 10% and 20% hydrogen by volume blend in function of equivalence ratio (reprinted from [33]).

increase of the hydrogen concentration. When the concentration on 80% of hydrogen is fixed, the flame is anchored on the burner tip in the outer recirculation zone. In the [36], the pure hydrogen flame was found to be more compact and closer to the burner exit than the pure methane flame. Experimental simulations on premixed combustion in a test rig of a gas turbine burner fueled by methane hydrogen mixture have been carried out by Giuberti et al. in [38] in order to evaluate the influence of hydrogen on stabilizing a M-flame. Schefer et al. in [34] drew attention to the variation in flame structure and increase in the peak of OH concentration due to the addition of hydrogen in methane-air mixture in premixed swirl-stabilized flame.

### 1.2.2 Effect on Thermo-acoustic stability of the system

A review on the influence of hydrogen and hydrogen-enriched natural gas on the thermoacoustic instability has been carried out by Beita et al. in [39]. The effect of hydrogen injection on the stabilization and flame structure of a swirling flame has been investigated by Laera et al. in [2]. Janus et al. in [40] investigated a sub-scale combustor fueled by natural gas, propane, and some hydrogen/hydrocarbon mixtures. Numerical and experimental results highlighted that the shifting of instability regime is due primarily to the change in reaction rate. Æsøy et al. in [41] scaled the Flame Transfer Function (FTF) on a no swirled bluff body stabilized burner fueled by different hydrogen and methane blends. In [42] the thermoacoustic instabilities for fully premixed combustor fueled by methane-hydrogen blend up to 40% hydrogen by volume have been studied. A transition in frequency spectrum from multi-modal distribution to a single has been observed with the increase of hydrogen concentration. Hydrogen enrichment extends the lean blowout limit and leads to a shift in the dynamic instability regions toward

lower equivalence ratios. Shanbhogue et al. in [33] prove that the critical equivalence ratio, that indicates the transition between stability and instability of a swirl stabilized combustor burning in atmospheric pressure and temperature, decreases in the case of using methane-hydrogen mixtures. The influence of equivalence ratio on azimuthal instabilities of annular laboratory-scale burner fueled by methane hydrogen mixtures has been carried out in [43]. This parameter is intrinsically linked to the higher turbulent flame speed of hydrogen and to the resulting upstream shift in flame position which alters the thermoacoustic characteristics of the combustor. The implication is that a combustor that is thermoacoustically stable could be rendered unstable and vice versa depending upon the equivalence ratio. Increasing hydrogen content can also lead to transitions from stable to unstable combustion through an intermittent regime characterised by random bursts of high amplitude limit cycle oscillations and stable aperiodic states. Mode switching between natural frequencies of the combustor, including the excitation of higher frequency instabilities, can also be triggered as a result of hydrogen enrichment. The forced flame response of natural-gas enriched with hydrogen up to 60% by volume has been reported by Kim et al. in [37]. The higher burning velocity of hydrogen was the cause of flame structure transition towards lower equivalence ratio.

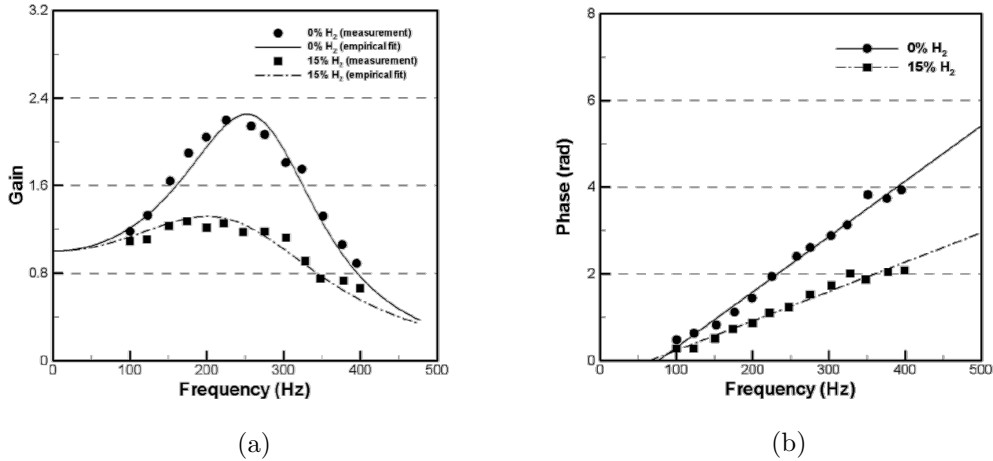


Figure 1.3: Sensibility on hydrogen enrichment of gain (a) and phase (b) of FTF at low forcing amplitude. Operating conditions: bulk velocity = 60 m/s, inlet temperature = 200°C and equivalence ratio = 0.6 (reprinted from [37]).

In Fig. 1.3 the gain and phase of the FTF of pure methane and blend of 85% of methane and 15% of hydrogen are reported in order to illustrate the effect of hydrogen addition. Kim et al. in [37] found a decrease in gain and phase of FTF at low forcing amplitude for hydrogen blend with respect methane flame. The shorter and compact M-flame allows damping of flow perturbation in the combustor. The impact of variation in flame surface area on heat release and thus impact on thermoacoustic instability [44, 45] was investigated by Zhang et al. in [46]. Methane-hydrogen fuel blend up to 40% by volume and for a range of equivalence ratio and Reynolds number were studied. In the case of unstable flames, hydrogen addition leads to a stronger coupling between heat release oscillation and unsteady pressure fluctuations. The increase of hydrogen in the fuel mixture leads to an increase in the local flame surface area. As summarized, the above studies have demonstrated that the higher reactivity of hydrogen-enriched fuels in the

gas turbine burners has a significant influence on flame position and flame structure and hence can alter the thermoacoustic behavior and stability driving mechanism of the system.

### 1.2.3 Effect on Flashback

There is a strong correlation between thermoacoustic instabilities and the phenomenon of flashback in the burner. In [47] a fully premixed burner at atmospheric pressure conditions fueled by methane-hydrogen blends with up to 50%  $H_2$  by volume has been experimentally investigated. The hydrogen addition causes an increase in root mean square pressure amplitude and leads to a shift in the dominant frequency to a lower frequency. This behavior coincides with the condition in which flashback was started. The pressure and heat release oscillation are in phase with flashback signal. Also, in [48], the flashback phenomenon induced by thermoacoustic instability due to the hydrogen addition to natural gas was highlighted. Fig. 1.4 shows spectra of the pressure, heat release, and flashback. In the case of pure methane, flashback is not present, while in the case of 50% $H_2$  by volume of hydrogen, in correspondence of 40 Hz, there is a signal of flashback.

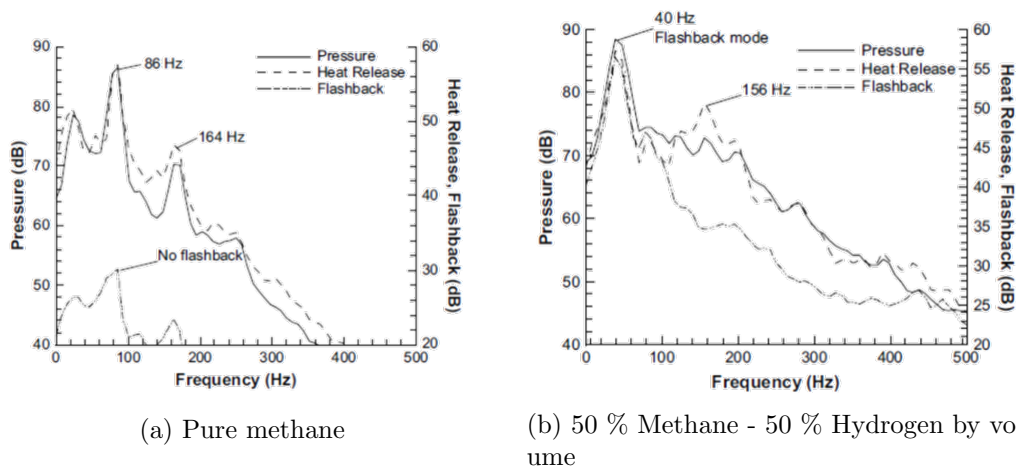


Figure 1.4: Spectra of heat release, pressure and flashback at  $\phi = 0.7$ . Flashback was induced by combustion instabilities (reprinted from [47]).





## Chapter 2

# Description of thermo-acoustic instability

Thermo-acoustic combustion instabilities are generated by mutual interaction between pressure fluctuations and heat release rate oscillations of the flame. These instabilities are spontaneously excited and self-sustained by various feedback loop mechanisms, the most important of which is summarized in Fig. 2.1. Fluctuations of heat release in the combustion zone generate acoustic waves. Due to propagation and reflection, these acoustic waves will move in the combustion chamber up to the burner region where the velocity fluctuations in the proximity of the injection point will produce flow and mixture perturbations, which may close the feedback loop.

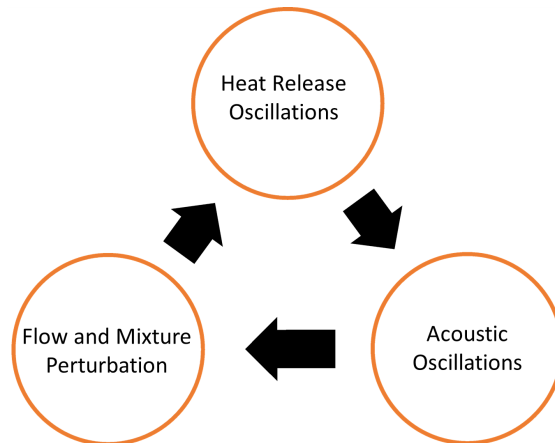


Figure 2.1: The principal feedback process responsible of thermo-acoustic combustion instabilities (reprinted from [49]).

### 2.1 Rayleigh Criterion

Lord Rayleigh, in 1878, highlighted the importance of the phase between unsteady heat release and pressure oscillations in the onset of instability [50]. The Rayleigh criterion is best defined as the following inequality:

$$\int_0^\tau \int_0^V p'(x,t) \dot{q}'(x,t) dv dt \geq \int_0^\tau \int_0^V E_d(x,t) dv dt \quad (2.1)$$

where  $p'$  and  $\dot{q}'$  are the pressure and heat release fluctuations respectively,  $\tau$  is the period of oscillation,  $V$  is the control volume and  $E_d$  is the wave energy dissipation. The LHS of the inequality represents the total mechanical energy added to the oscillations by the heat addition process per cycle. The RHS of the inequality represents the total energy dissipated by the oscillation per cycle. When the inequality in Eq. (2.1) is satisfied, thermoacoustic instability occurs. It is possible to neglect the acoustic dissipating term inside the combustor so that Eq. (2.1) becomes:

$$\int_0^\tau \int_0^V p'(x,t) \dot{q}'(x,t) dv dt \geq 0 \quad (2.2)$$

As consequence, a specific relationship between  $p'$  and  $\dot{q}'$  yields the Rayleigh criterion to be satisfied. Assuming that  $p'$  and  $\dot{q}'$  have a periodic time dependence, the sign of the time integral in the LHS depends on the ratio  $\tau/\tau_0$ , where  $\tau_0$  is the phase difference between  $p'$  and  $\dot{q}'$ . In particular when:

- $\frac{\tau}{\tau_0} = 0, 1, 2, \dots$  the integral has a positive maximum
- $\frac{\tau}{\tau_0} = \frac{1}{2}, \frac{3}{2}, \dots$  the integral has a negative minimum

This agrees with Lord Rayleigh's hypotheses: when  $p'$  and  $\dot{q}'$  are in phase, instability occurs, when  $p'$  and  $\dot{q}'$  are out of phase, stabilization occurs. Since the integral in Eq. (2.2) is both temporal and spatial, stabilization and destabilization can occur in different locations inside the combustor. In general, thermoacoustic oscillations are associated with one of the natural pure acoustic modes of the combustion chamber of the system. These include, for example, bulk, axial, and transverse modes [51]. Under specific conditions, however, it has been found that instabilities may arise due to the excitation of coupled convective–acoustic modes. These modes occur at frequencies lower than those of purely acoustic modes and are due to hot–gas spots (known as entropy waves) that are generated in the flame region and convected toward the end of the combustion chamber. If the wavelength of entropy waves and the wavelength of the acoustic waves are comparable, the acoustic waves that propagate back to the flame may be excited. This will excite another convected wave, and a second feedback loop mechanism is established. These types of modes are often encountered in systems that present a nozzle or a flow section reduction at the end of the combustion chamber and operate at conditions close to flame blow–off [49].

### 2.1.1 Thermodynamic Rayleigh Criterion

The Rayleigh criterion can be better explained by means of a thermodynamic cycle [52]. Sound waves are isentropic so in the  $p - v$  diagram of Fig. 2.2 the volume moves back and forth on an isentrope (blue line). When the heat is added or extracted periodically to the gas, an increase of the specific volume  $v$  of the gas occurs. If this heat addition is in phase with pressure oscillations, the state of the gas volume moves clockwise around a thermodynamic cycle (curve 1-2'-3'-4' in Fig. 2.2). This process can be seen as a “thermoacoustic heat engine”, transferring mechanical energy into sound waves, and a

self-excited instability can occur, as suggested by Rayleigh. In the case in which heat release fluctuations are not perfectly in phase with pressure fluctuations, the area 1-2'-3'-4' will be smaller and the efficiency reduced. When the heat release fluctuations are out-of-phase with pressure fluctuations, the system moves counterclock-wise through the cycle 1-2''-3''-4'', and mechanical energy is extracted from the acoustic wave.

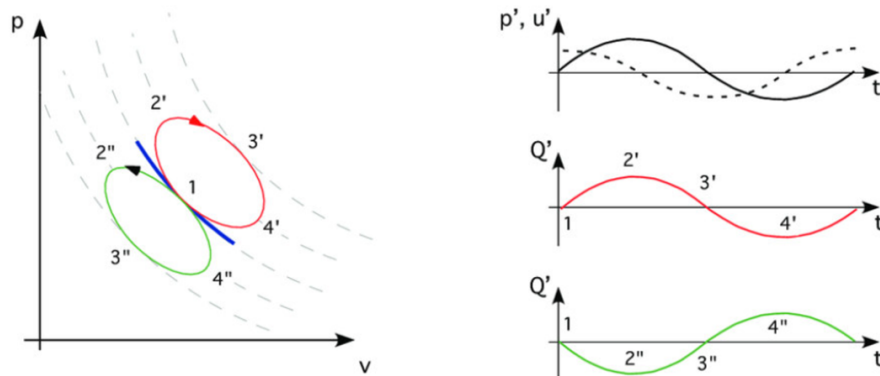


Figure 2.2: Thermodynamic interpretation of the Rayleigh criterion.

The mechanical work performed by the thermodynamic cycle resulting from acoustic oscillations with heat release can be expressed as follows:

$$\oint p dv = \oint (\bar{p} + p') d(\bar{v} + v') = \oint \bar{p} dv' + \oint p' dv' = 0 + \oint p' dv' \quad (2.3)$$

In Eq. (2.4) the specific volume  $v'$  is split into an isotropic part, for which  $v' = -\frac{v dp'}{\gamma p}$ , and part  $v'^{(\dot{q})}$  due to heat addition (or removal).

$$\oint p' dv' = -\frac{v}{\gamma p} \oint p' dp' + \oint p' dv'^{(\dot{q})} = 0 + \oint p' \frac{dv'^{(\dot{q})}}{dt} dt \sim \oint p' \dot{q}' dt \quad (2.4)$$

The rate of change of  $v'$  in time is proportional to heat release perturbations. So the work done by the “thermoacoustic engine” is positive (energy added to acoustics) if the integral of  $p' \dot{q}'$  is positive over one period of oscillation, as already suggested by Rayleigh. If the losses of acoustic energy exceed the rate of energy input to the acoustic field by the fluctuating flame, a self-excited instability cannot develop, even if  $p'$  and  $\dot{q}'$  are in phase. This is why the Rayleigh criterion is a necessary, but not a sufficient criterion for instability to occur [52].

## 2.2 Driving mechanisms

In a simple longitudinal gas turbine combustor equipped with a laboratory scale burner open at both ends, there are a lot of mechanisms capable of driving combustion instabilities, see Fig. 2.3. The indicated mechanisms can be grouped in two categories, indirect and direct:

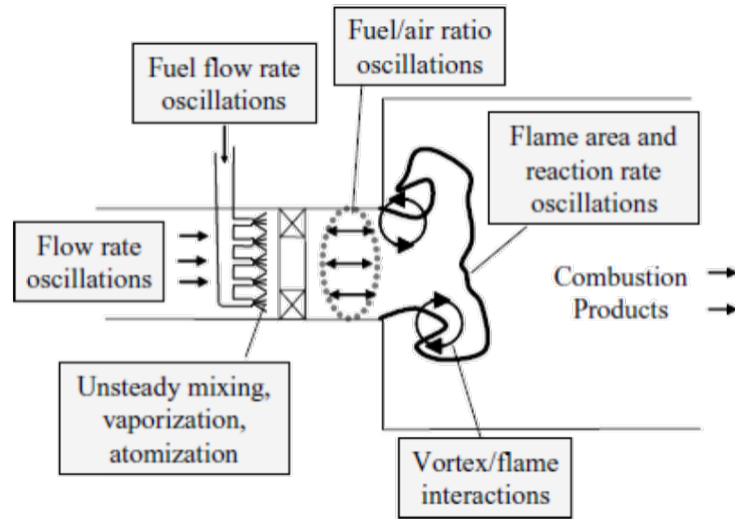


Figure 2.3: Driving mechanism of thermoacoustic instability in gas turbine burner (reprinted from [49]).

1. Indirect heat release oscillation generation mechanism:

**Equivalence ratio oscillations.** [1, 53] In the section of premixer, fuel and air flow rate ( $\dot{m}'_f$  and  $\dot{m}'_{air}$  respectively) are modulated by pressure oscillations. This produces oscillations of the equivalence ratio and, thus, heat release rate fluctuations.

**Fuel flow rate fluctuations.** [54] If fuel nozzle is unchoked, the pressure drop across the nozzle is modulated by the pressure oscillations in the combustor. This produces fluctuations of fuel injection and hence generates oscillatory heat release rate in flame zone.

**Liquid fuel - Unsteady vaporization and atomization process.** [1, 53] If the liquid fuel is used, interactions between the fuel spray and acoustic waves during the primary and secondary breakthrough mechanisms produce periodic variations of the spray shape, droplet sizes and evaporation rates. These variations produce heat release rate oscillations in the flame zone.

2. Direct heat release oscillation generation mechanism:

**Flame area variations.** [55] Direct interactions between the flame front and the acoustic waves in the flame zone produce periodic variation of the flame area and, thus, heat release fluctuations.

**Flame vortex interactions.** [56–58] Velocity fluctuations ( $u'$ ) in the combustion zone may trigger the already existing “shear layer” disturbances caused by flow separation at the exit of the burner producing large-scale coherent vortical structures. In the initial stage of their formation, these vortices generally consist of combustible mixture. Later, as they are convected toward the flame front, these vortices entrain hot combustion products and get ignited. This is followed by rapid combustion and sudden breakdown of the vortex structure

with the consequent energy transfer at lower-scale turbulence structures. If these vortical structures reach the flame front, they may distort the flame and cause its surface area to oscillate, producing heat release fluctuations .

Fig. 2.4 shows the response of five of previously described mechanisms to a pressure pulse with period  $T$ . The heat release fluctuations due to the process 1 and pressure fluctuations are positively correlated since the time delay  $\tau_1$  is of the order of the period of the acoustic waves,  $T$ . Hence, this specific mode is excited and, if the energy addition exceeds damping, instability occurs (as stated in the Rayleigh criterion).

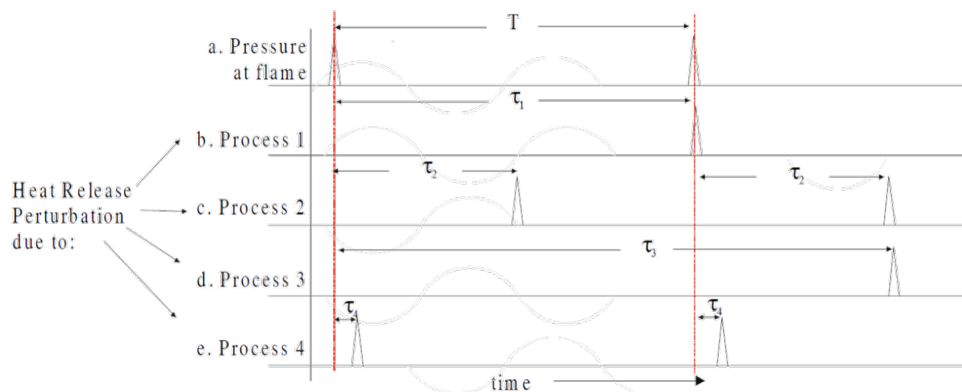


Figure 2.4: Influence of delayed responses of various combustor processes to a periodic pressure disturbance (reprinted from [49]).

If the period of pressure fluctuation is  $T_2 = T/2$  (second mode of the system), then  $\tau_1 = 2T_2$  and  $\tau_2 = T_2$ . Energy is added to this mode by process 1 and process 2. Therefore, different mechanisms play different roles in the stability of the different modes. Each mode of the system can be excited, the only condition is that the characteristic time scale of the excitation mechanisms has to equal the period  $T$ ,  $2T$  or any other integer multiple of  $T$  of the resonant mode. The “pulselike” response shown in Fig. 2.4 does not happen in real systems in which the pressure oscillations generally vary harmonically with time. So, the time delays and the period of the various modes do not need to be exactly equal in order to satisfy the Rayleigh criterion. It has been found that if  $T - T/4 < n\tau < T + T/4$ , where  $n$  is an integer, a positive correlation between pressure fluctuations and heat release fluctuations is still observed [54].

## 2.3 Instability damping mechanism

The acoustic energy generated is partially naturally dissipated from the burner. This allows for an attenuation of the phenomenon of instability and allows the resonant system to reach a non-stationary equilibrium. The amplitude of these oscillations directly depends on the power developed by the burner. All damping mechanisms can be grouped in three categories:

**Viscous and heat-transfer mechanism.** These damping effects are due to boundary layer and flow-separation. Suppose that an acoustic wave impinges obliquely on a rigid wall. In the proximity of the surface, flow, and temperature boundary layers

induce the transfer of the energy of the mode into vortical velocity fluctuations and entropy fluctuations, respectively. As a consequence, the energy of the wave reflected by the wall is smaller than the one of the incident wave [59, 60]. The magnitude of these dissipation mechanisms increases with frequency as  $(f \cdot \tau_v)^{(1/2)}$ , where  $f$  is the frequency and  $\tau_v$  is the viscous or thermal transport timescale. Flow separation losses can occur in zones of strong velocity gradients, e.g., rapid expansion of the jet into the combustor. Here, the acoustic energy is transferred between the acoustic mode and vorticity mode through the mean flow.

**Convection and/or radiation of acoustic energy.** Radiation and/or convection of acoustic energy out of the boundaries of the system is, in most cases, the highest source of acoustic damping. In general, this damping mechanism scales with frequencies as  $(f \cdot \frac{D}{c})^2$ , where  $f$ ,  $D$ ,  $c$  are frequency, characteristic dimension of the system and speed of sound, respectively. Usually, the magnitude of acoustic damping in a system is quite small, so the presence of low-velocity mean flow can have a significant impact on the system's damping level [61]

**Transfer of energy from natural to high order modes.** This mechanism consists of transferring energy from the excited modes (natural frequency  $f_0$ ) to higher harmonics ( $2f_0, 2f_0, \dots$ ) or sub-harmonics ( $f_0/2, f_0/3, \dots$ ). The energy at these higher frequencies is more rapidly dissipated by the previously described damping mechanisms whose magnitudes are a function of frequency [62].

## 2.4 Linear and nonlinear stability

Under the hypothesis of small acoustic fluctuations with respect to the mean values of the flow, acoustics became linear and second order terms in the dynamical equations can be neglected [63]. The energy addition and dissipation become only function of the frequency. In this case, a linear stability analysis can be performed. Unfortunately, in nature, all systems present a saturation process, which is governed by nonlinear terms. When the amplitude of oscillations increases, the dynamics of the system is controlled by the nonlinear process. The energy addition becomes also a function of the amplitude of the oscillations, which reaches its maximum value when the time average of energy addition equals the dissipation.

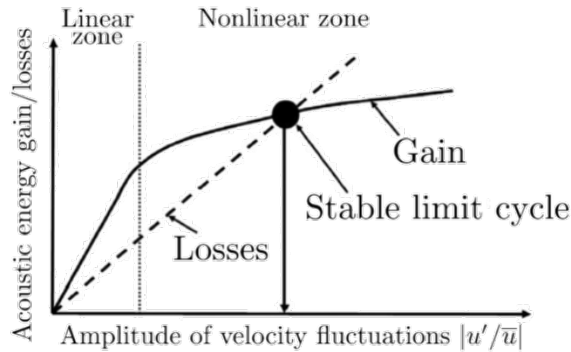


Figure 2.5: Energy gain and acoustic losses in a thermoacoustic system forced with a sinusoidal signal of frequency  $\omega$  and increasing amplitude  $|u'/u|$  (reprinted from [64]).

In Fig. 2.5 is shown a typical trend of the energy gain and acoustic losses as function of the excitation level  $|u'/u|$  [64]. For small values of the excitation level the flame responds linearly (linear zone in Fig. 2.5). With the increase of the amplitude of the acoustic oscillations, a saturation of the energy gain is observed (nonlinear zone in Fig. 2.5). As indicated by Eq. (2.1), the amplitude of the instability grows until the rate of energy addition equals the rate of energy dissipation. When this condition is reached, the system exhibits a stable limit cycle (intersection point of the two lines, indicated with the circular dot in Fig. 2.5). Limit cycles are inherently nonlinear phenomena in which the system manifests self-sustained oscillations of amplitude constant with time. In a phase diagram, a limit cycle is an isolated closed trajectory from which, in absence of perturbation, the system cannot deviate [65].





## Chapter 3

# Thermo-acoustic mathematical models of combustion instability

In this chapter, the mathematical models that are used for the analysis of thermo-acoustic combustion instabilities are reviewed. Firstly, starting from the Navier–Stokes equations of the fluid flow, the equations of the flow under heat release rate fluctuations are obtained. Then, under the hypotheses of vanishing flow velocity, the classical undamped inhomogeneous wave equation with a source term representing the heat release rate fluctuations is presented. In order to close the problem, the concept of flame response function (FRF) is introduced. At last, in Section 3.5 the influence of mean flow is presented with particular attention on its implementation in low order and Helmholtz solvers. Part of this chapter has been already published in [15].

### 3.1 Time domain equations

The acoustic analysis is based on the resolution of the wave equation. It is derived from the linearized equations of the perturbations. In the case of a compressible viscous fluid in the absence of external forces, the Navier-Stokes equations are obtained from the conservation of mass and momentum, i.e.:

$$\frac{D\rho}{Dt} + \rho \nabla \cdot \mathbf{u} = 0 \quad (3.1)$$

$$\rho \frac{D\mathbf{u}}{Dt} = -\nabla p + \frac{\partial \sigma_{i,j}}{\partial x_j} \mathbf{e}_i \quad (3.2)$$

where  $p$  is the pressure,  $\rho$  the density,  $\mathbf{u}$  is the velocity vector,  $\sigma_{i,j}$  is the viscous stress tensor and  $\mathbf{e}_i$  is the unit vector in the direction  $i$ .  $D/Dt$  is the material derivative and it is defined as  $\partial/\partial t + \mathbf{u} \cdot \nabla$ . If the fluid is considered as a perfect gas, the gas law is introduced:

$$\frac{p}{\rho} = R_g T \quad (3.3)$$

where  $T$  is the temperature and  $R_g = c_p - c_v$  is the gas constant with  $c_p$  and  $c_v$  the specific heats at constant pressure and constant volume, respectively. The internal energy  $e$  is equal to  $c_v T$ , whereas the enthalpy  $h$  is equal to  $e + p/\rho$ . Conservation of energy reads:

$$\rho \frac{D}{Dt} \left( e + \frac{1}{2} \mathbf{u}^2 \right) = -\nabla \cdot (p\mathbf{u}) + \dot{q} + \nabla \cdot (K\nabla T) + \frac{\partial}{\partial x_j} (\sigma_{i,j} u_i) \quad (3.4)$$

where  $K$  is the thermal conductivity and  $\dot{q}$  is the heat release rate added to the fluid per unit volume. Using the conservation of momentum, Eq. (3.2), Eq. (3.4) can be rearranged as:

$$\rho \frac{Dh}{Dt} = \frac{Dp}{Dt} + \dot{q} + \nabla \cdot (K\nabla T) + \sigma_{i,j} \frac{\partial u_i}{\partial x_j} \quad (3.5)$$

Entropy  $S$  is defined by the thermodynamic relation  $dh = TdS + (1/\rho)dp$ , so that Eq. (3.5) yields:

$$\rho T \frac{DS}{Dt} = \dot{q} + \nabla \cdot (K\nabla T) + \sigma_{i,j} \frac{\partial u_i}{\partial x_j} \quad (3.6)$$

where it is clear that entropy is increased by heat input, heat transfer and viscous effects. The viscous effects lead to the combination of turbulent reacting flow with pressure fluctuations. These effects can be treated making use of CFD simulations based on LES (Large Eddy Simulation) techniques. However, it is possible to assume that the viscous effects are normally small within the volume, so the flow can be assumed to be inviscid and consider  $\sigma_{i,j} = 0$ . Additionally, the fluid is assumed to be an ideal gas with specific heats constant. From its definition entropy can be evaluated as  $S = c_v \log(p/\rho^\gamma)$ , where  $\gamma = c_p/c_v$  is the ratio of specific heats. The flow can be considered the sum of a steady mean flow (identified by an over-bar), which depends only on space, and a small perturbation (identified by a prime). The instantaneous pressure field can then be written as:

$$p(\mathbf{x}, t) = \bar{p}(\mathbf{x}) + p'(\mathbf{x}, t) \quad (3.7)$$

and the same for the other variables. Substituting the above expression in Eq. (3.1), Eq. (3.2) and Eq. (3.6), and retaining only the first order terms (linear functions of the perturbations), we obtain the following set of linear equations for the fluctuating quantities  $\rho'$ ,  $\mathbf{u}'$  and  $p'$ :

$$\frac{\partial \rho'}{\partial t} + \mathbf{u}' \cdot \nabla \bar{\rho} + \bar{\rho} \nabla \cdot \mathbf{u}' + \bar{\mathbf{u}} \cdot \nabla \rho' + \rho' \nabla \cdot \bar{\mathbf{u}} = 0 \quad (3.8)$$

$$\bar{\rho} \frac{\partial \mathbf{u}'}{\partial t} + \nabla p' + \bar{\rho} \mathbf{u}' \cdot \nabla \bar{\mathbf{u}} + \bar{\rho} \bar{\mathbf{u}} \cdot \nabla \mathbf{u}' + \rho' \bar{\mathbf{u}} \cdot \nabla \bar{\mathbf{u}} = 0 \quad (3.9)$$

$$\frac{\partial S'}{\partial t} + \mathbf{u}' \cdot \nabla \bar{S} + \bar{\mathbf{u}} \cdot \nabla S' = \frac{R_g \dot{q}'}{\bar{p}} - \frac{R_g \bar{q}}{\bar{p}^2} p' \quad (3.10)$$

The above system of equations represents the linearized Euler equations (LEE) in a reacting flow. Its complete solution, at the time being, is a challenging task that has found only few applications [66]. In a uniform flow, that is a simplified hypothesis that can be applicable to one-dimensional combustion chambers, the linearized equations result:

$$\frac{D\rho'}{Dt} + \bar{\rho} \nabla \cdot \mathbf{u}' = 0 \quad (3.11)$$

$$\frac{D\mathbf{u}'}{Dt} + \frac{1}{\bar{\rho}}\nabla p' = 0 \quad (3.12)$$

$$\bar{\rho}\bar{T}\frac{DS'}{Dt} = \dot{q}' \quad (3.13)$$

Combining Eq. (3.11), Eq. (3.12) and Eq. (3.13), and considering that  $S' = c_p p'/p - c_p \rho'/\rho = 0$ , the inhomogeneous wave equation is obtained:

$$\frac{1}{\bar{c}^2} \frac{D^2 p'}{Dt^2} - \nabla^2 p' = \frac{\gamma - 1}{\bar{c}^2} \frac{D \dot{q}'}{Dt} \quad (3.14)$$

where  $c$  is the speed of sound. Eq. (3.14) may be applied to a combustion gas, provided that reactants and products behave as perfect gases and there is no molecular weight change during the chemical reaction [67]. Since in gas turbine combustion chamber the flow velocity is generally far below the sound velocity, the flow velocity  $u$  can be generally considered negligible. Under such hypothesis, the inhomogeneous wave equation in Eq. (3.14) becomes:

$$\frac{1}{\bar{c}^2} \frac{\partial^2 p'}{\partial t^2} - \nabla^2 p' = \frac{\gamma - 1}{\bar{c}^2} \frac{\partial \dot{q}'}{\partial t} \quad (3.15)$$

### 3.2 Frequency domain equations

The thermo-acoustic analysis can be carried out in the frequency domain [49,61,63]. Considering linear analysis, a generic fluctuating quantity can be defined as  $a' = \Re(\hat{a} \exp(i\omega t))$ , where  $\hat{a}$  is a complex quantity,  $i$  the imaginary unit, and  $\omega$  is a complex angular frequency. Applying the harmonic analysis for the two acoustic variables  $p'$  and  $u'$ , result:

$$p'(\mathbf{x}, t) = \hat{p}(\mathbf{x}) \exp(i\omega t) \quad (3.16)$$

$$u'(\mathbf{x}, t) = \hat{u}(\mathbf{x}) \exp(i\omega t) \quad (3.17)$$

where  $\mathbf{x}$  is the spatial coordinate. For finite disturbances, the flame model  $\dot{q}'(\mathbf{x}, t)$  may not be pure harmonic but is still periodic and hence it can be described by a Fourier series:

$$\dot{q}'(\mathbf{x}, t) = \left( \sum_{m=0}^{\infty} \hat{q}(\mathbf{x})^m e^{im\omega t} \right) \quad (3.18)$$

where  $m$  is the order of the harmonics. In thermo-acoustic analysis, neglecting non linear effects, we will consider that the modes act one independently from the other. Therefore, considering a single frequency, it follows:

$$\hat{q}'(\mathbf{x}, t) = \hat{q}(\mathbf{x}) e^{i\omega t} \quad (3.19)$$

Introducing Eq. (3.16) and (3.19) in Eq. (3.15) and considering a spatial variation of the base flow thermodynamic variables, the inhomogeneous Helmholtz Eq. (3.20) can be derived:

$$\frac{\lambda^2}{c^2} \hat{p}(\mathbf{x}) - \hat{\rho}(\mathbf{x}) \nabla \cdot \left( \frac{1}{\hat{\rho}(\mathbf{x})} \nabla \hat{p}(\mathbf{x}) \right) = -\frac{\gamma-1}{c^2(\mathbf{x})} \lambda \hat{q}(\mathbf{x}) \quad (3.20)$$

where  $\lambda = -i\omega$ .

### 3.3 Flame Response Function (FRF)

A relation that correlates the unsteady heat release rate fluctuation with the pressure waves is needed in order to close the thermoacoustic problem. In the frequency domain, in the case of small perturbations, the local flame response to an acoustic perturbation can be represented by the Flame Response Function (FRF), that is a complex function that depends only on the excitation frequency or on the angular frequency  $\omega = 2\pi f$ . This function is defined as the ratio of the heat release fluctuations to the relative velocity fluctuations at the reference position  $j$ :

$$\frac{\hat{q}}{\bar{q}} = FRF(\omega, \mathbf{x}) \frac{\hat{u}_j}{\bar{u}_j} \quad (3.21)$$

More complex model, not examined here, take into account the amplitude of  $\hat{u}_j$  of the acoustic velocity through a FDF (Flame Describing Function). In Eq. (3.21), the subscript  $j$  corresponds to the reference position. The FRF can be expressed in terms of its gain,  $G = |FRF(\mathbf{x})|$ , and phase,  $\varphi = \arg(FRF(\mathbf{x}))$ . FRF is used to have a spatial distribution of the flame response along the flame front in order to have a more accurate response of the system than that obtained from the flame-sheet model (unsteady heat release is assumed to be concentrated at a single axial plane). The evaluation of FRF is the most important aspect of thermoacoustic analysis because it describes the coupling between the acoustic field and the heat fluctuations. The FRF (Eq. (3.21)) depends on the flame characteristics, as described by Lieuwen [49] and Camporeale et al. [3]. The present thesis is focused on thermoacoustic instabilities occurring in gas turbine combustors equipped by a perfectly premixed burner [68]. For these kinds of combustors, the flame is fed by a premixed fuel-air stream, whose mixture is formed before entering in the burner. Considering the zero-Mach-number-approximation, heat release rate fluctuations are mainly influenced by velocity fluctuations. Following these assumptions, in the frequency domain, applying the harmonic analysis, the linear FRF is derived:

$$FRF = n \exp(-i\omega\tau) \quad (3.22)$$

In the general formulation, both  $n$  and  $\tau$  are function of the frequency  $\omega$ . The interaction index  $n$  is usually modeled as a first-order low pass filter whose cut-off frequency  $\omega_c$  is defined as the angular frequency at which the gain begins to decrease [69, 70].

$$\frac{\hat{q}}{\bar{q}} = n \exp(-i\omega\tau(\mathbf{x})) \frac{\hat{u}_j}{\bar{u}_j} \quad (3.23)$$

#### 3.3.1 Eigenvalue analysis

The Helmholtz equation (Eq. (3.20)) coupled with the flame model of Eq. (3.21) represents a quadratic eigenvalue problem that can be solved for the studies of instability making use of the techniques of linear analysis [65]. In the eigenvalue problem,

$\omega$  is a complex angular frequency, whose real part gives the frequency of the oscillations,  $f = \Re(\omega)/2\pi$  Hz, whereas the imaginary part corresponds to the growth rate  $GR = -\Im(\omega)/2\pi$  s<sup>-1</sup> that allows, in absence of damping, the identification of unstable modes. If  $GR$  is positive, the acoustic mode is unstable so the amplitude of fluctuations grows with time. If  $GR$  is negative, the acoustic mode is stable, i.e., perturbations decay with time. However, as described in Section 2.3, real systems are characterized by a certain amount of damping  $\eta$  s<sup>-1</sup>. If this damping is not included directly into the calculations, the stability is governed by the difference  $GR - \eta$ , predicting instability when the growth rate is greater than the damping rate. One also deduces that when  $GR = \eta$  a limit cycle condition is reached.

### 3.4 Mathematical models and Solutions procedures

Different approaches to analyze thermo-acoustic instabilities in gas turbine combustion chambers can be found in several works (see [44,52]). Fig. 3.1 shows, among the several classifications of the tools to solve the thermo-acoustic problem, the classification proposed by Balachandran [71]. In this case, there is an increase in the complexity of the tool going from the right to the left.

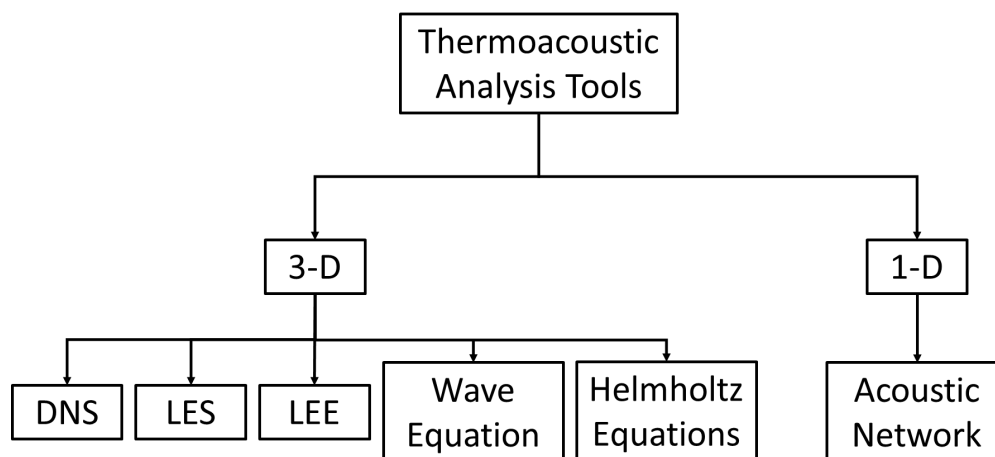


Figure 3.1: Classification of tools to solve the thermo-acoustic problem (inspired by [71]).

A Direct Numerical Simulation (DNS) is a simulation in computational fluid dynamics in which the Navier-Stokes equations are numerically solved without any turbulence model, resolving the whole range of spatial and temporal scales of turbulence. Large Eddy Simulation (LES) operates on the Navier-Stokes equations to reduce the range of length scales of the solution, reducing the computational cost by means of mathematical models for turbulence. The Linearized Euler Equations (LEE) are obtained by linearization of the Euler equations in non-conservation form with flux Jacobians. The Wave Equation is an important second-order linear partial differential equation for the description of waves. The Helmholtz Equation is an elliptic partial differential equation derived from the wave equation. An Acoustic Network is a 1-D numerical approach to solve the acoustic problem. All these methodologies can be also classified into three different groups: Low-Order Models, models that use the computational fluid dynamic (CFD) approach, and models that use the finite element method (FEM). Tools like the Acoustic

Networks and the Helmholtz solvers detect the eigenfrequencies, the growth or the decay of the modes, the limit cycle amplitude of the oscillations, but in order to use these tools information regarding the flame model needs to be provided by the user. Theoretically, LES may capture the thermo-acoustic oscillations in the combustor, but it requires huge computational sources and time. A brief excursus of these tools is now presented below.

### 3.4.1 Low-order model approach

Low-order models are based on the idea of modeling thermo-acoustic system as a network of acoustic elements (hence the name Acoustic Network), where each element corresponds to a component of the system, such as a duct, a nozzle, a burner, etc... Generally, it is a one-dimensional tool mainly based on linear acoustics and harmonic time dependence ( $i\omega t$ ). A good introduction to these methods comes from Munjal et al. [51] and from Poinso et al. [61]. Initial studies were carried out by Merk et al. [72]. Afterwards other studies were carried out on afterburners by Bloxsidge et al. [73] on the Rijke tube, by Heckl [74] on the lean premixed land-based gas turbines, by Keller et al. [75] and by Lieuwen et al. [76] on aero engines, by Giuliani [77], on rocket motors and on industrial boilers. Applications to annular combustion chambers are proposed by Dowling and Stow [78] and by Campa et al. [79]. Bohn et al. [80] were the first to suggest to use the Low-Order models as a network tool. Then this methodology had a very large spread in several universities and research centers. At University of Cambridge considering early studies [67, 69, 73, 81], Dowling and Stow developed a one-dimensional code, called LOTAN, to use linear theory to predict the combustion oscillations in LPP combustors [63]. Once the combustor is defined as a series of subsystems, mathematical transfer function matrices are used to connect these lumped acoustic elements one to each other, so providing the continuity of acoustic velocity and pressure across each zone. The unknowns are acoustic pressure and velocity fluctuations ( $p'$  and  $u'$  respectively) at the ports of each network element. Instead of using  $p'$  and  $u'$ , the Riemann invariants can be used as unknowns. The coupling relations for the unknowns across an element are combined into the transfer or scattering matrix of the element. The transfer matrix coefficients of all network elements are combined into the system matrix  $\mathbf{S}$  of the network. In this scheme, the flame is concentrated in one of the lumped elements, located at the beginning of the combustion chamber and described by the Rankine-Hugoniot relationship. The numerical tools build up a representation of the system as an assembly of interconnected elements, construct the corresponding system matrix from this network and then solve the algebraic problem. Generally acoustic networks represent a very robust methodology, providing fast answers for studies carried in the frequency domain [63] and in time domain [70]. Instabilities coupled with longitudinal [7, 82] and azimuthal modes [83, 84] can be analyzed assuming linear [81] and nonlinear flame models [69, 70, 85, 86]. These models are very attractive because they provide non-trivial results and they are very helpful to understand the instability mechanisms. Due to the possibility to insert the influence of the mean flow, acoustic networks are a good approach to study the influence of all the mechanisms related to the mean flow, such as entropy waves [13] and vorticity [87]. However, they are limited in geometrical flexibility and, when complex elements are involved, these models become inexact and make use of assumptions and empirical data.

### 3.4.2 Finite Elements method approach

In order to overcome some of the limitations of the previous techniques, a finite element method approach may be used [3, 13]. Three-dimensional geometries can be examined. This approach numerically solves the differential equation problem in the frequency domain described by Eq. (3.20). It is possible to examine a spatially distributed flame inside the combustion chamber and not only a simplified flame sheet [88]. This method takes into account the main phenomenon, that is the interaction between the flame and the pressure waves, but the fluid dynamic phenomena are neglected. It is possible to evaluate the damping capability of the pressure waves by means of passive systems. In this thesis, the stability analysis is carried out with the finite element code COMSOL Multiphysics. Numerically, the discretization of Eq. (3.20) along with the boundary conditions over an unstructured finite element grid results in the following eigenvalue problem [3, 89, 90]:

$$2A\mathbf{P} + \omega B(\omega)\mathbf{P} + \omega^2 C\mathbf{P} = D(\omega)\mathbf{P} \quad (3.24)$$

where  $\mathbf{P}$  is the eigenmodes values vector, the matrices  $A$  and  $C$  contain coefficients originating from the discretization of the Helmholtz equation,  $B(\omega)$  is the matrix of the boundary conditions, and  $D(\omega)$  represents the source term due to the unsteady heat release rate. When the heat release is considered, the eigenvalue problem becomes non-linear and is solved with an iterative algorithm. At the  $k^{th}$  iteration equation Eq. (3.24) is first reduced to a linear eigenvalue problem:

$$[2A + \Omega_k B(\Omega_k) - D(\Omega_k)]\mathbf{P} + \omega_k^2 C\mathbf{P} \quad (3.25)$$

where  $\Omega_k = \omega_{k-1}$  is the previous iteration result. The software uses the ARPACK numerical routine for large-scale eigenvalue problems. This is based on a variant of the Arnoldi algorithm, called the implicit restarted Arnoldi method [91]. This procedure is iterated until the error defined by  $\epsilon = |\omega_k - \Omega_k|$  is lower than a specific value, typically  $10^{-6}$ .

### 3.4.3 Computational Fluid Dynamic approach

CFD models developed for the analysis of the thermoacoustic instability generally use LES (large eddy simulation) techniques. These LES codes [92, 93] are proposed in order to investigate the phenomenon of combustion instability and matching pressure oscillations with turbulent combustion phenomena and the dynamically relevant scales are considered during the resolution. Through Computational Fluid Dynamic (CFD) analysis the physics of instability phenomenon can be replicated by taking into account several parameters such as the interaction between the flame and pressure waves. On the other hand, an enormous computational effort is required for the resolution. The governing equations are obtained by applying a spatially localized time independent filter of given size to the set of compressible Navier-Stokes equations. Because of the filtering approach, LES allows a dynamic representation of the large scale motions, whose contributions are critical if the geometry is complex. The simulation becomes more complex when reacting flows are considered because the chemical phenomena occur at small scales, which is the modelled range. However the macro mixing process is naturally taken into account when the largest scales are explicitly computed. Giauque et al. [93] presented maps of combustion delay and response amplitude extracted from LES, showing the potentiality



of LES simulations in obtaining more accurate results. Martin et al. [94] and Nicoud et al. [13] analyzed an active flame in 3D combustion chamber by means of LES approach, considering local fields of  $k$  and  $\tau$  and forcing the frequencies of interest. LES uses the exact chamber geometry, a high-order numerical scheme, and a fully compressible solver to track acoustic waves. It is able to capture the self-excited combustion instability appearing in the real engine and provides unique insight into the behavior of the unstable combustor. After the initialization, the computations of reacting flow evolve (in case of unstable systems) to the most amplified oscillation mode. In that case LES captures (if present) the process of the onset and the transient growth of the oscillations until the limit cycle is reached, without any external excitation. The LES is able to reveal the dominant mode that characterizes the combustion chamber. However, this is one limit of the methodology since any other unstable mode is hidden while the Helmholtz solvers offer a list of the potential unstable modes that may occur. If the simulation is carried out over several cycles, it is possible to resolve interesting phenomena such as spinning or standing modes [95].

### 3.5 Influence of mean flow

Usually the mean flow is small compared to that of the sound that is generated in the combustion chamber for gas turbines (in general the Mach number does not exceed 0.2 [63]), but at the same time, it is not fully correct to neglect it. Mean flow has two main consequences. First of all, it affects the propagation speed of acoustic waves, with the traveling downstream wave at a speed  $c+u$  and upstream at a speed  $c-u$ . Furthermore, it affects the existence of entropy and vorticity waves. Moreover, the contribution of the mean flow is of fundamental importance to describe the behavior of compact elements such as a burner. The introduction of the velocity in a computational model, able to solve the convective wave equation, allows to evaluate with greater accuracy the effect of the fluid dynamics and acoustic losses on the propagation of the waves within a compact element. Dowling and Stow in [63] used a low-order model to demonstrate the damping of frequencies as the number of Mach increases. Besides this, Dowling and Stow, demonstrated that the introduction of mean flow on simple geometries is not significant for Mach number less than about 0.2, without mentioning its influence on real test rig applications. The mean flow would introduce the possibility of a new mode of oscillation at much lower frequency in which the time taken for the convection of entropic waves or hot spots sets the period of fluctuation [96]. Campa in [97] introduced the mean flow in a methodology based on FEM in order to analyze the instability of thermo-acoustic combustion of gas turbines by solving a convective Helmholtz equation on simple longitudinal geometries with constant cross section. Starting from Eq. (3.14) the inhomogeneous wave equation can be rewritten in vectorial form as follow:

$$\frac{\partial^2 p'}{\partial t^2} - c^2 \nabla^2 p' + (\mathbf{u} \cdot \nabla)^2 p' = (\gamma - 1) \left( \frac{\partial \dot{q}'}{\partial t} + \mathbf{u} \cdot \nabla \dot{q}' \right) \quad (3.26)$$

Making explicit the component in Eq. (3.26), as follow:

$$\begin{aligned}
& \frac{\partial^2 p'}{\partial t^2} - c^2 \nabla^2 p' + 2u_x \frac{\partial^2 p'}{\partial x \partial t} + 2u_y \frac{\partial^2 p'}{\partial y \partial t} + 2u_z \frac{\partial^2 p'}{\partial z \partial t} + u_x^2 \frac{\partial^2 p'}{\partial x^2} + u_y^2 \frac{\partial^2 p'}{\partial y^2} + u_z^2 \frac{\partial^2 p'}{\partial z^2} + \\
& + u_x u_y \frac{\partial^2 p'}{\partial x \partial y} + u_x u_z \frac{\partial^2 p'}{\partial x \partial z} + u_y u_z \frac{\partial^2 p'}{\partial y \partial z} + u_x \frac{\partial u_y}{\partial x} \frac{\partial p'}{\partial y} + u_x \frac{\partial u_z}{\partial x} \frac{\partial p'}{\partial z} + u_y \frac{\partial u_x}{\partial y} \frac{\partial p'}{\partial x} + \\
& + u_y \frac{\partial u_z}{\partial y} \frac{\partial p'}{\partial z} + u_z \frac{\partial u_x}{\partial z} \frac{\partial p'}{\partial x} + u_z \frac{\partial u_y}{\partial z} \frac{\partial p'}{\partial y} = (\gamma - 1) \left( \frac{\partial \hat{q}'}{\partial t} + u_x \frac{\partial \hat{q}'}{\partial x} + u_y \frac{\partial \hat{q}'}{\partial y} + u_z \frac{\partial \hat{q}'}{\partial z} \right)
\end{aligned} \tag{3.27}$$

In the frequency domain we can rewrite Eq. (3.27) as follow:

$$\begin{aligned}
\frac{\lambda}{c^2} - \nabla^2 \hat{p} = & -\frac{\gamma - 1}{c^2} \left( \lambda \hat{q} + u_x \frac{\partial \hat{q}}{\partial x} + u_y \frac{\partial \hat{q}}{\partial y} + u_z \frac{\partial \hat{q}}{\partial z} \right) - \frac{1}{c^2} \left( -2\lambda u_x \frac{\partial \hat{p}}{\partial x} - 2\lambda u_y \frac{\partial \hat{p}}{\partial y} + \right. \\
& - 2\lambda u_z \frac{\partial \hat{p}}{\partial z} + u_x^2 \frac{\partial^2 \hat{p}}{\partial x^2} + u_y^2 \frac{\partial^2 \hat{p}}{\partial y^2} + u_z^2 \frac{\partial^2 \hat{p}}{\partial z^2} + u_x u_y \frac{\partial^2 \hat{p}}{\partial x \partial y} + u_x u_z \frac{\partial^2 \hat{p}}{\partial x \partial z} + u_y u_z \frac{\partial^2 \hat{p}}{\partial y \partial z} + \\
& \left. + u_x \frac{\partial u_y}{\partial x} \frac{\partial \hat{p}}{\partial y} + u_x \frac{\partial u_z}{\partial x} \frac{\partial \hat{p}}{\partial z} + u_y \frac{\partial u_x}{\partial y} \frac{\partial \hat{p}}{\partial x} + u_y \frac{\partial u_z}{\partial y} \frac{\partial \hat{p}}{\partial z} + u_z \frac{\partial u_x}{\partial z} \frac{\partial \hat{p}}{\partial x} + u_z \frac{\partial u_y}{\partial z} \frac{\partial \hat{p}}{\partial y} \right)
\end{aligned} \tag{3.28}$$

### 3.5.1 Mean flow in Low Order solver

OSCILOS is a low-order simulator developed at the Imperial College London by Prof Aimee Morgans and Dr. Dong Yang. It is written in Matlab<sup>®</sup>/Simulink<sup>®</sup>. OSCILOS permits to draw a combustor as a network of connected modules and to model the acoustic waves whether in 1-D or 2-D plane. OSCILOS is a user-friendly low-order code and it returns reliable results by considering simple geometries. The mean flow is calculated by assuming 1-D flow condition with changes only across flames or module interface. It is necessary to connect the thermal properties and the mean flow between the neighboring combustor sections. In OSCILOS, between neighboring combustor sections, the mass and the energy flux are unchanged while the momentum flux is increased by the axial force on the walls [63, 98]. Therefore, the first-order energy equation can be written in function of ratio of sectional surface areas [98]. As bench-mark test the cylindrical duct with a uniform cross-sectional area, examined by Dowling and Stow [63], has been investigated. The details of this geometry, that reproduces an atmospheric rig, are given in Table 3.1 and the geometry is schematically reproduced in Fig. 3.2. The simulations have been carried out for Mach numbers varying from 0 to 0.2 with an interval of 0.05. The parameters set in OSCILOS, are shown in Fig. 3.3.

Table 3.1: Geometric parameters of the numerical Model

PARAMETERS	VALUES	UNITS
Cylindrical model length	3.00	m
Cylindrical model radius	0.10	m
Axial position of the flame sheet	0.30	m
Flame sheet thickness	0.01	m

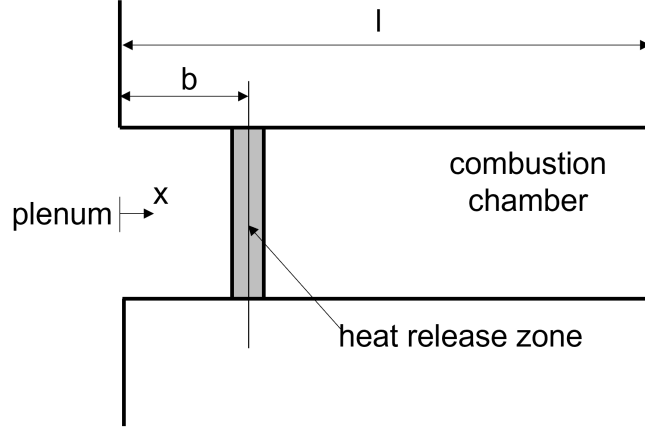
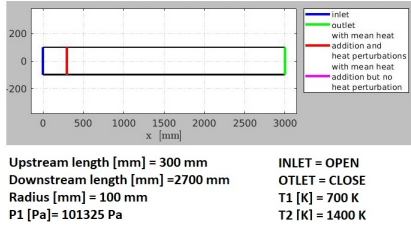
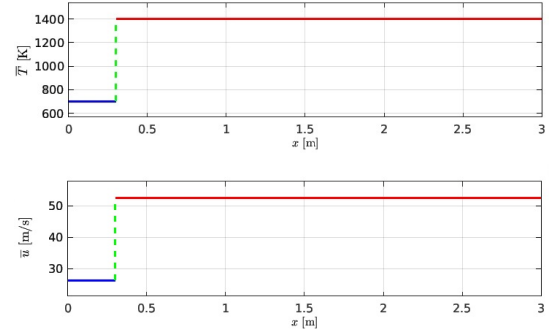


Figure 3.2: Detail of one-dimensional bench-mark geometry adapted by [63]. The gray section represents the flame sheet.

#### CYLINDRICAL DUCT WITH CONSTANT CROSS SECTION



(a)



(b)

Figure 3.3: Settings of OSCILOS Simulator. (a) Geometry of bench-mark burner (b) trend of temperature and velocity with length

### 3.5.2 Numerical setup in Helmholtz solver

To solve the acoustic in the combustion chamber through the Helmholtz solver a three-dimensional code based on the finite element method (FEM) is adopted: COMSOL Multiphysics<sup>®</sup> is the commercial software used [15, 99, 100]. In the acoustic network the unsteady heat release is assumed to be concentrated at a single axial plane  $x = b$  (see Fig. 3.2), called flame sheet. The fluctuation of heat release of Eq. (3.14) is assumed to be related to the oncoming air velocity with a time delay  $\tau$ .

$$\dot{q}'(x) = \dot{Q}'(t)\delta(x - b) \quad (3.29)$$

$$\dot{Q}'(t) = \frac{\rho c^2}{\gamma - 1} \beta u_i'(t - \tau) \quad (3.30)$$

where  $\dot{Q}'(t)$  is the rate of heat release per unit area,  $\beta$  is a non-dimensional parameter, introduced by Dowling and Stow [63], denoting the intensity of heat release and the subscript  $i$  denotes the position upstream the flame sheet.  $\tau$  is defined as the convection

time from fuel injection to its combustion. The term  $\delta(x-b)$  is the Dirac delta, denoting the reciprocal of the thickness of the flame sheet. In the 3D FEM approach, it is not possible to consider the heat release as a flame sheet, so that a thin region for the heat input is considered, as shown in Fig. 3.2. As a consequence, the term  $\delta(x-b)$  is defined as:

$$\delta(x-b) = \begin{cases} 0 & x \leq b - (s/2) \\ (1/s) & b - (s/2) \leq x \leq b + (s/2) \\ 0 & x > b + (s/2) \end{cases} \quad (3.31)$$

where  $s$  is the thickness of the heat release zone and  $b$  is its axial location. In order to define the non-dimensional parameter  $\beta$  of Eq. (3.30), it is necessary to consider a generic geometry in which there is a variation of cross section between plenum and combustion chamber. In this framework, in order to use the flame sheet model, a new flame law, that considers the variation of cross section, must be used.

$$\frac{\hat{Q}}{\bar{Q}} = -k \frac{\hat{m}_i}{\bar{m}_i} e^{-i\omega\tau} \quad (3.32)$$

where  $m$  is the flow rate in the restriction area before the flame sheet and  $k$  is a non-dimensional term used for varying the intensity of the unsteady heat release. Cross sectional area and air density are assumed constant along the restriction area, so that:

$$\frac{\hat{m}_i}{\bar{m}_i} = \frac{\hat{u}_i}{\bar{u}_i} \quad (3.33)$$

Considering that the mean mass flow rate is related to the cross section of the restriction area  $A_{ra}$  through:

$$\bar{m}_i = A_{ra} \bar{u}_i \quad (3.34)$$

the time average of heat release rate per unit area of the combustion chamber is:

$$\bar{Q} = \bar{\rho}_i \bar{u}_i c_p (T_2 - T_1) \frac{A_{ra}}{A_{comb.chamb.}} \quad (3.35)$$

where  $T_1$  and  $T_2$  are the temperatures upstream and downstream of the flame sheet respectively. Combining Eq. (3.29) and Eq. (3.30), we can write:

$$\hat{q}'(x) = -\frac{\rho c^2}{\gamma - 1} \beta u'(t - \tau) \delta(x - b) \quad (3.36)$$

Imposing RHS of Eq. (3.20) equal to monopole source defined in COMSOL ( $Q_{CM}$ ) and dividing it for the density, we obtain:

$$Q_{CM} = -\frac{\gamma - 1}{\rho c^2(\mathbf{x})} \lambda \hat{q}(\mathbf{x}) \quad (3.37)$$

Starting from this formulation, and combining Eq. (3.29), Eq. (3.32), Eq. (3.34) and Eq. (3.35),  $Q_{CM}$  became:

$$Q_{CM} = \lambda \cdot \delta \cdot \beta \cdot \hat{u}_i \cdot e^{\lambda\tau} \quad (3.38)$$

Hence,  $\beta$  is equal:

$$\beta = k\lambda\gamma R(T_2 - T_1) \frac{\rho_i}{\rho \bar{c}^2} \frac{A_{ra}}{A_{comb.chamb.}} \quad (3.39)$$

In this study, the mean flow is characterized by the solely axial velocity vector component, which corresponds to the  $x$  direction ( $u_x$ ). Thus in COMSOL formulation, the monopole source is added on the Eq. (3.38). This additional term is formulated starting from Eq. (3.28) neglecting the terms that do not depend on the axial velocity.

$$Q_{mf} = - \left( -2\lambda u_x \frac{\partial p}{\partial x} + u_x^2 \frac{\partial^2 \hat{p}}{\partial x^2} \right) \frac{1}{\rho c^2} \quad (3.40)$$

The properties of the flow are summarized in Table 3.2. The flame sheet has been positioned at 1/10 of the cylinder length; moreover, the monopole source has been set only in the domain of the flame sheet. The velocity has been imposed in order to set the mean flow in the respective domains (upstream and downstream of the flame sheet) considering them constant along the streamwise direction. To discretize the model an unstructured grid of 18218 elements has been used. For this model, the inlet section has been considered as an open wall (zero acoustic pressure), while the exit section has been considered as a closed wall ( $u' = 0$ ). The simulations have been carried out for Mach numbers varying from 0 to 0.2 with an interval of 0.05.

Table 3.2: Boundary conditions and settings for cylindrical combustor in module Acoustic Pressure and Frequency Domain of COMSOL Multiphysics<sup>®</sup>

PARAMETERS	VALUES	UNITS
$T_{air}$ = air temperature	700	K
$T_2$ = temperature in flame sheet and combustion chamber	1400	K
$p_{air}$ = air pressure	$1 \times 10^5$	Pa
$M_p$ = Mach number in the plenum	0-0.2	
$c_p$ = speed of sound in the plenum	517	m/s
$u_p$ = velocity in the plenum	$M_p c_p$	m/s
$u_2$ = velocity in flame sheet and combustion chamber	$(r_p/r_{cc})u_p$	m/s
$\tau$ = time delay	0.005	s
$\beta$ = factor provides a measure of the intensity of the heat release	0.6	s

### 3.5.3 Numerical validation on simple cylinder

The results obtained for frequency and growth rate are shown in Fig. 3.4, where the results of the Helmholtz analysis (COMSOL) are compared with those obtained by means of OSCILOS. As can be seen, the results obtained with the two solvers are in good agreement. The main difference between the Helmholtz solver (COMSOL Multiphysics<sup>®</sup>) and the low order solver (OSCILOS) is that COMSOL allows the user to discretize much more complex three-dimensional models, giving us compliant results both in the case of mean flow equal to zero and in the presence of mean flow. In accordance with the results obtained by Dowling and Stow [63], the frequency (normalized by  $f_{max} = 166.4031$  Hz) and the growth rate (normalized by  $|GR_{max}| = 8.8878$  1/s) of an unstable mode ( $GR < 0$ ) decrease as the number of Mach in the plenum increases, Fig. 3.4. The two

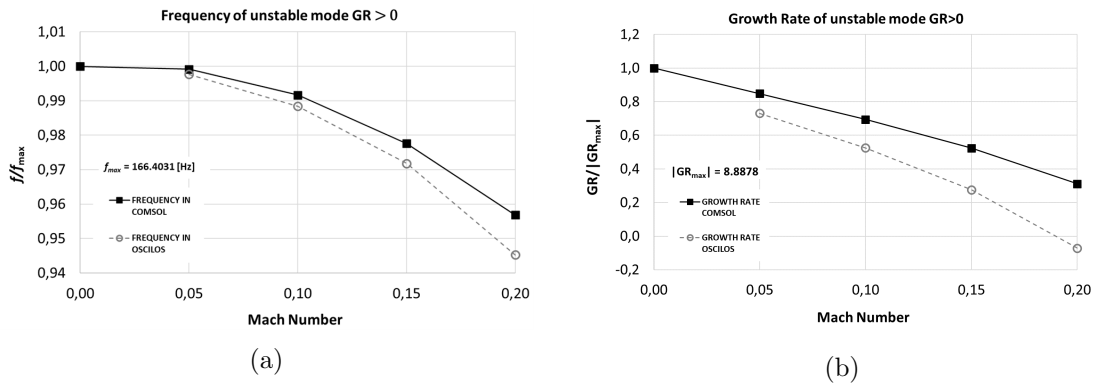


Figure 3.4: Comparison between COMSOL and OSCILOS of unstable mode: (a) Frequency, (b) Growth Rate

solvers (OSCILOS and COMSOL) predict the same frequency values with a maximum error of -1.22% at  $M = 0.2$ . As it can be seen going from  $M = 0.05$  to  $M = 0.2$ , the frequency decreases overall of 4% and 5.8%, respectively, for COMSOL and OSCILOS. On the other hand, the main discrepancies are found for the GR. Indeed, the gap between the curves is 54% at  $M = 0.2$  and GR changes its sign at  $M = 0.2$ , where the mode becomes stable. Also, in the case of stable mode ( $GR > 0$ ), in accordance with the results obtained by low order approach (OSCILOS) the frequency (normalized by  $f_{max} = 294.713$  Hz) and the growth rate (normalized by  $|GR_{max}| = 1.0588$ ) decrease as Mach number in the plenum increases, Fig. 3.5. Differently from the previous case, the frequency and the GR curves show roughly the same gap (=78%). In this case, both COMSOL and OSCILOS show a frequency reduction of 7.6% from  $M = 0$  to  $M = 0.2$ . The discrepancies between the frequencies and the growth rate calculated by using COMSOL and OSCILOS can be due to the fact that in COMSOL a constant density has been considered in the flame sheet.

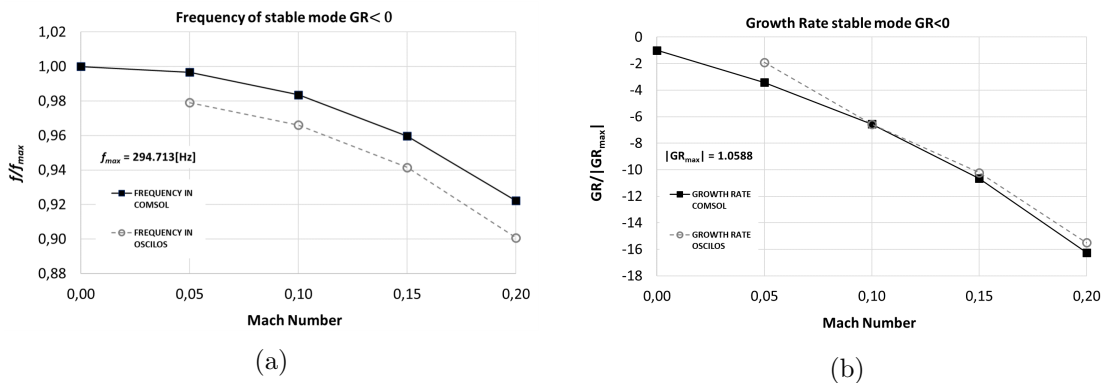


Figure 3.5: Comparison between COMSOL and OSCILOS of stable mode: (a) Frequency, (b) Growth Rate

### 3.5.4 Numerical setup on annular combustor

Once the aforementioned numerical evaluation has been made, a simplified model of an annular combustor has been considered. This model is characterized by a diffusion chamber (plenum) and a combustion chamber, both of them being annular connected to each other thanks to 12 swirled burners. A mixture of air and fuel is injected in the plenum from the outside. The numerical model does not take into account what is present upstream and downstream of the combustor. The dimensions of the various components of the system were determined using the model used by Pankiewitz and Sattelmayer in their study [101]. In the numerical model used in COMSOL Multiphysics<sup>®</sup>, see Fig. 3.6, the burners have been reproduced in a simplified way (ducts with constant cross section area) and the nozzles, located at the end of the combustion chamber, have been omitted. This leads to a simplified geometry characterized by an annular plenum, 12 thin ducts, representing the burners, and an annular combustion chamber. The plenum is characterized by the following dimensions: external diameter  $d_{\text{ext,P}} = 540$  mm and internal diameter  $d_{\text{int,P}} = 334$  mm. The length of the plenum is 200 mm. The burners, which are modeled as thin ducts, show:  $d_B = 26$  mm and length  $l_B = 30$  mm. The combustion chamber consists of an external diameter  $d_{\text{ext,CC}} = 480$  mm and an internal diameter  $d_{\text{int,CC}} = 394$  mm. The length of the combustion chamber is 300 mm.

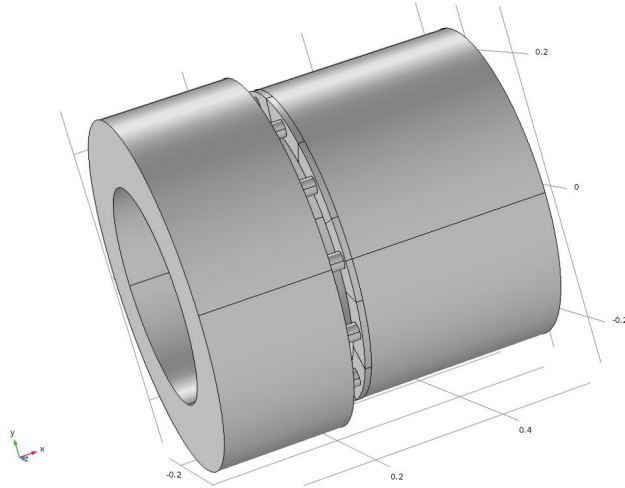


Figure 3.6: Geometry of annular combustor

The plenum inlet and the combustion chamber outlet behave like walls acoustically closed ( $u' = 0$ ). In the plenum, and therefore in the burners, there is the mixture of air and fuel at a controlled temperature of  $T_P = 774$  K. The absolute pressure is assumed constant and equal to  $p_0 = 101325$  Pa. The combustion chamber is modeled as an annular duct at the temperature of  $T_{CC} = 2350$  K. In the first part of the combustion chamber, a sheet of 0.01 mm has been introduced to model the flame as proposed by Dowling and Stow [63]. The density of the flow inside both the plenum and the burners is equal to  $0.45 \text{ kg/m}^3$ , whereas, in the combustion chamber the density is equal to  $0.15 \text{ kg/m}^3$ . The speed of sound inside both the plenum and the burners is equal to  $556 \text{ m/s}$ , whereas in the combustion chamber  $c_2 = 945.2 \text{ m/s}$ . A grid independence study has been performed. Three unstructured grids have been generated, see Fig. 3.7a, 3.7b and 3.7c. Table 3.3 summarizes their number of cells and the values of frequency and

growth rate obtained for the third vibrating mode, in the case of Mach number equal to zero. We note the independence of the frequencies from the number of elements of the grid.

Table 3.3: Grid influence on Frequencies and Growth Rate

GRID TETRAHEDRON ELEMENTS	FREQUENCY [Hz]	GROWTH RATE [1/s]
68601	752.59	0.0766
131671	752.40	0.0783
183515	752.29	0.0799

This is explained by the fact that the wavelengths involved are sufficiently large compared to the cell size used, thus making its influence negligible. It is worth to highlight that a grid with less than 68601 numbers of elements, is not able to discretize correctly the flame sheet zone. Finally, the unstructured grid, made of 68601 tetrahedral elements, has been chosen for further simulations. The mean flow in the plenum is calculated by the Mach number (Mach number which varies from 0 to 0.125 with a range equal to 0.025) and the speed of sound imposed in the plenum. Pankiewits and Sattelmayer in [101] consider a model with a Mach number equal to 0.017, while in this thesis a wide range of values has been investigated. In the combustion chamber, the mean flow is derived by applying the continuity equation,  $u_2 = (u_p \rho_p A_p) / (\rho_2 A_2)$ . The velocity in the 12 burners is considered equal to the velocity in the plenum; its variation in the passage between the plenum and the swirler is neglected in this preliminary no zero Mach number study.

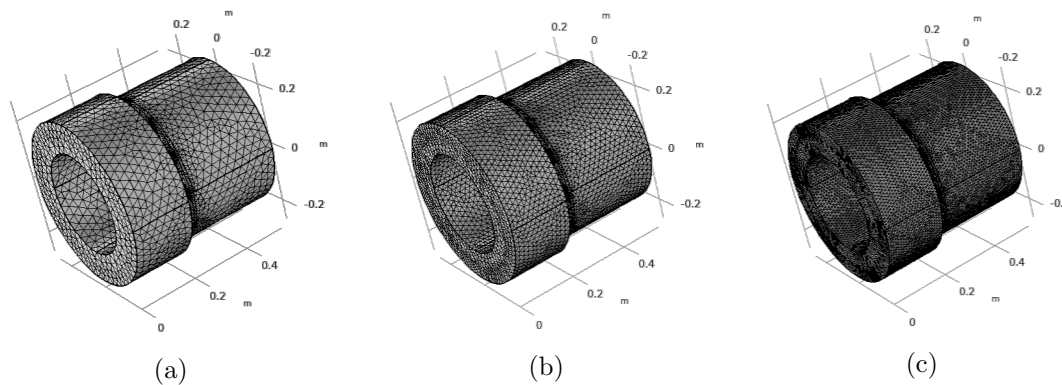


Figure 3.7: Unstructured grid of Annular combustor: (a) 68601 tetrahedron elements, (b) 131671 tetrahedron elements, (c) 183515 tetrahedron elements

### 3.5.5 Results of the annular combustor

The influence of the Mach number on the third stable mode is shown in Fig. 3.8. The Mach number in the plenum has been changed from 0 to 0.125. This range of Mach number and the thermodynamic properties of the flow is representative of the flow field at the inlet of real gas burner applications (i.e.,  $u=80$  m/s). The results of the sensitivity analysis on the frequency and the growth rate of the third stable mode, by varying the Mach number in the plenum, are shown in Fig. 3.8 and summed up in Table 3.4. Looking at Table 3.4, the frequency is not affected by great variations (at least 1.4%), on the



contrary, the GR undergoes a remarkable variation. As shown in Fig. 3.8, the frequency (Blue line) and the growth rate (Red line) decrease while the Mach number increases, according to Dowling and Stow [63]. This means that in this case, the third stable mode becomes more stable by introducing the mean flow.

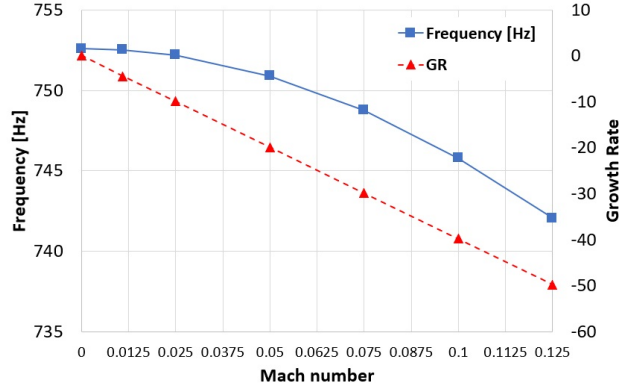


Figure 3.8: Trend of Frequency and Growth Rate in Annular Model

Table 3.4: Frequency and Growth Rate of the third stable mode by varying the Mach Number in the plenum.

MACH NUMBER	FREQUENCY [Hz]	GROWTH RATE [1/s]
0	752.5946	0.0776
0.011	752.5242	-4.4235
0.025	752.1855	-9.9192
0.050	750.8982	-19.8922
0.075	748.7584	-29.8381
0.100	745.7986	-39.7804
0.125	742.0488	-49.7944

Helmholtz solver has been used to study the effects of various mean flow magnitudes on frequency and growth rate on a real annular combustor. The mean flow is introduced in a 3D model for the first time. Both the frequency and the relative Growth Rate drop as the Mach number in the plenum rises. This indicates that the burner instability is reduced as a result of the mean flow. The oscillation mode of the combustor is stabilized by the mean flow because it causes energy dissipation in the burner.

## Chapter 4

# Computational Fluid Dynamic (CFD) mathematical models

In this chapter, the mathematical models that are used for the Computational Fluid Dynamic (CFD) analysis of the combustion are reviewed. Firstly, the equations of non-reacting system are presented. Then, the approaches that involve the solution of Navier-Stokes equations in turbulent regime are summarized. After, the Partially Premixed combustion model is explained. Lastly, in order to close the combustion model, the prediction of turbulent flame speed by means the Zimont model is reported.

### 4.1 Computational Fluid Dynamic (CFD) simulations

Computational Fluid Dynamic (CFD) uses numerical analysis and data structures to study fluid flow in terms of physical phenomena, such as heat transfer, radiation, and chemical reactions. The aim is to solve the flow field and evaluate other physical quantities in each point of the discretized computational domain. CFD has several advantages over experiments:

- lower cost in terms of time,
- possibility to simulate dangerous conditions,
- possibility to simulate the system in real scale in order to eliminate scale-up problems,
- analysis of the phenomena and quantities that are not always easily explored or measured,
- simulation before prototype construction.

However, CFD, like all numerical simulation approaches, cannot completely replace experimental campaigns. CFD is actually based on theories, approximations, and hypotheses that need to be experimentally verified.

#### 4.1.1 Mathematical basis of CFD

CFD simulations are based on the solution of the Navier-Stokes equations. Given a control volume  $V$  bounded by a surface  $S$  (Fig. 4.1), denoted by  $\Psi$  a generic extensive

physical quantity, and by  $\psi = \Psi/\rho V$  the corresponding intensive physical quantity, where  $\rho$  represents the density of the fluid, the conservation equation of  $\Psi$  in integral form can be expressed as follows:

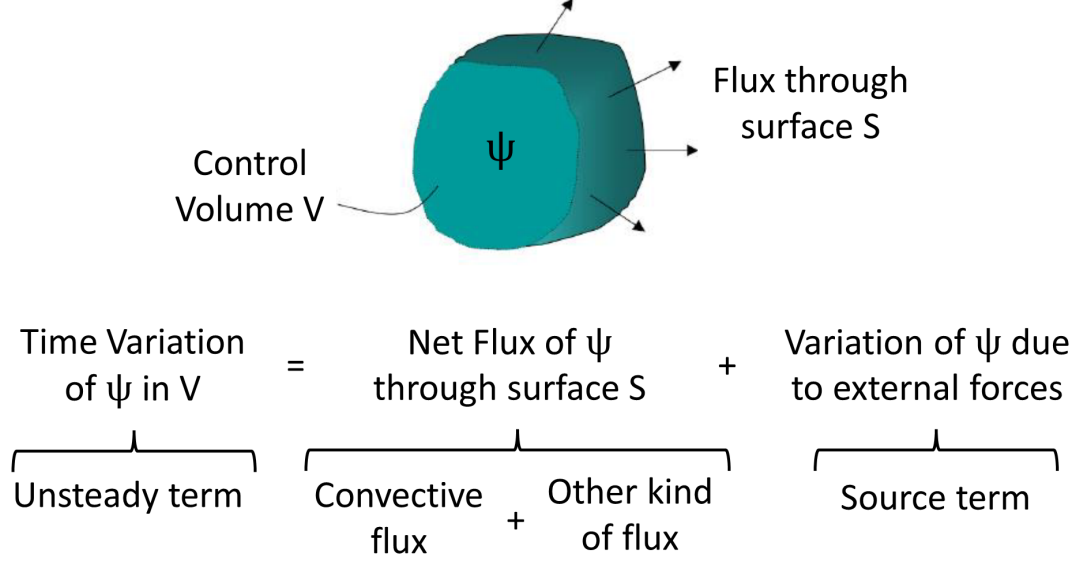


Figure 4.1: Graphical representation of a generic volume  $V$  and the generic conservation equation of an extensive physical quantity  $\Psi$ .

$$\frac{\partial}{\partial t} \int_V \rho \psi dV = - \oint_S \rho \psi \mathbf{u} \cdot \mathbf{n} dS + \oint_S D_\psi \nabla \psi \cdot \mathbf{n} dS + \int_V S_\psi dV \quad (4.1)$$

where  $\mathbf{u}$  is the velocity vector,  $D_\psi$  is the diffusion coefficient of  $\psi$ ,  $\mathbf{n}$  is the unit vector normal to the infinitesimal surface element  $dS$  pointing outward from  $V$  and  $S_\psi$  is the source term that takes into account the generation of  $\psi$  inside  $V$ . Eq. (4.1) in differential form becomes:

$$\frac{\partial \rho \psi}{\partial t} = -\nabla \cdot (\rho \psi \mathbf{u}) + \nabla \cdot (D_\psi \nabla \psi) + S_\psi \quad (4.2)$$

The fluid flow and heat release is regulated by conservation equations, i.e.:

- mass conservation equation

$$\frac{\partial \rho}{\partial t} = -\nabla \cdot (\rho \mathbf{u}) \quad (4.3)$$

Dealing with chemical species, said  $Y_k$  the mass fraction of the generic species in the mixture,  $u_i$  the generic component of the velocity vector,  $\dot{R}_k$  the rate of production of the species,  $\mu$  the dynamic viscosity and  $Sc_k$  the Schmidt number of the species with  $k = 1, \dots, K$ , using Eq. (4.4) and Eq. (4.5):

$$Y_k = \frac{\rho_k}{\rho} \quad (4.4)$$

$$\sum_{k=1}^K Y_k = 1 \quad (4.5)$$

where  $\rho_k$  is the partial density of generic species, we can rewrite Eq. (4.3) as follows:

$$\frac{\partial(\rho Y_k)}{\partial t} = -\frac{\partial(\rho Y_k u_i)}{\partial x_i} + \frac{\partial}{\partial x_i} \left( \frac{\mu}{Sc_k} \frac{\partial Y_k}{\partial x_i} \right) + \rho \dot{R}_k \quad (4.6)$$

- momentum conservation equations

$$\frac{\partial(\rho \mathbf{u})}{\partial t} = -\nabla \cdot (\rho \mathbf{u} \mathbf{u}) - \nabla p + \nabla \bar{\bar{\tau}} + \rho \mathbf{g} + \mathbf{F} \quad (4.7)$$

where  $p$  is the static pressure,  $\rho \mathbf{g}$  is the gravitational body force,  $\mathbf{F}$  is the external body force and  $\bar{\bar{\tau}}$  is the stress tensor. Under the hypothesis of a Newtonian fluid, that meets the Stokes hypothesis,  $\bar{\bar{\tau}}$  can be written as follows:

$$\bar{\bar{\tau}} = \mu \left[ (\nabla \mathbf{u} + \nabla \mathbf{u}^T) - \frac{2}{3} (\nabla \cdot \mathbf{u}) \bar{\bar{I}} \right] \quad (4.8)$$

where  $\bar{\bar{I}}$  is the unit tensor and the RHS of Eq. 4.8 represents the effect of volume dilatation.

- energy conservation equation

$$\frac{\partial(\rho E)}{\partial t} = -\nabla \cdot (\mathbf{u}(\rho E + p)) + \nabla \cdot \left( k \nabla T - \sum h_i J_i + (\bar{\bar{\tau}}) \right) + \rho \mathbf{g} \cdot \mathbf{u} + S_h \quad (4.9)$$

where  $k$  is the thermal conductivity,  $E$  is the total internal energy for unit mass equal to the sum of internal energy for unit mass  $e = h - p/\rho$  ( $h$  static enthalpy) and kinetic energy  $u^2/2$ ,  $h_i$  is the enthalpy of  $i$ -th species,  $S_h$  is the energy or heat source due to the chemical reaction in the case of reactive flows and  $J_i$  is the diffusion flux of the  $i$ -th species in the case of turbulent flows equal to:

$$J_i = - \left( \rho D_{i,m} + \frac{\mu_t}{Sc_t} \right) \nabla Y_i - D_{T,i} \frac{\nabla T}{T} \quad (4.10)$$

where  $T$  is the static temperature,  $D_{T,i}$  is the thermal mass diffusion coefficient of the  $i$ -th species,  $Sc_t = \mu_t/(\rho D_t)$  is the Schmidt number for turbulent flux ( $D_t$  is the diffusion coefficient for turbulent flux and  $\mu_t$  is the turbulent viscosity) and  $D_{i,m}$  is the mass diffusion coefficient of the  $i$ -th species equal to:

$$D_{i,m} = \frac{1 - X_i}{\sum_{i,j \neq i} \frac{X_i}{D_{i,j}}} \quad (4.11)$$

where  $D_{i,j}$  is the diffusion coefficient of the  $i$ -th species in the  $j$ -th species and  $X_i$  is the molar fraction of the  $i$ -th species.

In case of chemical reactions, some additional expressions are necessary, and their formulation depends on the approach used. If models with a finite number of reactions are used, it will be necessary to write as many conservation equations as the chemical species involved. If, however, a mixture fraction approach is chosen, it will only be necessary to write two transport equations: one for the mixture fraction and one for its variance.

### 4.1.2 Solution approach to turbulent flows

In the turbulent regime, the random nature of the quantities involved makes it necessary to employ simplified approaches. In general, we distinguish different levels of solution of the Navier-Stokes equations:

- **RANS (Reynolds-Averaged Navier-Stokes equations)** This approach involves the solution of the Navier-Stokes equations appropriately averaged over time, so as to describe the spatial variation of only the average quantities. The averaging operation introduces some unknown terms (including terms that quantify the thermal release due to the chemical reaction and the velocity of conversion of chemical species) that must be evaluated with appropriate models, often of empirical nature and derived on the basis of observation of the physical phenomena. For unsteady phenomena, Unsteady RANS equations can be solved. In this case, the averaging time should be sufficiently small to follow the unsteady phenomenon but sufficiently large for averaging
- **LES (Large Eddy Simulation)** It allows to simulate the turbulent fluctuations associated with the largest spatial (and temporal) scales (of the order of the integral scale). Motion at the smallest spatial scales (Kolmogorov) is solved by models similar to those used for RANS: the use of these models limited to the smallest spatial scales is certainly more efficient given their intrinsic properties of isotropy and ability to be less affected by macroscopic flow characteristics as well as boundary conditions. The equations used in the LES approach are obtained by a filtering operation of the exact Navier-Stokes equations, as well as a mathematical manipulation of them, in order to “remove” from the dynamics of the simulated flow the vortices of a scale smaller than the characteristic scale of the filter used, which is usually fixed according to the sizing of the grid employed for the discretization of the studied domain. The LES approach typically requires significant computational resources, due to the need to accurately resolve the vortices in both the space and time domains.
- **DNS (Direct Numerical Simulation)** It provides for the direct complete non-stationary, three-dimensional solution of the instantaneous Navier-Stokes equations for all spatial scales without the aid of any additional model. The calculation is able to capture all fluctuations of the extensive quantities and directly quantify their effects.

### 4.1.3 Combustion Model: Partially premixed

ANSYS Fluent<sup>®</sup> (commercial CFD code) proposes a partially premixed combustion model, based on both the non-premixed type model and the premixed type model. It is used to simulate reactant systems characterized by gas mixtures that are not perfectly premixed, as well as with an inhomogeneous distribution of the equivalence ratio. The partially premixed combustion model requires the instantaneous thermochemical state of the fluid to be related to two scalar quantities whose transport equations are solved: the mixture fraction (mixture fraction,  $\xi$ ) and the flame front progress variable (reaction progress variable,  $\theta$ ). The first is defined as follows:

$$\xi = \frac{Z_i - Z_{i,ox}}{Z_{i,fuel} - Z_{i,ox}} \quad (4.12)$$

where  $Z_i$  is the elemental mass fraction of the  $i$ -th element and subscript  $ox$  and  $fuel$  denote that the mass fraction is evaluated in relation to the initial composition of the oxidizer and fuel, respectively. Under the hypothesis that all chemical species have the same diffusion coefficient, which is the case of turbulent flow in which turbulent diffusion overwhelms molecular diffusion, we can write the transport equation of average mixture fraction  $\bar{\xi}$  as follows:

$$\frac{\partial}{\partial t}(\rho\bar{\xi}) + \nabla \cdot (\rho\mathbf{u}\bar{\xi}) = \nabla \cdot \left( \frac{\mu_t}{\sigma_t} \nabla \bar{\xi} \right) + S_m + S_{user} \quad (4.13)$$

where the source term  $S_m$  is due solely to transfer of mass into the gas phase from liquid fuel droplets or reacting particles and  $S_{user}$  is an eventual user-defined source term. In addition, ANSYS Fluent<sup>®</sup>, solves a conservation equation for the mixture fraction variance,  $\bar{\xi'^2}$  defined, according to Reynolds decomposition, as  $\xi' = \xi - \bar{\xi}$ :

$$\frac{\partial}{\partial t}(\rho\bar{\xi'^2}) + \nabla \cdot (\rho\mathbf{u}\bar{\xi'^2}) = \nabla \cdot \left( \frac{\mu_t}{\sigma_t} \nabla \bar{\xi'^2} \right) + C_g \mu_t (\nabla \bar{\xi}^2) - C_d \rho \frac{\epsilon}{k} \bar{\xi'^2} + S_{user} \quad (4.14)$$

where the default values for the constants  $\sigma_t$ ,  $C_g$ , and  $C_d$  are 0.85, 2.86, and 2.0, respectively. The potential of the combustion modeling approach based on the evaluation of the mixture fraction,  $\xi$ , can be found on the fact that, under the hypothesis of chemical equilibrium, all of the thermochemical scalar quantities ( $\psi$ ), such as the mass fractions of the chemical species involved in the system, density and temperature at each point in the computational domain, are related to the instantaneous value of the mixture fraction,  $\xi$ :

$$\psi_i = \psi_i(\xi) \quad (4.15)$$

Actually, this is true only in the case of adiabatic systems. In the non-adiabatic hypothesis (including systems with radiation) we have that these thermochemical scalar quantities are functions not only of  $\xi$ , but also of the local value of enthalpy. Thus:

$$\psi_i = \psi_i(\xi, h) \quad (4.16)$$

This means that, in this case, solving an additional transport equation related to the mean enthalpy,  $\bar{h}$ , is required:

$$\frac{\partial}{\partial t}(\rho\bar{h}) + \nabla \cdot (\rho\mathbf{u}\bar{h}) = \nabla \cdot \left( \frac{k_t}{c_p} \nabla \bar{h} \right) + S_h \quad (4.17)$$

where  $S_h$  is the source term related to radiation, heat transfer through walls or other, and  $k_t$  is the turbulent kinetic energy. Indeed, the predictions made during simulation by the ANSYS Fluent<sup>®</sup> code for turbulent reactant flow regard the average values of these thermochemical scalar quantities that exhibit fluctuations over time. The manner in which the average value is related to the instantaneous value of these quantities depends on the interaction model between chemistry and turbulence. The combustion model of the partially premixed combustion model, as well as the non-premixed type, takes this interaction into account through a statistical approach, i.e., by means of a probability density function ( $PDF$ ) that depends greatly on the nature of the fluctuations of  $\xi$ . In our case studies, the shape of the Probability Density Function,  $PDF(\xi)$ , is approximated by means of the  $\beta$ -function, implemented in ANSYS Fluent<sup>®</sup> and defined as follows:

$$PDF(\xi) = \frac{\xi^{\alpha^*-1}(1-\xi)^{\beta^*-1}}{\int \xi^{\alpha^*-1}(1-\xi)^{\beta^*-1}d\xi} \quad (4.18)$$

where:

$$\alpha^* = \bar{\xi} \left[ \frac{\bar{\xi}(1-\bar{\xi})}{\bar{\xi}'^2} - 1 \right] \quad (4.19)$$

$$\beta^* = (1-\bar{\xi}) \left[ \frac{\bar{\xi}(1-\bar{\xi})}{\bar{\xi}'^2} - 1 \right] \quad (4.20)$$

In premixed combustion, the reaction progress variable  $\theta$ , is used to model the flame front propagation. In particular, flame front propagation is modeled by solving a transport equation for the mean reaction progress variable  $\bar{\theta}$ :

$$\frac{\partial}{\partial t}(\rho\bar{\theta}) + \nabla \cdot (\rho\mathbf{u}\bar{\theta}) = \nabla \cdot \left( \left( \frac{k}{c_p} + \frac{\mu_t}{S_{c_t}} \right) \nabla \bar{\theta} \right) + \rho S_c \quad (4.21)$$

where the Turbulent Schmidt number  $S_{c_t}$  is equal to 0.7,  $k$  is laminar thermal conductivity of the mixture, and  $S_c$  is the Product Formation Rate (PFR) that represents the reaction progress source term ( $s^{-1}$ ). In the case of non-adiabatic premixed combustion model, ANSYS Fluent solves an energy transport equation in order to account for any heat losses or gain within the system. The energy equation in terms of sensible enthalpy,  $h$ , for the fully premixed combustion is as follows:

$$\frac{\partial}{\partial t}(\rho h) + \nabla \cdot (\rho\mathbf{u}h) = \nabla \cdot \left( \frac{k + k_t}{c_p} \nabla h \right) + S_{h,chem} + S_{h,rad} \quad (4.22)$$

where  $S_{h,rad}$  is the heat loss due to the radiation and  $S_{h,chem}$  represents the heat gain due to the chemical reaction:

$$S_{h,chem} = \rho S_c H_{comb} Y_{fuel} \quad (4.23)$$

where  $H_{comb}$  is the lower heating value of fuel and  $Y_{fuel}$  is mass fraction of unburnt fuel in the mixture. The progress variable is defined as the normalized sum of the product species:

$$\theta = \frac{\sum_{i=1}^n Y_i}{\sum_{i=1}^n Y_{i,eq}} \quad (4.24)$$

where  $n$  is the number of product species,  $Y_i$  is the mass fraction of  $i$ -th product species and  $Y_{i,eq}$  is the equilibrium mass fraction of product species  $i$ -th. Based on this definition, the variable takes value  $\theta = 1$  upstream of the flame front, where the products of combustion occur,  $\theta = 0$  downstream of the flame front, where the unburned mixture is present, and  $0 < \theta < 1$  inside the flame front. Under the hypothesis of thin flame such that only the reactants and combustion products are present, non-adiabatic system and chemical equilibrium, the average thermochemical scalar quantities ( $\bar{\psi}_i$ ), such as the mass fractions of the chemical species involved, density and temperature, can be calculated by predicting the values of  $\bar{\xi}$ ,  $\bar{\xi}'^2$ ,  $\bar{h}$  and  $\bar{\theta}$  at each point in the computational domain. In particular:

$$\bar{\psi}_i = \bar{\theta} \int_0^1 \psi_{i,b}(\xi, \bar{h}) PDF(\xi) d\xi + (1-\bar{\theta}) \int_0^1 \psi_{i,u}(\xi, \bar{h}) PDF(\xi) d\xi \quad (4.25)$$

where subscripts  $u$  and  $b$  identify the reactant and burned mixture, respectively. Since, under the above hypotheses, the shape of the PDF is a function only of  $\bar{\xi}$  and  $\bar{\xi}'^2$ , by predicting the values of these quantities in each point of the computational domain, it is possible to derive the shape of the PDF and consequently the average values of the mass fractions of the involved chemical species, density, and temperature by means of Eq. (4.25). Under the hypothesis of a system in non adiabatic chemical equilibrium, the above thermochemical scalar quantities are solely a function of  $\bar{\xi}$ ,  $\bar{\xi}'^2$ , and  $\bar{h}$ , in order to economize time in the computational processes, look-up tables, generated in a pre-processing phase, are used. Thus, during the simulation, these tables are used by entering with the values predicted by the computational code of  $\bar{\xi}$ ,  $\bar{\xi}'^2$  and  $\bar{h}$  in the generic point of the computational domain and, by interpolation, the average value of the scalar quantity ( $\bar{\psi}_i$ ) is obtained (see Fig. 4.2).

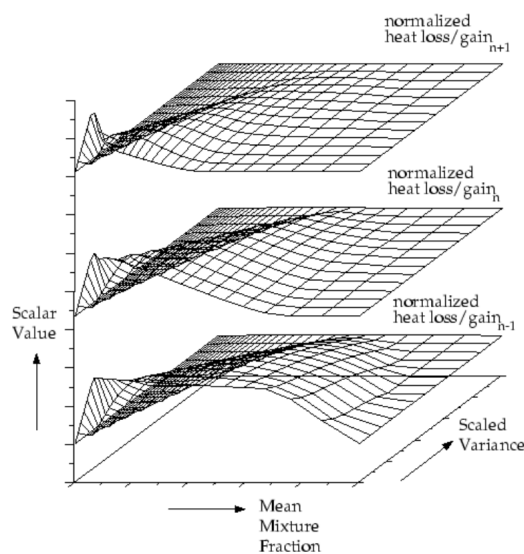


Figure 4.2: Visual Representation of a Look-Up Table for the Scalar  $\bar{\psi}_i$  as a Function of  $\bar{\xi}$  and  $\bar{\xi}'^2$  and  $\bar{h}$  in Non-Adiabatic in chemical equilibrium Systems.

However, the Steady Diffusion Flamelet approach was used in order to model the non-equilibrium chemical conditions of the reactant mixture induced by the stretching of the flame due to the interaction between the flame and the field of motion external turbulence. The approach, using flamelets, allows us to consider the turbulent flame brush as a discrete set of laminar flame fronts, thin and locally one-dimensional, called flamelets. Under this assumption, the reaction chemistry is described by two parameters, i.e., the mixture fraction,  $\xi$ , and a parameter called scalar dissipation,  $\chi$ , defined as follows:

$$\chi = 2D_c|\nabla\xi|^2 \quad (4.26)$$

where  $D_c$  is a characteristic diffusion coefficient. It is necessary to emphasize that the Steady Diffusion Flamelet Model is limited to modeling relatively fast chemical kinetics. To capture the effects associated with all reactions characterized by larger time scales of kinetics, such as that typical of the formation of  $NO_x$ , we turn to the Unsteady Diffusion Flamelet Model approach. Since the chemical equilibrium assumption is not considered, we cannot calculate the thermochemically averaged scalar quantities using Eq. (4.25),



but only with Eq. (4.27), in order to take into account their dependence on  $\bar{\xi}$ ,  $\overline{\xi'^2}$ ,  $\bar{h}$  and on the value of  $\chi$  at the stoichiometric mixture fraction  $\xi_{st}$ .

$$\begin{aligned} \bar{\psi}_i = & \bar{\theta} \iint \psi_{i,b}(\xi, \bar{h}, \chi_{st}) PDF(\xi, \chi_{st}) d\xi d\chi_{st} + \\ & + (1 - \bar{\theta}) \iint \psi_{i,u}(\xi, \bar{h}, \chi_{st}) PDF(\xi, \chi_{st}) d\xi d\chi_{st} \end{aligned} \quad (4.27)$$

Since in ANSYS Fluent<sup>®</sup>,  $\xi$  and  $\chi$  are considered statistically independent, the  $PDF(\xi, \chi_{st})$  can be simplified as  $PDF_{\xi}(\xi)PDF_{\chi}(\chi_{st})$ . For  $PDF_{\xi}(\xi)$  a  $\beta$ -function is assumed as seen above (see Eq. (4.20)), while  $PDF_{\chi}(\chi_{st})$  is approximated, neglecting the fluctuations of  $\chi_{st}$ , with a delta-function  $PDF_{\chi} = \delta(\chi - \bar{\chi})$ . Again, in order to reduce computational time, look-up tables, generated in a pre-processing phase, are used for the calculation of average thermodynamic scalar quantities.

#### 4.1.4 Turbulent flame speed: Zimont model

In order to close the premixed combustion model the prediction of turbulent flame speed  $U_t$  normal to the mean surface of the flame has been computed by means the Zimont model:

$$U_t = A(u')^{3/4} U_l^{1/2} \alpha^{-1/4} l_t^{1/4} = A u' (\tau_t / \tau_c)^{(1/4)} \quad (4.28)$$

where  $A$  is the model constant,  $u'$  is the velocity fluctuation,  $U_l$  is the laminar flame speed,  $\alpha = k/(\rho c_p)$  is the thermal diffusivity of the unburnt mixture,  $l_t$  is the turbulence length scale,  $\tau_t = l_t/u'$  is the turbulence time scale and  $\tau_c = \alpha/U_l^2$  is the chemical time scale. The turbulence length scale is as follows:

$$l_t = C_D \frac{(u')^3}{\epsilon} \quad (4.29)$$

where  $\epsilon$  is the turbulence dissipation rate. When the partially premixed model is used, the laminar flame speed  $U_l$  is calculated by means the linear polynomial function of  $\xi$  integrated in the software and validated for unburnt mixture temperature between 298 and 800 K, and pressure between 1 and 40 bar. The model is based on equilibrium of vortices of small scale inside the flame front, in order to make the turbulent flame speed function of only the largest turbulent scale. For the model constant,  $A$ , and for  $C_D$  were used the default values of 0.52 and 0.37, respectively.

The ‘‘partially premixed’’ combustion model is often used in Fluent also in the case of fully premixed gas turbine burners because it offers greater flexibility in modeling the combustion process. The premixed combustion model allows to analyze, in post-processing: the progress variable,  $\theta$ ; the product formation rate,  $PFR$ ; the laminar flame speed,  $U_l$ ; and turbulent flame speed,  $U_t$ ; but it gives no information about the composition of the mixture. Instead, the partially premixed combustion model, considering also species transport allows one to evaluate the concentration of species in the mixture. The fuel concentration is needed to calculate the heat release rate and the reaction rate developed in the combustion chamber by defining a custom field function. The calculation of these parameters is necessary to introduce the heat source inside the Helmholtz solver in order to simulate a more accurate heat distribution inside the combustion chamber.

## Chapter 5

# CFD Simulations of burners fueled by methane and hydrogen

The combustion with hydrogen, as previously described, alters the behavior of flame shape and its interaction with the combustor. In this chapter the main advantages and disadvantages related to combustion with hydrogen are highlighted by carrying out a thermo-fluid dynamic study on two stabilized lean-premixed lab-scale burners. These burners have been simulated by mean of a commercial CFD software ANSYS Fluent<sup>®</sup>. Different types of fuel composition are analyzed: injection of methane only, injection of a mixture of methane enriched with hydrogen, and injection of pure hydrogen. In the numerical analysis of the reacting system with the combustion of methane, methane enriched with hydrogen, and pure hydrogen, temperature, density, axial velocity, and species concentration distributions inside the combustion chamber are considered. Part of this chapter on Louisiana State University burner is already published in [102]. The other part on the Vanderbilt University burner is published in [103]. The investigation on these burners is developed in partnership with ANSALDO ENERGIA.

### 5.1 Premixed Louisiana Laboratory burner

As first lab-scale burner, the Louisiana State University's swirled premixed burner has been studied [102]. Several author studied experimentally and numerically this burner fueled by pure methane mixture [47, 104–106]. The geometry of the Louisiana burner is showed in Figure 5.1 and Fig. 5.2.

The axial swirler (Fig. 5.3) consists of 45° swirl vanes with 8 straight blades screws on a cylindrical center body that extends from inlet section to combustion chamber outlet (dump plane). The center body is characterized by a variable cross section. Indeed, its inner diameter decreases from 19.05 mm (at the air inlet section) to 12.7 mm (at a distance of 76.2 mm from the dump plane). Moreover,  $D = 12.7$  mm is assumed as the burner characteristic dimension. The axial position of the swirler can change in a range imposed by the lead screw on the center body. In the configuration considered in this study the swirler is placed in the position farthest from the damp plane corresponding to  $14D$  from it. The swirler is characterized by a geometric Swirl Number  $S_g = 0.82$ , as defined by Eq. (5.1).

$$S_g = \frac{2}{3} \left( \frac{1 - (D_{in,sw}/D_{out})^3}{1 - (D_{in,sw}/D_{out})^2} \right) \tan \zeta \quad (5.1)$$

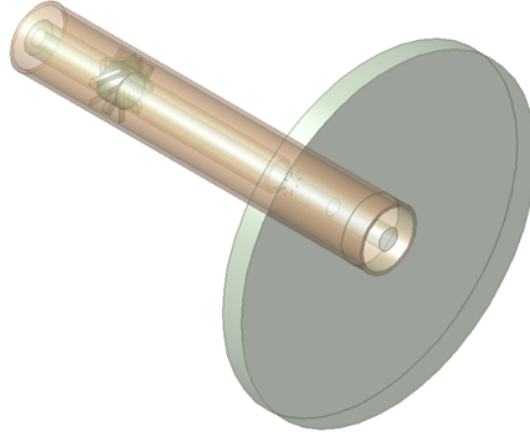


Figure 5.1: Isometric view of the Louisiana State University swirled premixed burner.

where  $D_{in,sw} = 20.96$  mm is the swirler inner diameter,  $D_{out} = 34.93$  mm is the outer diameter of the air delivery pipe and  $\zeta = 45^\circ$  is the swirl angle. Furthermore, the swirl vane has an axial dimension of 12.70 mm and blade height, and thickness equal to 5.08 mm and 2.38 mm, respectively. The fuel mixture is injected through 8 equally spaced holes, with a diameter of 0.7874 mm (see Fig. 5.4a), located downstream of the backward facing step due to the cross section restriction of the center body, exactly 9.53 mm from it (see Fig. 5.2, 5.4b). Moreover, the fuel injection holes are inclined  $11.46^\circ$  with respect to the radial direction (see Fig. 5.4a).

### 5.1.1 Numerical setup

The Louisiana burner geometry developed in ANSYS Fluent<sup>®</sup> is composed by the cylindrical duct (as stated in Section 5.1) that contains the axial swirler and the cylindrical domain for combustion zone downstream of the dump plane with a radius and axial dimension equal to  $12D$  and  $20D$  respectively (see Fig. 5.5).

For the non-reacting flow (only air), the *Reynolds Stress Model* (RSM) has been used as turbulence model and the hypothesis of incompressible and adiabatic flow has been assumed considering atmospheric operating conditions (see Table 5.1). Among turbulence models provided in ANSYS Fluent<sup>®</sup>, the RSM has been used since it has showed the best results in terms of velocity profiles with respect to the experimental ones. This can be explained since the RSM takes into account the anisotropy of the turbulence, which allows a good simulation of strongly swirled flows. Moreover, a pressure-based solver with a SIMPLE pressure-velocity coupling scheme has been used. Spatial discretization operator are second order accurate (first order for turbulence equations). Time integration has been performed by means of first order implicit scheme: a time step size  $\Delta t = 10^{-2}$  s has been defined in order to take into account the non-stationary phenomena related to the Precessing Vortex Core (PVC). Indeed, as evidenced by experimental activities in [47, 106], the PVC for the non-reacting flow is characterized by a frequency equal to 3 Hz.

Referring to the reacting flow simulations, a *Partially Premixed Combustion Model* is

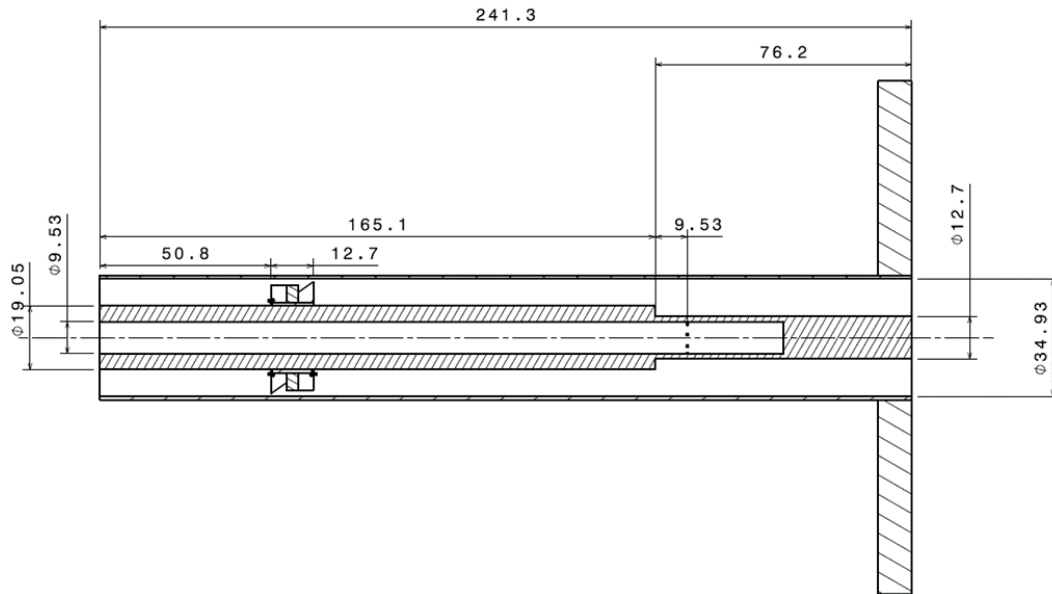


Figure 5.2: Axial section of the Louisiana State University swirled premixed burner.

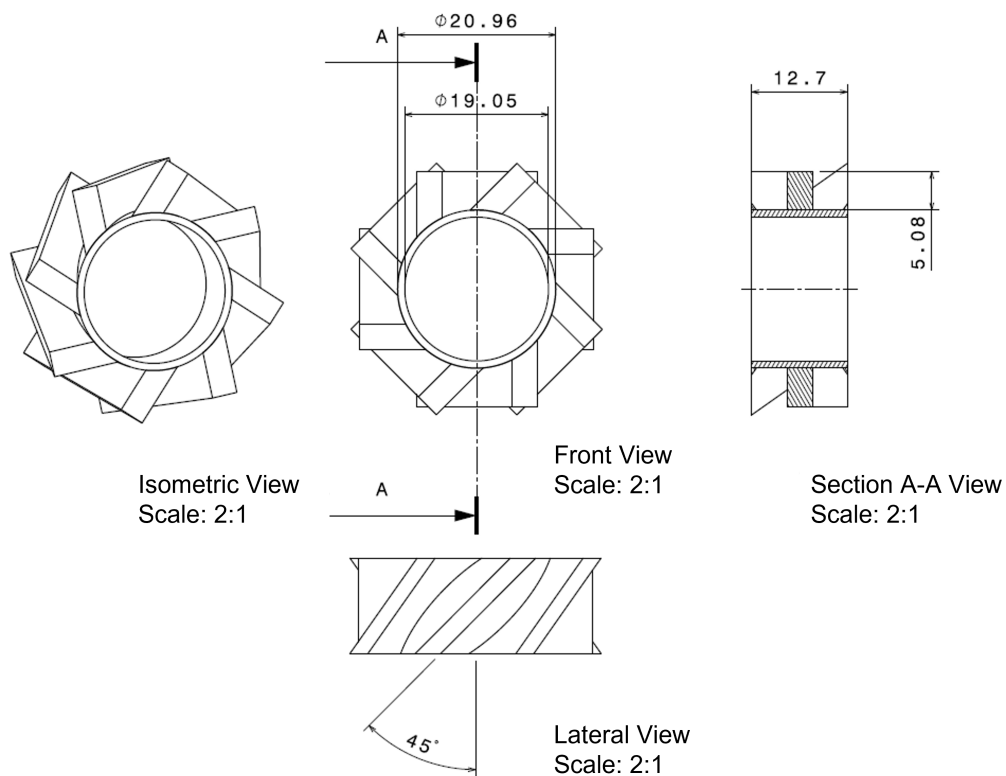


Figure 5.3: Axial swirler of the Louisiana State University swirled premixed burner.

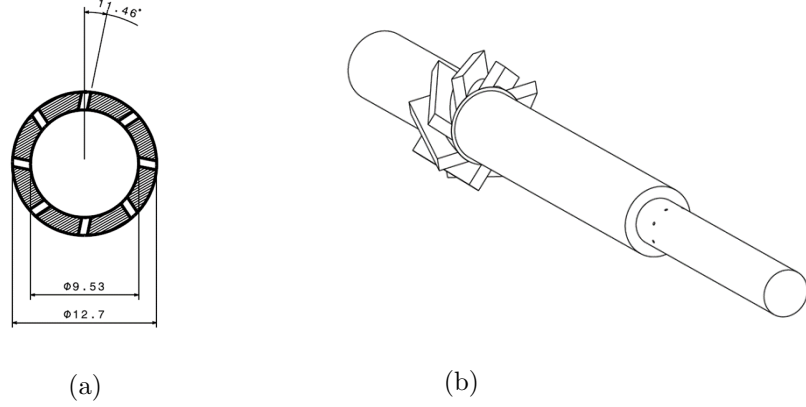


Figure 5.4: Louisiana burner: (a) fuel injection holes (dimension in [mm]) (b) Isometric view center body. The injection holes are located backward of the cross section restriction.

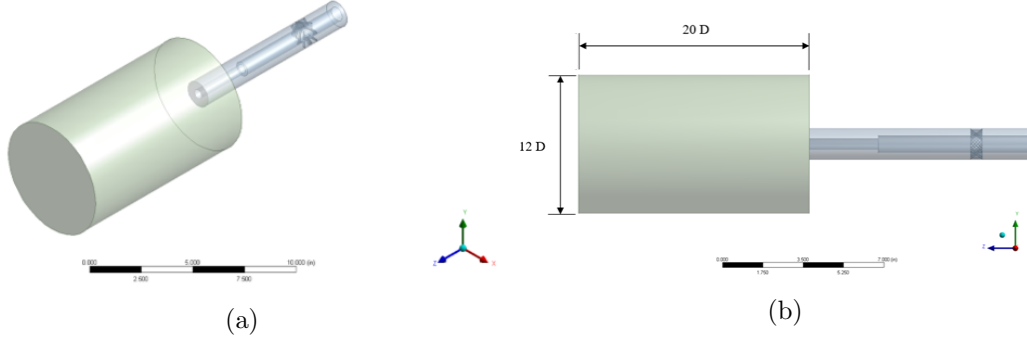


Figure 5.5: Computational domain Louisiana burner (a) isometric computational geometry (b) axial section computational geometry with combustion zone dimensions

Table 5.1: Louisiana burner parameters of the non reacting flow.

PARAMETERS	VALUES	UNITS
Density	1.225	kg/m <sup>3</sup>
Specific heat at constant pressure $c_p$	1006.43	J/(kgK)
Viscosity $\mu$	1.7894e-05	kg/(ms)
Temperature	298.15	K
Pressure	101325	Pa

used to simulate the combustion process, since there is neither a perfectly premixed nor a diffusive flame. Furthermore, the *Steady Diffusion Flamelet* approach is selected in order to consider all the reaction phenomena released from the chemical equilibrium hypothesis because of the flame stretching due to the interaction with the external turbulent velocity field. In addition to the default Fluent library for the thermodynamic properties, the *GRI-mech 2.11* [107] has been used as *Gas-Phase CHEMKIN Mechanism File* in order to generate the PDF-table. It consists of 49 chemical species and 277 reactions. The *Discrete Ordinates Model* (DO) has been chosen as radiation model. In this case, a

COUPLED solution scheme has been used because it is better than segregated algorithms in simulating compressibility effects. Spatial discretization operator are second order accurate (first order for turbulence equations). Time integration has been performed by means of first order implicit scheme. For the simulations, the time step size is halved with respect to the non-reacting flow.

### 5.1.2 Boundary conditions of non reacting flow

In the case of non-reacting flow, at the air inlet section, a velocity-inlet boundary condition has been considered, setting a velocity magnitude of 11.83 m/s, calculated starting from experimental bulk velocity equal to  $u_0 = 9.57$  m/s, a turbulence intensity of 5% and a hydraulic diameter  $D_h = 15.87$  mm (see Fig. 5.6). An outflow condition has been applied to the domain outlet (see Fig. 5.7a). This type of boundary condition is used when no information is known at the outlet. Moreover, the combustion chamber surface is treated with a slip wall type boundary condition, whereas all the other walls of the computational domain are characterized by a wall no-slip condition (see Fig. 5.7b).

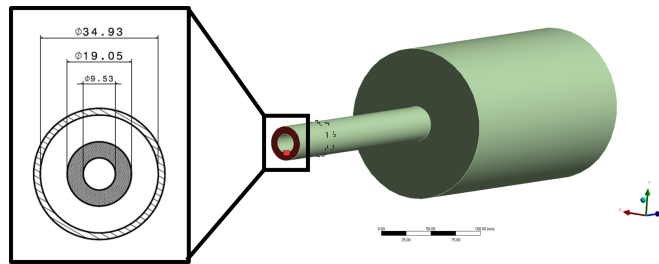


Figure 5.6: Boundary condition inlet section non reacting flow Louisiana burner

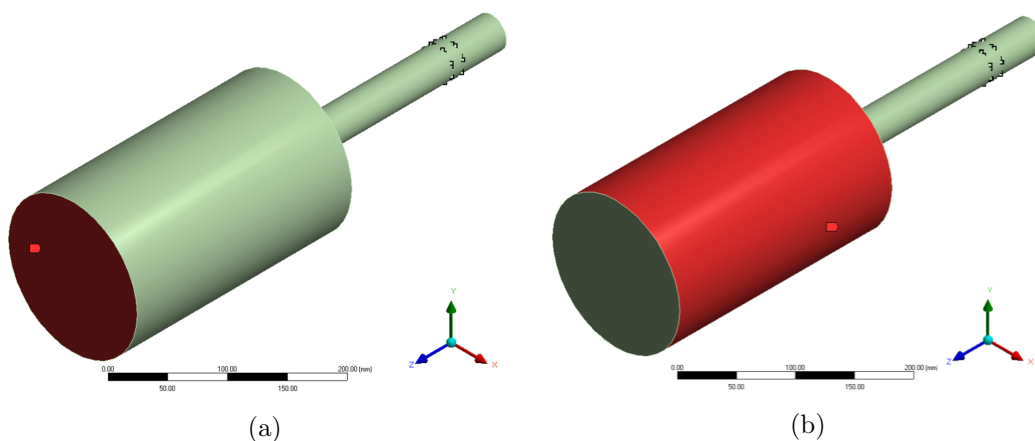


Figure 5.7: Boundary conditions used when simulating non reacting flow Louisiana burner (a) outlet section (b) combustion zone surface

### 5.1.3 Boundary conditions of reacting flow

In the case of reacting flow, the velocity-inlet boundary conditions for the fuel injectors have been introduced considering two cases: injection of pure methane (100%  $CH_4$ )

and injection of a mixture of methane enriched with 30%v of hydrogen (70%v  $CH_4$  + 30%v  $H_2$ ). Table 5.2 compares the main parameters for the fuel mixtures of the two aforementioned cases. The inlet radial,  $U_{rad,fuel}$ , and tangential,  $U_{tan,fuel}$ , velocity components of the fuel mixture have been calculated by assuming constant the inlet air mass flow rate,  $\dot{m}_{air} = 9.307$  g/s and the mean value of the equivalence ratio,  $\phi = 0.7$ , defined as the ratio between the stoichiometric,  $\alpha_{st}$ , and actual,  $\alpha$ , air-fuel ratio. In order to consider the effect of radiation, the walls internal emissivity has been set to 0.6, and zero heat flux hypothesis has been adopted to simulate an adiabatic system.

Table 5.2: Louisiana burner reacting flow parameters for pure methane and methane enriched with hydrogen case.

PARAMETERS	100%v $CH_4$	70%v $CH_4$ + 30%v $H_2$	UNITS
$\phi = \alpha_{st}/\alpha$	0.7	0.7	
$\alpha_{st}$ = stoichiometric fuel-air ratio	17.225	18.032	
$MW$ = molecular weight	16.0	11.8	kg/kmol
$\alpha$ = fuel-air ratio	24.65	25.76	
$\dot{m}_{air}$ = air flow rate	9.307	9.307	g/s
$\dot{m}_{fuel}$ = fuel flow rate	0.377	0.361	g/s
$\rho_{fuel}$ = fuel density	0.6551	0.4796	kg/m <sup>3</sup>
$U_{rad,fuel}$ = fuel radial velocity	150.9	197.3	m/s
$U_{tan,fuel}$ = fuel tangential velocity	30.6	40.0	m/s
$LHV$ = lower heating value	50.0	53.6	MJ/kg

The fuel is assumed to be injected counter-rotating with respect to the main swirled air flow Fig. 5.8. In reacting flow the turbulence intensity and hydraulic diameter have been set equal to 5% and 0.7874 mm respectively.

### 5.1.4 Grid refinement

In order to identify a good compromise between low computational cost and acceptable number of elements, three different unstructured meshes with different levels of refinement have been generated via ANSYS Workbench. In each mesh the same refinement, reported in Table 5.3, for the domain containing the swirler has been used, based on the influence sphere (Fig. 5.9) with the center point identified by the intersection between burner longitudinal axis and the center line of the swirler, radius of 17.78 mm and element size of 0.75 mm. The difference between Mesh 2 and 3 is the inflation that develops 19 layer of structured mesh on the internal and external walls of the central body duct downstream of the swirler and on the dump plane surface, Fig. 5.10. The first cell height of the inflation is 0.01 [mm], this characteristic is chosen in order to set the value of  $y^+$  equal to unity in the duct downstream the swirler, a number of 19 layers and a growth rate equal to 1.25 that leads to have a structural cell dimension equivalent to unstructured cell dimension, neighboring to the inflation, equal to 1 mm in the Mesh 3. This value of unstructured cells leads to a smooth radius of curvature at the angles of geometric cross-sectional variations, Fig. 5.10b. Furthermore, in Mesh 3 the element size in the domains upstream the swirler and from the swirler to 60 mm downstream of the dump plane has been changed from 1.5 mm of Mesh 1 to 1 mm.

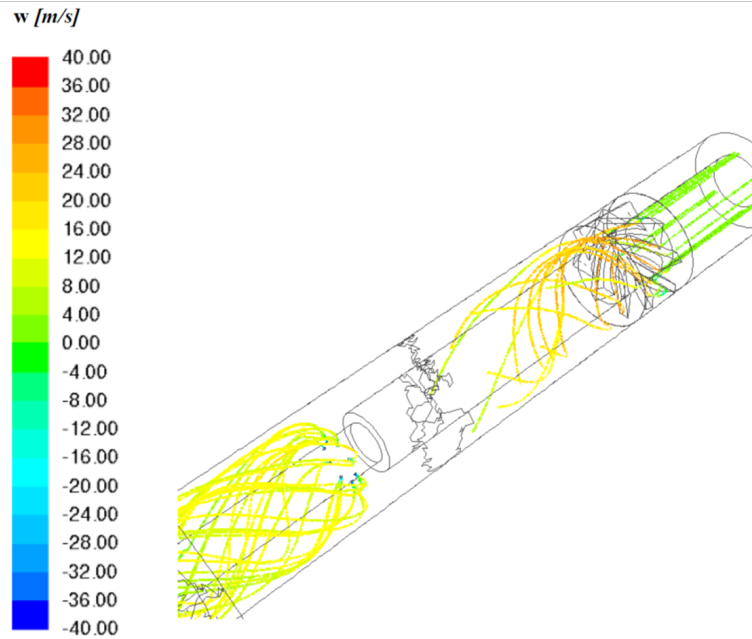


Figure 5.8: Pathlines tangential velocity in the duct of center body in the case of reacting flow.

Table 5.3: Louisiana burner mesh parameters.

MESH DATA	MESH 1	MESH 2	MESH 3	UNITS
Element size inlet - dump plane	2	1.5	1	mm
Element size sphere swirler	1	0.75	0.75	mm
Element size dump plane - 60 mm downstream of the dump plane	2	1.5	1	mm
Element size 60 mm downstream of the dump plane - outlet	4	4	4	mm
Inflation	✗	✗	✓	
First layer height	✗	✗	0.01	mm
Number of layer	✗	✗	19	
Growth Rate	✗	✗	1.25	
Number of elements	1.85M	3.7M	11.4M	

In order to allow an accurate fuel flow rate injection, for the reacting flow simulations, in each mesh the fuel injectors have been discretized with local face sizing of 0.15 mm, see Fig. 5.11. Fig. 5.12 shows the comparison between numerical and experimental mean axial velocity profiles normalized to the air bulk velocity,  $u = u_0$ . The profiles have been computed in the case of non-reacting flow at different axial locations downstream of the dump plane. Finally, Mesh 2, with number of elements of 3.7M, has been chosen as a good compromise between computational costs and results accuracy.



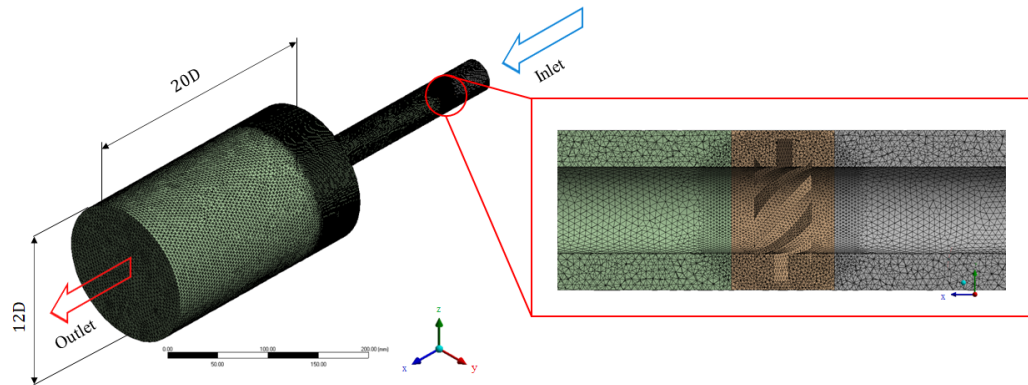


Figure 5.9: Refinement in swirler zone.

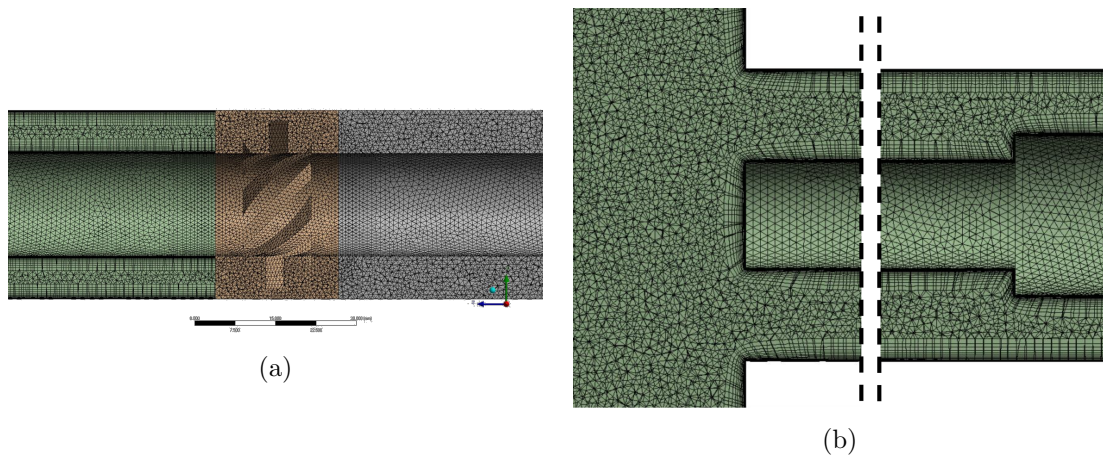


Figure 5.10: Inflation (a) in the duct of center body downstream the swirler (b) details of inflation on longitudinal variations of section

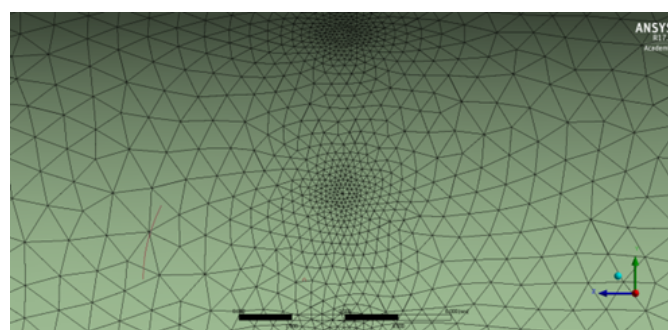


Figure 5.11: Face size injectors.

### 5.1.5 Non reacting flow results

In order to compare the results of non-reactive flow simulations with the experimental results, in the combustion chamber, 21 points on three axial lines in the longitudinal plane at 20, 30 and 40 mm downstream of the dump plane have been considered (see Fig. 5.13). In these points the values of the axial  $u$  and the tangential  $w$  velocities, normalized to

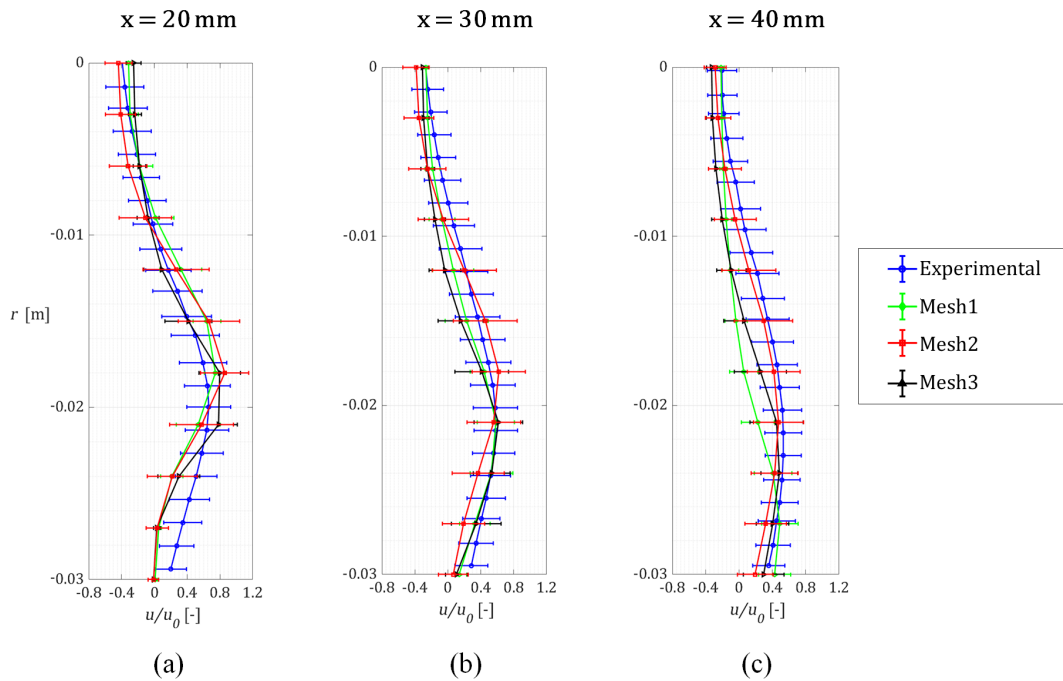


Figure 5.12: Comparison for different meshes between numerical and experimental normalized mean axial velocity profiles,  $u/u_0$ , for non-reacting flow, at different axial locations ( $x = 20$  mm (a),  $x = 30$  mm (b),  $x = 40$  mm (c))

the bulk velocity, have been calculated. Fig. 5.14 shows the comparison between the numerical and experimental radial distribution of the mean axial ( $u$ ) velocity profiles for the non reacting case. The averaging-time used for these quantities is  $\Delta T = 4$  s, approximately equal to 12 times the characteristic period of the flow ( $1/f = 1/3.2 = 0.3125$  s) equal to the period of the PVC [106]. The numerical and experimental simulations are in good agreement. The numerical profiles are completely contained inside the RMS bars of the experimental data retrieved from [106]. The comparison between numerical and experimental mean tangential velocities has been reported in Fig. 5.15. In general the agreement between numerical simulations and experimental data is good with the velocity peaks well predicted both in magnitude and location.

Fig. 5.16a shows the distribution of the mean axial velocity,  $u$ , in the burner longitudinal plane with the zero-axial velocity isolines to highlight the recirculation zones. In particular, three distinct recirculation zones can be observed: a separation *Wake Recirculation Zone* (WRZ) behind the center body, a *Corner Recirculation Zone* (CRZ) due to sudden expansion of combustor cross section downstream of the dump plane and a *Central Toroidal Recirculation Zone* (CTRZ), formed due to vortex breakdown. The structure of this vortex is pointed out by the vorticity magnitude contour in logarithmic scale in Fig. 5.16b where the highest vorticity levels are observed at the WRZ and the CTRZ. Fig. 5.17 represents the Power Spectral Density (PSD) for the axial velocity signals sampled at the monitoring points located both on the combustor longitudinal axis and on the traverses downstream of the dump plane. It can be observed that the characteristic frequency is equal to 3.2 Hz, as expected [106]. This one can be considered the fundamental frequency of PVC precessing motion along the axis for the non-reacting flow. To

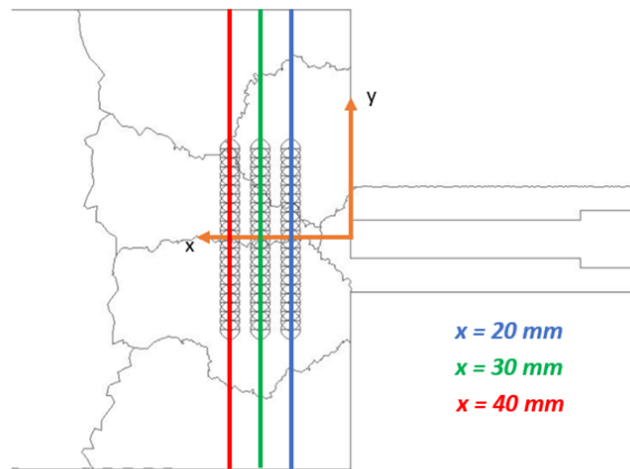


Figure 5.13: Monitoring points downstream dump plane.

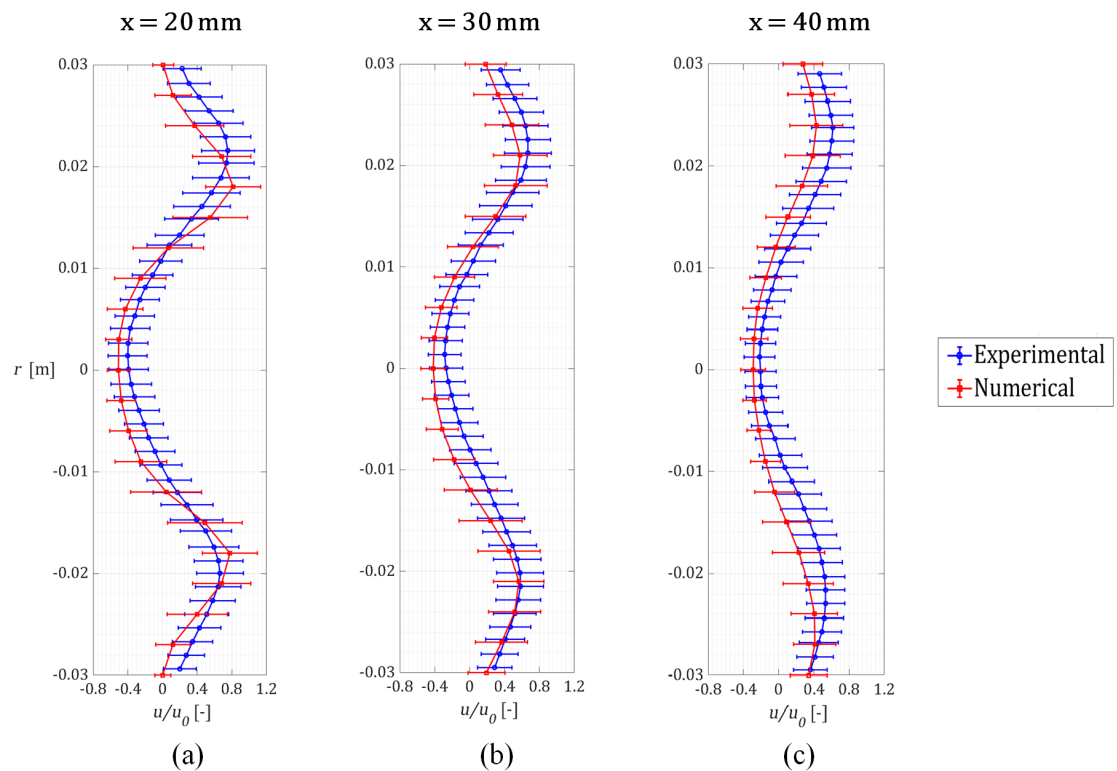


Figure 5.14: Comparison between numerical and experimental normalized mean axial velocity profiles,  $u/u_0$  for non-reacting flow, at different axial locations ( $x = 20$  mm (a),  $x = 30$  mm (b),  $x = 40$  mm (c)).

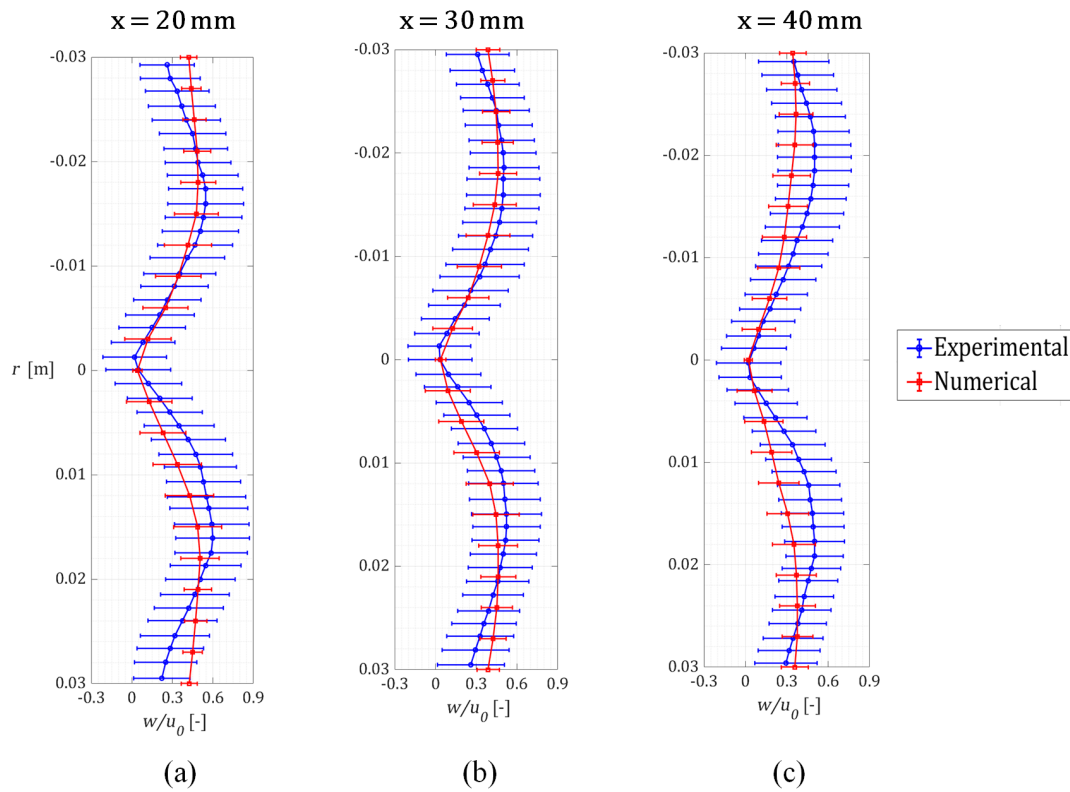


Figure 5.15: Comparison between numerical and experimental normalized mean tangential velocity profiles,  $u/u_0$  for non-reacting flow, at different axial locations ( $x = 20$  mm (a),  $x = 30$  mm (b),  $x = 40$  mm (c)).

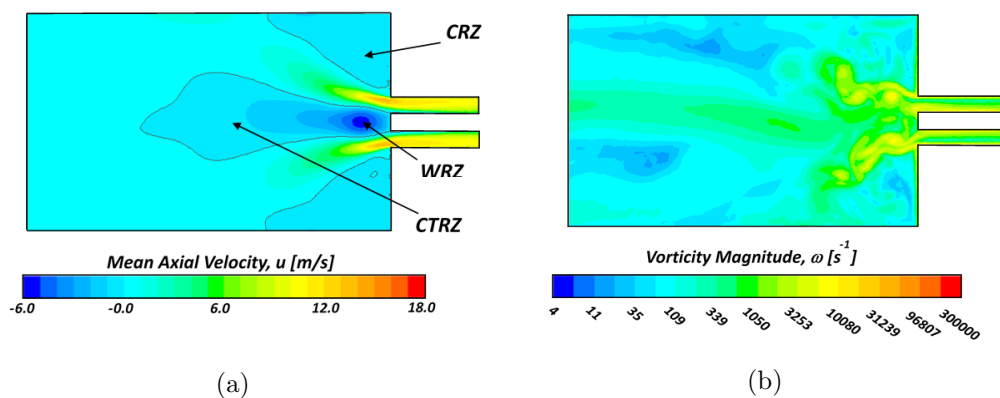


Figure 5.16: Contours on longitudinal plane of: (a) Mean axial velocity,  $u$ , with identification of Wake Recirculation Zone (WRZ), Corner Recirculation Zone (CRZ) and Toroidal Recirculation Zone (CTRZ) and the zero-axial velocity isolines in the longitudinal plane of the burner; (b) Vorticity magnitude.

underline the PVC vortex structure an iso-vorticity magnitude surface for  $\omega = 1000 \text{ s}^{-1}$  has been realized, as shown in Fig. 5.18.

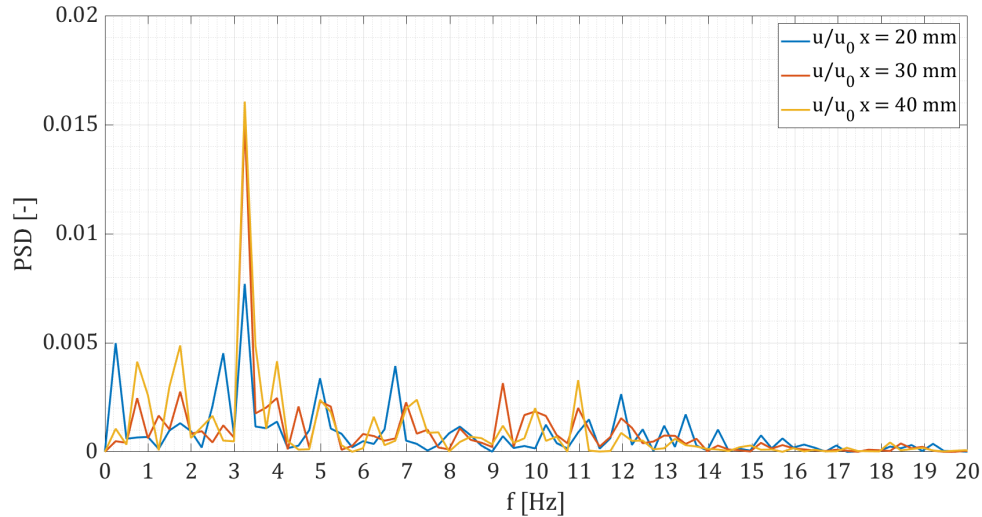


Figure 5.17: Power Spectral Density (PSD) for the axial velocity signals at different axial locations.

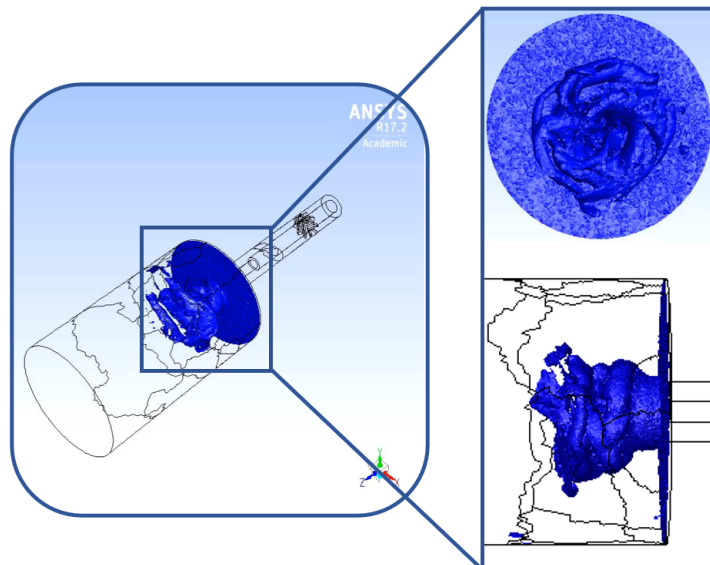


Figure 5.18: Iso-vorticity magnitude surface ( $\omega = 1000 \text{ s}^{-1}$ ).

### 5.1.6 Comparison between 100% $CH_4$ mixture vs 70% $CH_4$ - 30% $H_2$ blends

Starting from cold simulations, by activating combustion equations, reacting simulations have been carried out. In order to evaluate the influence of radiation model on reacting simulations the Discrete Ordinates (DO) radiation model has been activated. In Table 5.4 the parameters of calculation models implemented for reacting case are summarized.

Table 5.4: Calculation parameters of reacting flow simulations.

<b>Combustion parameters</b>		
PARAMETERS	VALUES	UNITS
Type	URANS	
Time step size (dt)	0.005	s
Number of Time Step	400	
Flow time analyzed	3	s
Iteration/Time step	20	
<b>Combustion model: Partially Premixed Combustion</b>		
PARAMETERS	VALUES	UNITS
State Relation	Steady Diffusion Flamlet	
Energy Treatment	Non-Adiabatic	
Imported CHEMKIN Mechanism	GRI-mech 2.11 [108]	
Operating pressure	101'325	Pa
<b>PDF Parameters</b>		
PARAMETERS	100%v CH <sub>4</sub>	70%v CH <sub>4</sub> + 30%v H <sub>2</sub>
Number of Mean Mixture Fraction	51	46
Number of Mixture Fraction	18	18
Maximum Number of Species	20	20
Number of Mean Enthalpy Points	25	32
<b>Flamelet Parameters</b>		
PARAMETERS	VALUES	UNITS
Number of Grid Points in Flamelets	32	
Maximum Number of Flamelets	20	
Initial Scalar Dissipation	0.01	1/s
Scalar Dissipation Step	5	1/s
<b>Radiation Model: Discrete Ordinates (DO)</b>		
<b>Angular Discretization</b>		
PARAMETERS	VALUES	
$N_\varphi$	4	
$N_\theta$	4	
$N_{\varphi,p}$	3	
$N_{\theta,p}$	3	

First of all, the mixing processes between air and the two fuel mixtures (only  $CH_4$  and 70%v  $CH_4 + 30\%v H_2$ ) have been studied by focusing on the radial distribution of the equivalence ratio,  $\phi$ , entering the combustion chamber. Fig. 5.19 shows the mean contours of the equivalence ratio, averaged on a time interval of 3 s, at the burner cross section located at 1 mm upstream of the dump plane. It is noteworthy to note how  $\phi$  is not homogeneous ( $\phi = 0.7$ ). Moreover, its gradient in the radial direction in the case of methane-hydrogen mixture injection is higher than the case of pure methane injection: the fuel, indeed, tends to concentrate at the outermost radii.

Fig. 5.20 shows the mean radial distributions of equivalence ratio  $\phi$  in the case of burner fueled by 100%v  $CH_4$  (see Fig. 5.20a) and 70%v  $CH_4 + 30\%v H_2$  (see Fig. 5.20b). In

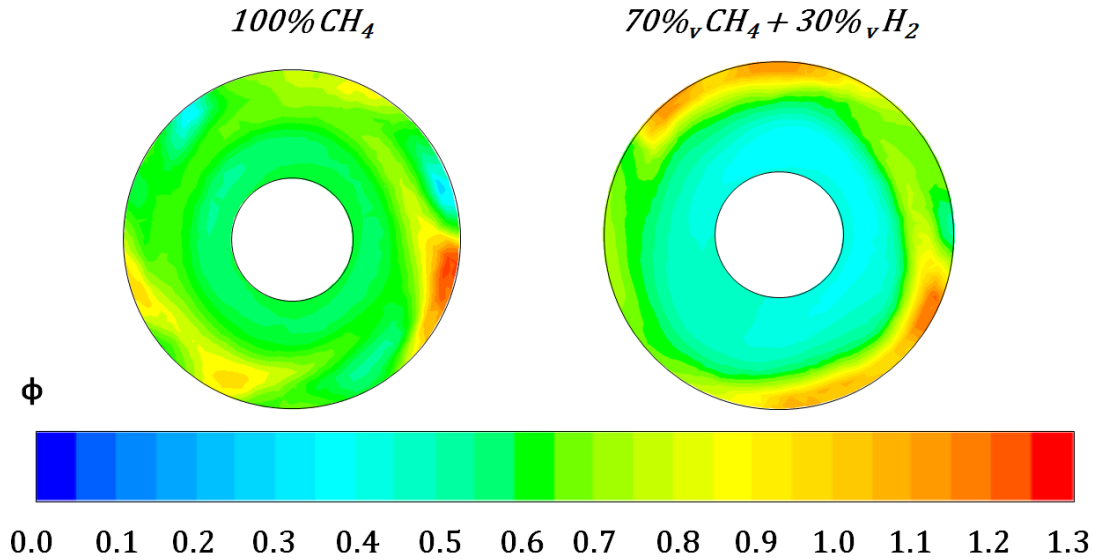


Figure 5.19: Comparison of the mean contours of the equivalence ratio,  $\phi$ , between pure methane (left) and methane-hydrogen mixture (right) combustion case (evaluated at the cross section located at 1 mm upstream of the dump plane).

the case of  $70\%v CH_4 + 30\%v H_2$  the mean value, until a radius equal to 12.35 mm, is in the range between 0.3 and 0.6. Instead, in the case of  $100\%v CH_4$ , the condition of  $\phi = 0.7$ , is already achieved for radii near to 12 mm. In the case of pure methane injection, major scattering is observed at radii greater than 12 mm respect with the case fueled by  $70\%v CH_4 + 30\%v H_2$ . This is a typical issue encountered in adapting combustors to hydrogen enriched fuels: because of the density reduction of fuel mixture due to the hydrogen blending, its momentum ( $\rho u_r^2$ ) increases in the injection, ensuring a greater penetration in the main air flow and letting the mixture leaner at inner radii.

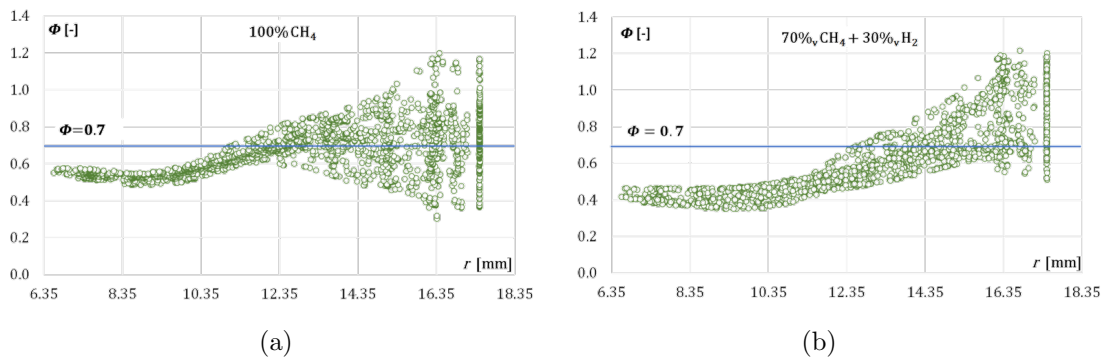


Figure 5.20: Mean radial distribution (sampling time= 3 s) of equivalence ratio  $\phi$  (cyan line is equal to  $\phi = 0.7$ ) in burner's cross section located at 1 mm upstream the dump plane: (a) burner fueled by  $100\%v CH_4$ , (b) burner fueled by  $70\%v CH_4 + 30\%v H_2$

After this comparison between mixing process of two mixtures, the mean profiles, normalized with respect to the bulk velocity  $u_0 = 11.826$  m/s, of axial and tangential velocities in the case of burner fueled by  $100\%v CH_4$  mixture, obtained by means of

URANS simulation on flow time equal to 2 s, have been compared with LES and experimental results of [106]. Fig. 5.21 and 5.22 show the mean radial profiles of  $u/u_0$  and  $w/u_0$ , at different axial locations ( $x = 20$  mm,  $x = 30$  mm,  $x = 40$  mm) downstream of the dump plane, with and without radiation model (DO). First of all, it is possible to highlight that the use of radiation model does not compromise the results of URANS simulations. At axial positions  $x = 20$  mm and  $x = 30$  mm (Fig. 5.21a and 5.21b) downstream the dump plane the URANS profiles for  $u/u_0$  are in good agreement with the LES results, in terms of both intensity and position of the peak, and both dimension and position of recirculation zone (where negative axial velocities occur). Instead, at axial position  $x = 40$  mm downstream the dump plane (Fig. 5.21c), the profiles of  $u/u_0$ , obtained by URANS simulations, are in good agreement with respect to the LES results only in terms of peak but not in terms of position, leading to a bigger recirculation zone. The mean profiles of tangential velocities  $w/u_0$  are very similar to the numerical (LES) results (Fig. 5.22) in each axial positions (see [102]).

Fig. 5.23 shows the comparison of axial velocity distribution,  $u$ , into the burner longitudinal plane between pure methane (left) and methane-hydrogen mixture (right) combustion case. The iso-velocity lines for  $u = 0$  m/s have been drawn to emphasize the recirculation zones. What is immediately marked is the similarity between the two velocity fields. This confirms the fact that up to 30% the velocity field does not change significantly. Moreover, if we compare this field with the one of the non-reacting case (see Fig. 5.16a), we can notice a variation of CTRZ in dimension and intensity. Indeed, it tends to stretch towards the outlet and to increase its radial dimension, leading the flow towards the lateral walls of the combustion chamber (see [102]). This behaviour has been found in other works on burners with a geometry similar to that investigated here (see for example [109]).

The contours of mean static temperature field, with and without DO, represented into the combustion chamber for the two reacting flows, evaluated on sampling time of 2 s, are compared in Fig. 5.24. A higher temperature can be noted, equally for case with and without DO, in the reaction zone for the case of methane-hydrogen mixture (2260 K for the mixture of methane enriched with 30%v of hydrogen versus 2150 K for the pure methane). This is due to two factors: firstly the introduction of hydrogen into the fuel mixture because of its slightly greater adiabatic flame temperature than methane; the second point is the higher local equivalence ratio of the mixture at the outer diameter of the mixing tube. However, in the case of burner fueled by 70%v  $CH_4 + 30\%v H_2$  mixture, simulated without DO (Fig. 5.24c), the temperature field is not uniform because a peak temperature can be observed in the corner of the combustion chamber. The activation of DO leads to smothering this effect due to the infrared light opacity of species such as  $CO_2$  and  $H_2O$ . Furthermore, in the case without DO (Fig. 5.24c), the flame length of burner fueled by 70%v  $CH_4 + 30\%v H_2$  mixture is shorter than the flame of pure methane mixture.

In Fig. 5.25 and Fig. 5.26 the radical  $OH$  and the  $CO_2$  mass fraction distributions are represented for both cases, with and without DO, respectively. The first ones allows to highlight the reaction zone into the combustion chamber because they are intermediate radicals of the combustion mechanism. The higher production of  $OH$  in methane-hydrogen mixture combustion points out the greater chemical reactivity of the hydrogen enriched mixture than pure methane. This distribution in the case of methane-hydrogen mixture without DO tends to be concentrated in the corners zone of combustion chamber. Regarding  $CO_2$  production, this is lower for the combustion of methane-hydrogen



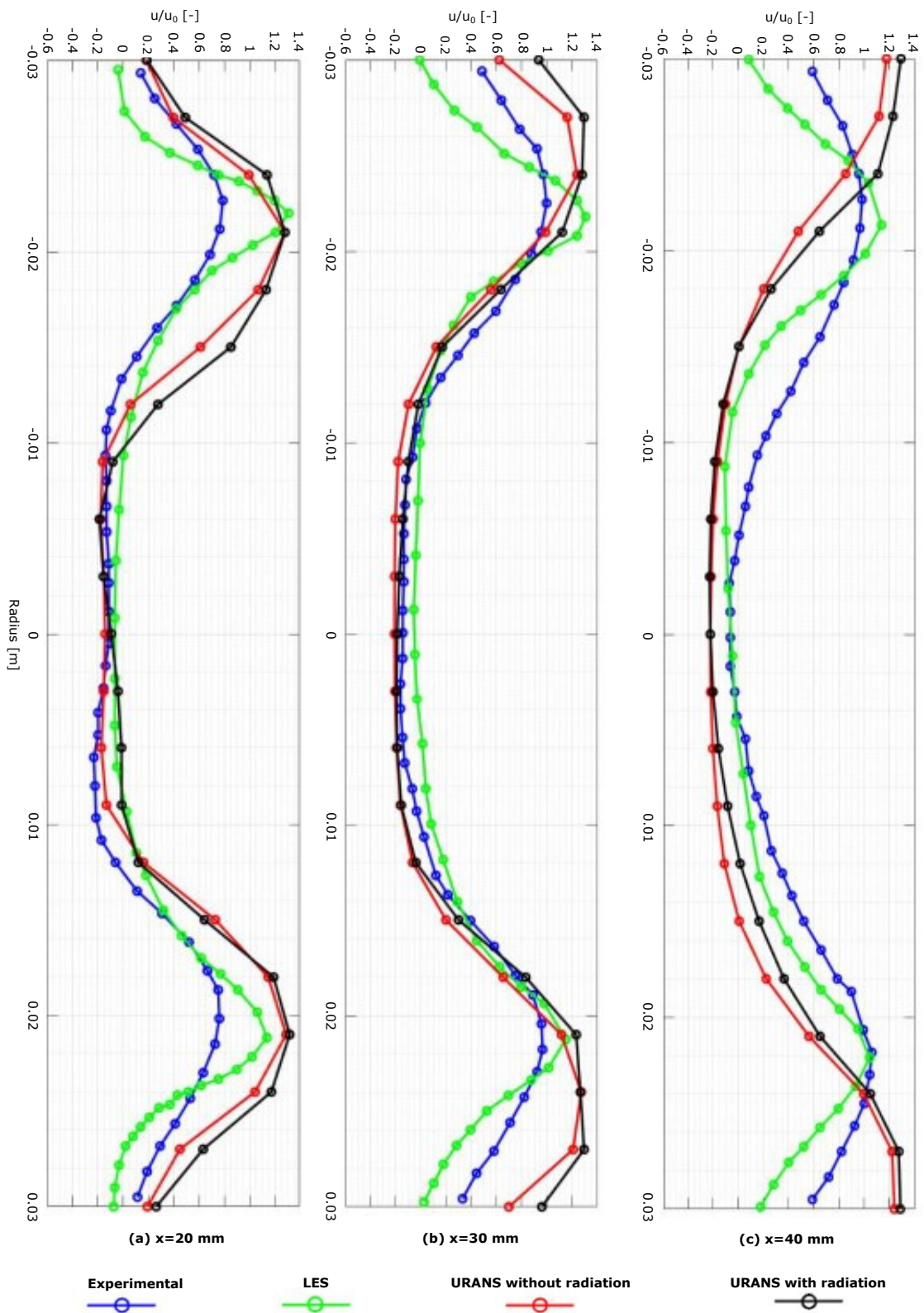


Figure 5.21: Burner fueled by 100%v  $CH_4$ -air mixture. Comparison of the mean profiles, normalized with respect to the bulk velocity  $u_0 = 11.826$  m/s, of axial velocities  $u/u_0$  (sampling time  $T = 2$  s), between URANS simulations with and without radiation model (DO) and LES and experimental results of [106] at different axial locations ( $x = 20$  mm (a),  $x = 30$  mm (b),  $x = 40$  mm (c))

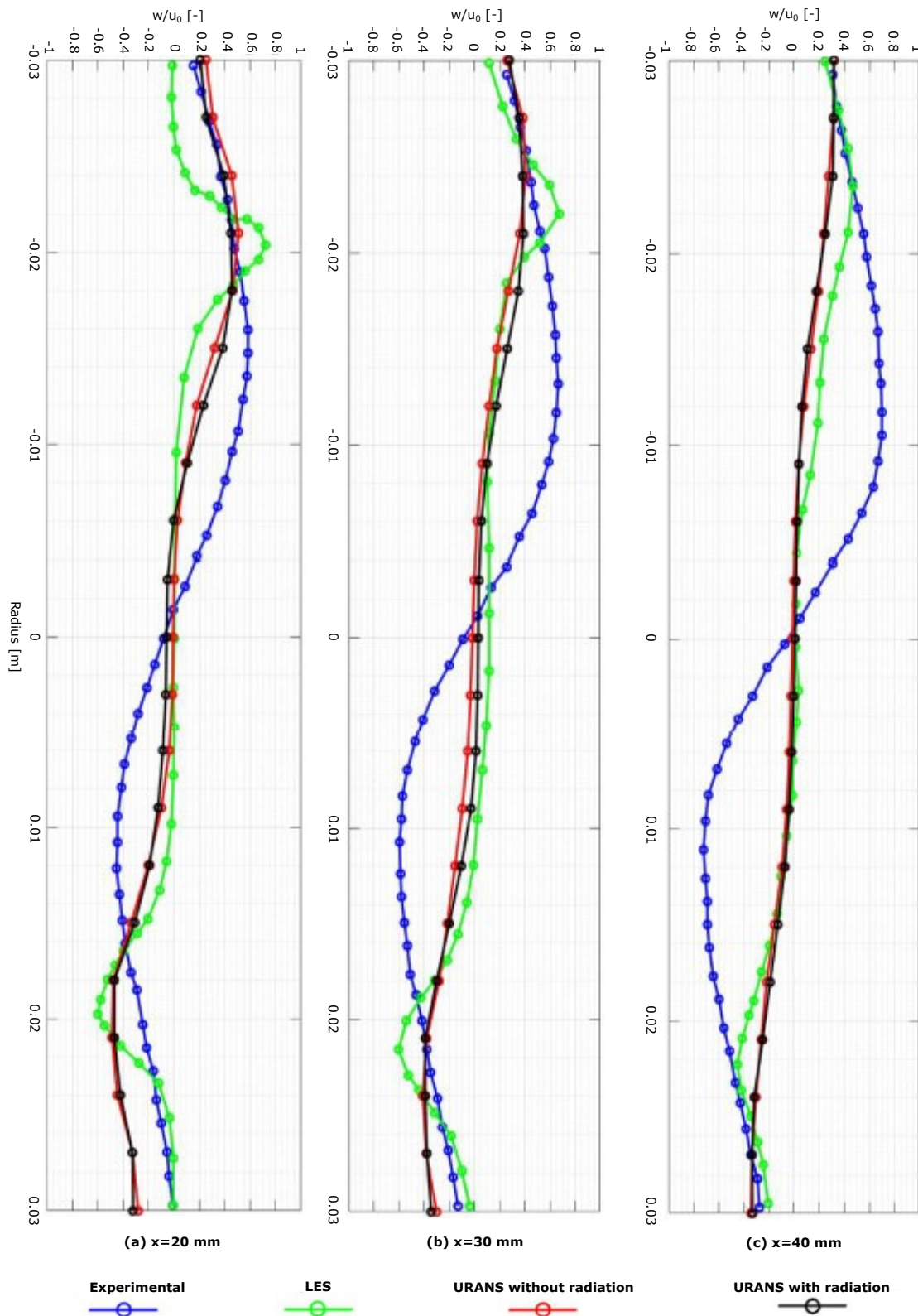


Figure 5.22: Burner fueled by 100%v  $CH_4$  mixture. Comparison of the mean profiles, normalized with respect to the bulk velocity  $u_0 = 11.826$  m/s, of tangential velocities  $w/u_0$  (sampling time  $T = 2$  s), between URANS simulations with and without radiation model (DO) and LES and experimental results of [106] at different axial locations ( $x = 20$  mm (a),  $x = 30$  mm (b),  $x = 40$  mm (c))

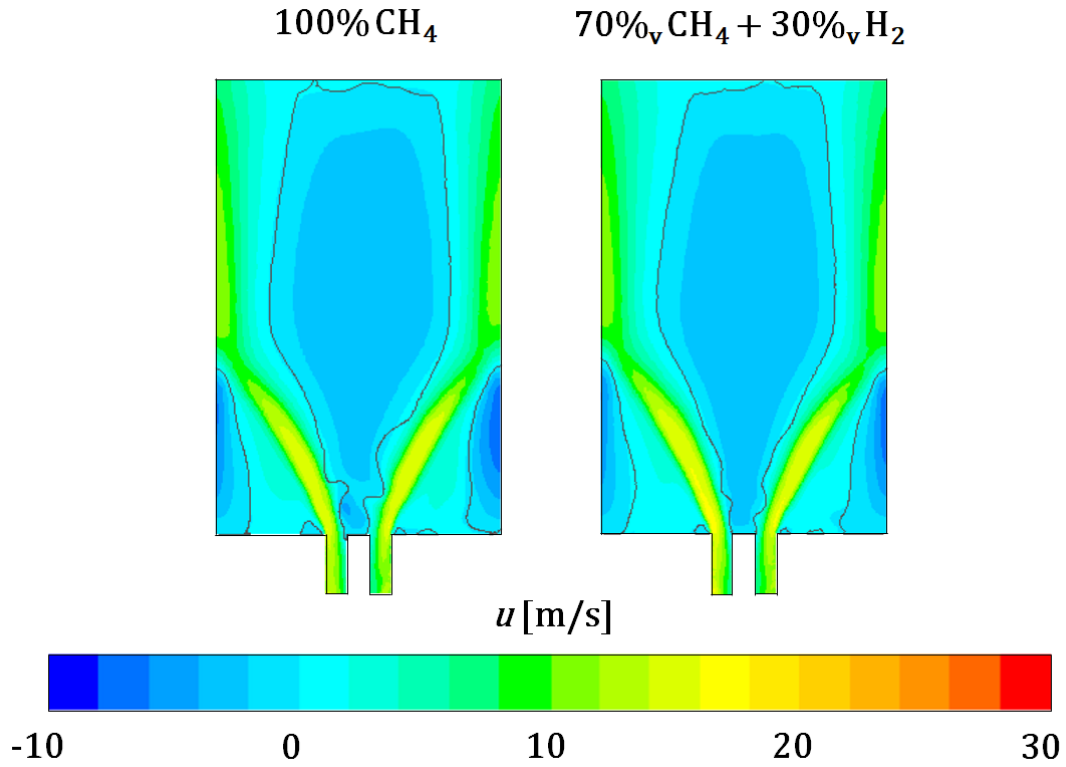


Figure 5.23: Comparison of axial velocity distribution,  $u$ , into the longitudinal plane of the burner between pure methane (left) and methane-hydrogen mixture (right) combustion case.

mixture due to the lower carbon content compared to pure methane. In Table 5.5 the  $CO_2$  emission levels are shown and it has been estimated a 10% reduction for the hydrogen enriched mixture. However, there is still a certain degree of asymmetry into the mean contours of the different quantities of the reacting flows, which could be caused by a short average time interval due to the high computational cost.

Table 5.5:  $CO_2$  emissions computed for both pure methane and methane-hydrogen mixture cases

	MEAN MASS FRACTION [ $kg_{CO_2}/kg_{mix}$ ]	MEAN MOLAR FRACTION [ $kmol_{CO_2}/kmol_{mix}$ ]	CONCENTRATION [ $g_{CO_2}/Nm^3_{mix}$ ]
100% $CH_4$	0.106	0.0675	132.6
70% $vCH_4 + 30\%vH_2$	0.0964	0.0607	119.2

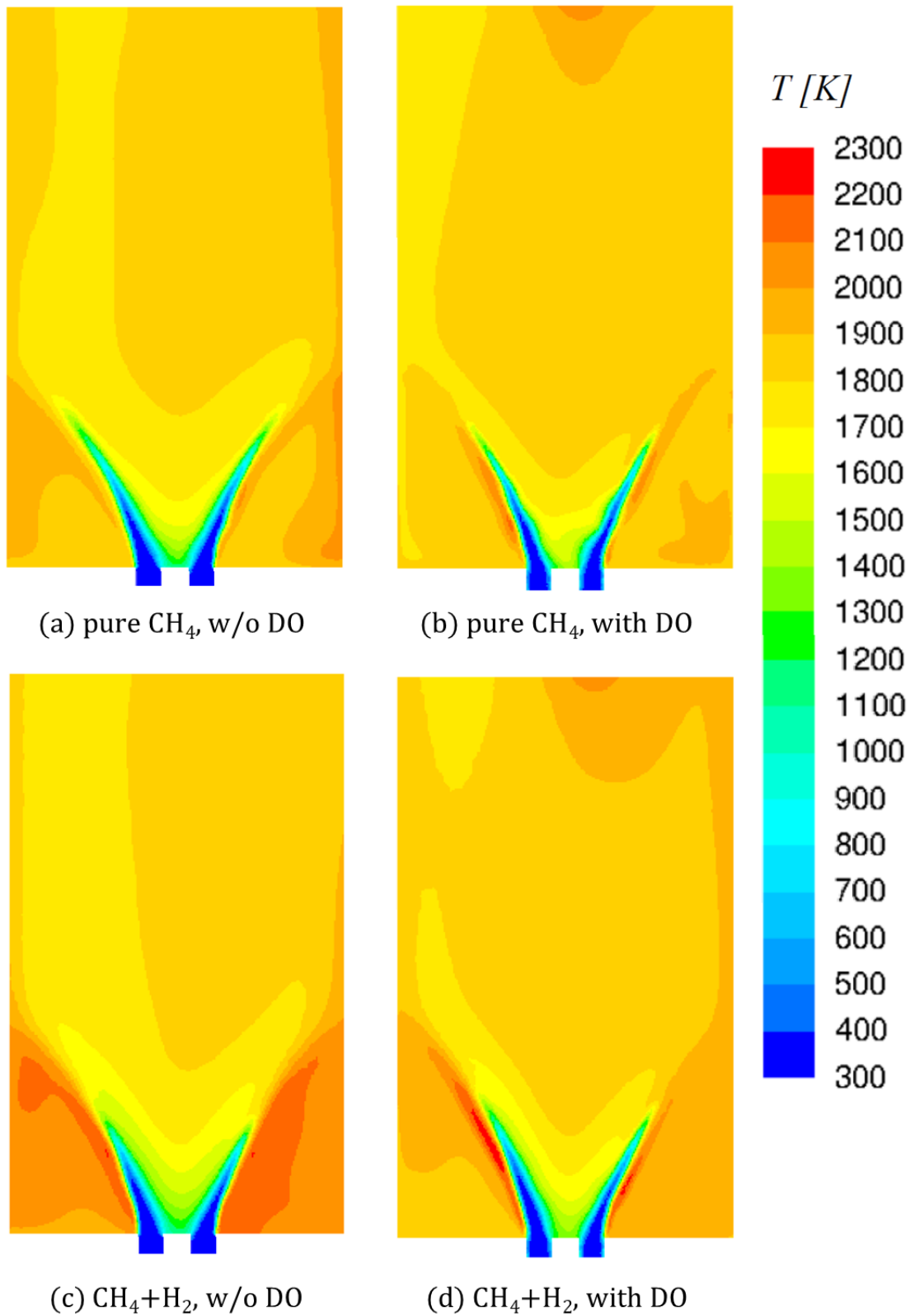


Figure 5.24: Comparison of mean static temperature field of combustion case into the longitudinal plane of the burner between pure methane ( $100\%v CH_4$ ) without (a) and with (b)  $DO$  and methane-hydrogen mixture ( $70\%v CH_4 + 30\%v H_2$ ) without (c) and with (d)  $DO$ .

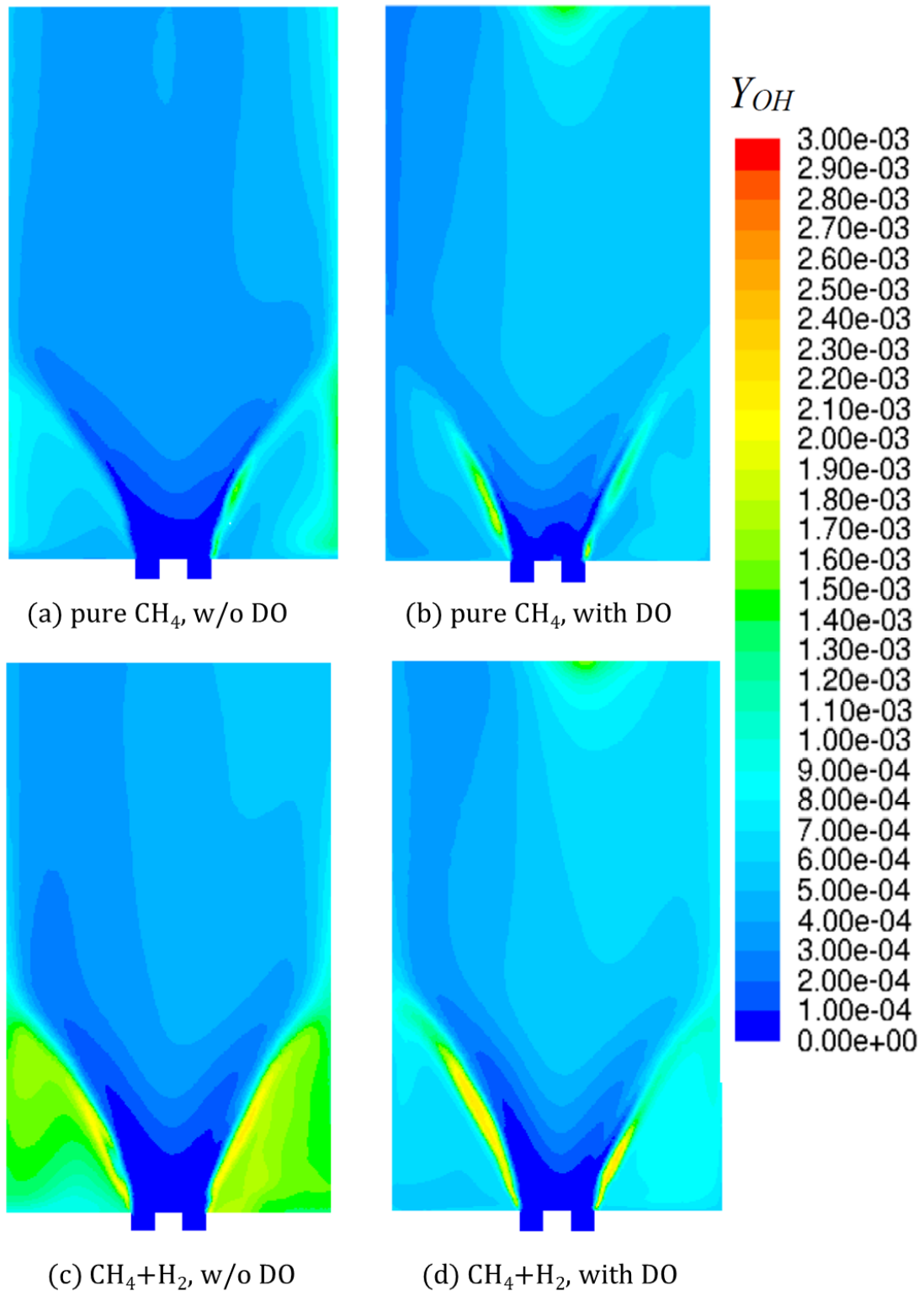


Figure 5.25: Comparison of  $OH$  mean mass fraction field of combustion case into the longitudinal plane of the burner between pure methane ( $100\%v CH_4$ ) without (a) and with (b) DO and methane-hydrogen mixture ( $70\%v CH_4 + 30\%v H_2$ ) without (c) and with (d) DO.

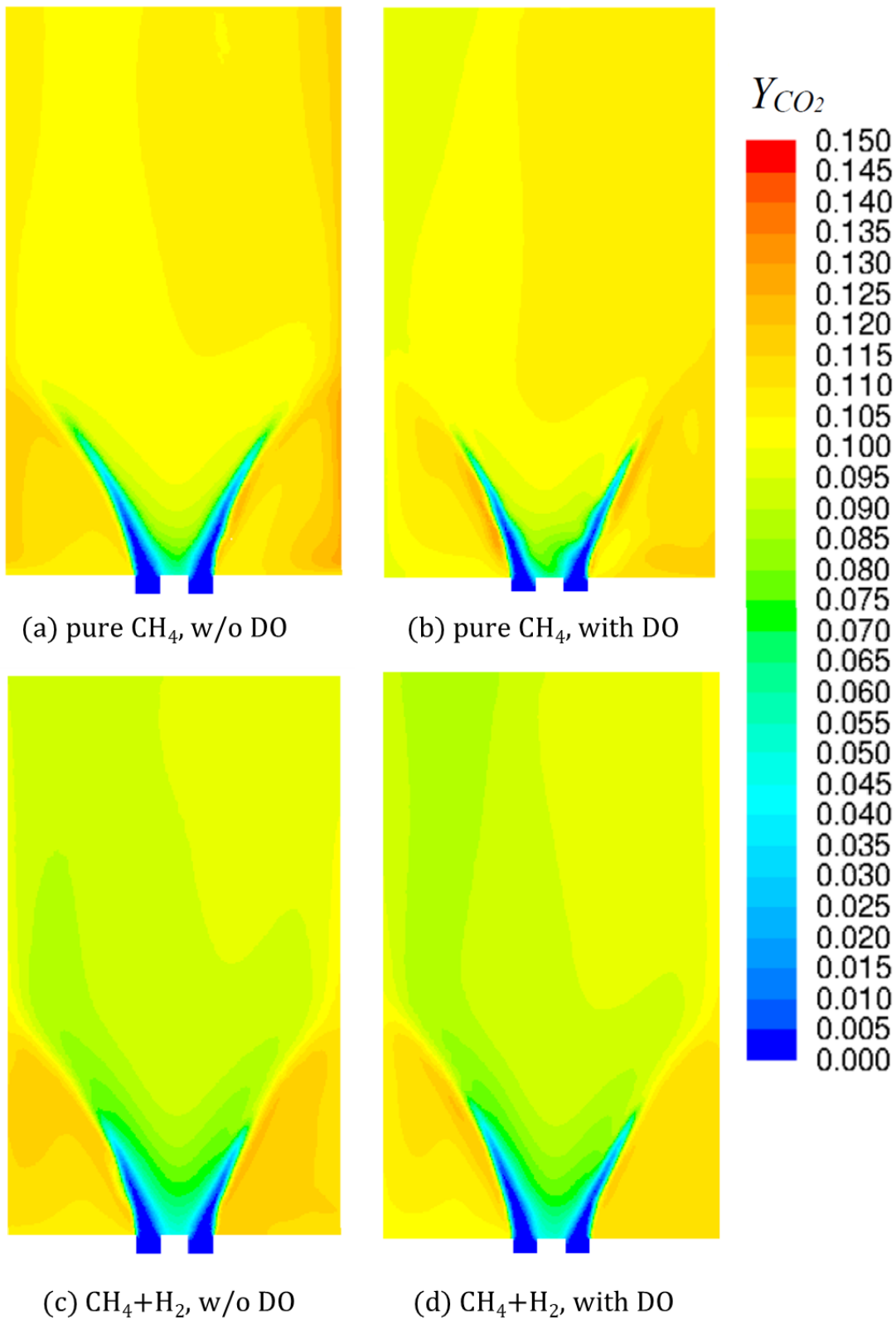


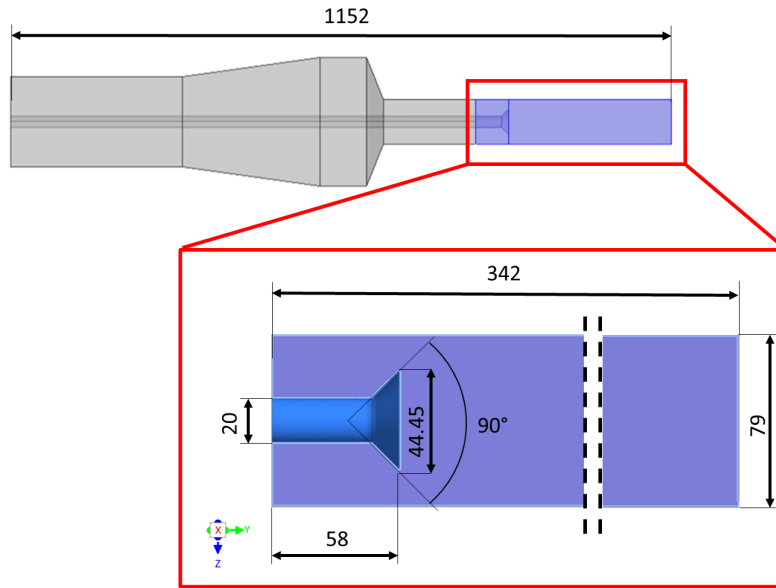
Figure 5.26: Comparison of  $CO_2$  mean mass fraction field of combustion case into the longitudinal plane of the burner between pure methane ( $100\%v CH_4$ ) without (a) and with (b)  $DO$  and methane-hydrogen mixture ( $70\%v CH_4 + 30\%v H_2$ ) without (c) and with (d)  $DO$ .

## 5.2 Premixed Vanderbilt Bluff body stabilized Laboratory Burner

The second lab-scale burner investigated by means of a fully steady 3D RANS approach [103] is a bluff body stabilized premixed burner studied at the Vanderbilt University. The choice of this burner is due to the presence of many numerical and experimental studies on it fueled by methane-air mixture. Indeed, Pan et al. [110] performed an experimental study that highlighted the influence of blockage ratio, turbulence intensity, value of vertex angle and equivalence ratio on recirculation zone after the bluff body. In addition, Nandula et al. [111] experimentally characterized this burner. Regarding numerical investigations, Cannon et al. [112] used "in situ tabulation method", with 5-step mechanism as chemical model in order to predict the behavior of the aforementioned burner. Andreini et al. [113] compared the LES and RANS simulations on this burner by using OpenFoam<sup>®</sup> and ANSYS Fluent<sup>®</sup> codes. Finally, Sudarma et al. [114] compared the  $k-\varepsilon$  and Reynolds Stress turbulence model in RANS simulations. Here this burner both in the case of CH<sub>4</sub>-air mixture and H<sub>2</sub>-air mixture, has been simulated. In the case of CH<sub>4</sub>-air mixture, the numerical setup has been validated with experimental results. Moreover, the influence of the turbulence models,  $k-\varepsilon$ ,  $k-\omega$ -SST and *Reynolds Stress*, have been analyzed. A study of the burner fueled with H<sub>2</sub>-air mixture has been carried out in order to compare the flame shape with ones of the case fueled by CH<sub>4</sub>-air mixture. Finally, a study of acoustic modes (frequencies and the growth rates) by using FEM approach (COMSOL Multiphysics<sup>®</sup>) is carried out in the case of two fuel mixtures in order to understand the influence of hydrogen on thermoacoustic behavior. In conclusions, the aim of this study is to understand the thermoacoustic effect of hydrogen in a burner designed to work with methane. [103]

### 5.2.1 Numerical setup

In Fig. 5.27, the geometry of the whole experimental setup is reported. Moreover, in the same figure a close up of the numerical domain is shown (marked with the red rectangle), in order to minimize the computational cost of the CFD simulations. As depicted in Fig. 5.27, the burner consists of a conical stainless steel bluff body with a base diameter  $D = 44.45$  mm and a vertex angle of 90°. The bluff body is co-axial with the burner. The combustion chamber shows a squared cross section (79 mm x 79 mm). In this study, the incompressible and adiabatic flow hypotheses were used considering  $T = 300$  K and  $p = 101325$  Pa as operating conditions. Three turbulence models, i.e.,  $k-\varepsilon$ ,  $k-\omega$ -SST and Reynolds Stress have been employed. A pressure-based solver with a SIMPLE pressure-velocity coupling scheme has been used. Spatial discretization operator are second order accurate (first order for turbulence equations). The *Partially premixed combustion model* was considered to simulate the combustion process together with the Zimont turbulent flame speed model to predict turbulent flame speed. The chemical kinetic mechanism GRIMECH-3.0 [108] has been adopted. The interaction between turbulence and chemistry is modeled with a probability density function (PDF). To model the flame front propagation, the transport equation of the progress variable ( $\theta$ ) is solved, which ranges from  $\theta = 0$  (unburnt mixture) to  $\theta = 1$  (burnt mixture). The CFD analysis was conducted by using ANSYS Fluent<sup>®</sup> v17.2 with a fully 3D RANS approach.



**Figure 5.27.** Representation of the numerical domain of the Vanderbilt University lab-scale burner

### 5.2.2 Boundary conditions

Table 5.6 shows the main parameters which characterize the  $\text{CH}_4$ -air mixture used for CFD simulations. In the same Table 5.6, the main parameters of the new mixture proposed for the hydrogen-air combustion are reported.

Table 5.6: Comparison of the main parameters characterizing the two mixtures employed in this work:  $\text{CH}_4$ -air and  $\text{H}_2$ -air

PARAMETERS	BENCHMARK $\text{CH}_4$ -AIR	NEW MIXTURE $\text{H}_2$ -AIR	UNITS
$\phi$	0.586	0.481	
$\alpha_{st}$	17.20	33.9	
$MW_{mix}$	28.11	24.31	kg/kmol
$\alpha$	29.30	70.6	
$\dot{m}_{air}$	70.78	70.78	g/s
$\dot{m}_{fuel}$	2.42	1	g/s
$\rho_{mix}$	1.14	0.99	kg/m <sup>3</sup>
$U_{ax,mix}$	10.81	12.26	m/s
$LHV$	50.0	119.9	MJ/kg
$T_{ad}$	1641	1577	K

In the case of reacting flow, for the air inlet section Fig. 5.28a, a velocity-inlet boundary condition has been chosen, setting an axial velocity of the fuel,  $u_{ax}$ , calculated starting from the inlet air mass flow rate,  $\dot{m}_{air} = 70.78$  g/s, indicated in [111, 114] and the thermal power of the burner,  $P_{burner} = 120$  kW. As result, the air-methane mixture is introduced through the inlet section with an average velocity of 10.81 m/s. A turbulence intensity of 24% has been used [111, 114]. The operating conditions of the fuel mixture



are  $T = 300$  K and atmospheric pressure. Furthermore, the chamber surface is treated with a no-slip wall type boundary condition (Fig. 5.28b). The outflow condition has been applied on the combustion chamber outlet surface (Fig. 5.28c).

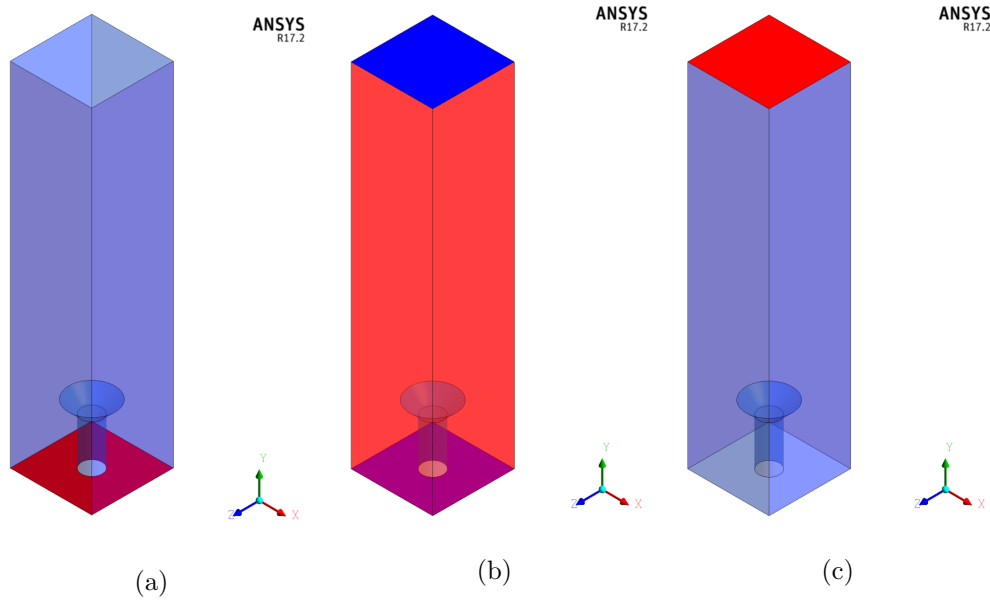


Figure 5.28: Boundary condition reacting flow Vanderbilt University burner: (a) inlet section, (b) combustion chamber surface, (c) outlet section.

### 5.2.3 Grid refinement

Three different unstructured meshes have been generated. As shown in Fig. 5.29, in which Mesh #3 has been reported, the domain has been divided into five zones in order to gradually increase the element size from the bluff body zone (zone 2) to the outlet zone (zone 5).

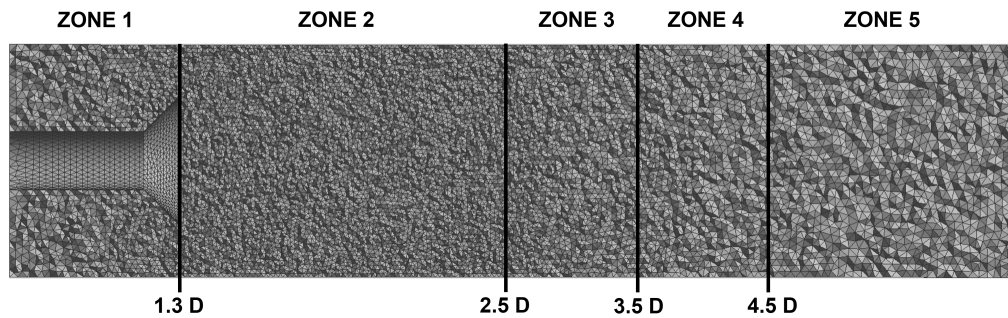


Figure 5.29. View of the Mesh #3 with the zones partition for the grid refinement

In Table 5.7, the zones extension along the axial distance,  $y$ , are expressed in function of bluff body diameter ( $D$ ). Mesh #1 and Mesh #2 are characterized by uniform grid size, i.e., 4.5 mm and 3 mm, respectively. On the other hand, Mesh #3 is characterized by element size of 3 mm in zones 1 and 5 with different levels of refinement in zone 2, 3,

and 4. The cell size has been chosen in order to activate the wall function.

Table 5.7: Summary of the grid refinement strategy applied for Vanderbilt University burner. For each zone, the cell dimension is reported ( $D$  is the bluff body diameter)

ZONE	STREAMWISE DIRECTION	MESH #1	MESH #2	MESH #3	UNITS
ZONE 1	0 - $1.3D$	4.5	3	3	mm
ZONE 2	$1.3D$ - $2.5D$	4.5	3	1.6	mm
ZONE 3	$2.5D$ - $3.5D$	4.5	3	2	mm
ZONE 4	$3.5D$ - $4.7D$	4.5	3	2.5	mm
ZONE 5	$4.5D$ - $7.7D$	4.5	3	3	mm
N. of elements		200 k	700 k	2.4 M	

Fig. 5.30 shows the comparison between the axial velocity profiles at different positions  $y/D$  for the three grid refinement. The results refer to a reacting case with methane-air mixture. All the cases have been computed by using the  $k-\omega$ -SST model for turbulent closure. Finally, the numerical results are in good agreement with the experiments. In conclusion, Mesh #2 with 700000 elements has been chosen in order to retain a good accuracy together with a reasonable computational cost.

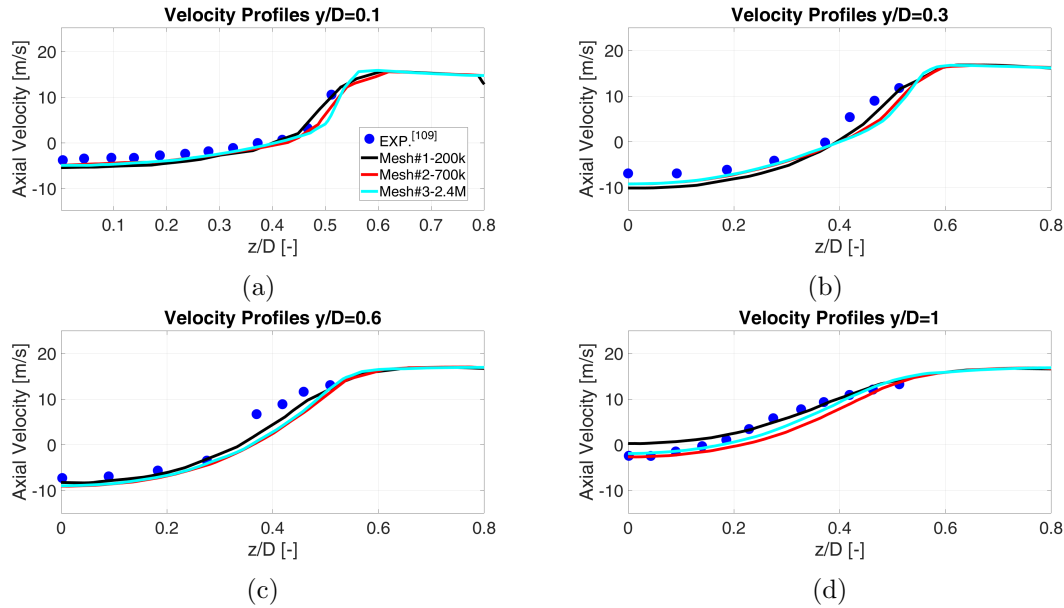


Figure 5.30: Mesh refinement: comparison between the exp. Nandula et al. [111] and the numerical results in terms of axial velocity profiles at different axial positions ((a)  $y/D = 0.1$ , (b)  $y/D = 0.3$ , (c)  $y/D = 0.6$ , (d)  $y/D = 1$ ) - reacting case

#### 5.2.4 Turbulence model assessment

The Reynolds Averaged Navier Stokes (RANS) equations are solved, thus the solution is related to the integral effects of the fluctuations, also called “turbulence effects”, on the mean flow. The closure of the momentum equations is based on the estimation of

the Reynolds stresses. Several models are widely used in CFD codes. Being the RANS simulations problem-based, the choice of the proper model should be made according to the flow characteristics. The results of three different turbulence models ( $k-\varepsilon$ ,  $k-\omega$ -SST and Reynolds Stress Model) are compared, on this burner, in order to select the best compromise between the reliability of the solution and the computational cost. The  $k-\varepsilon$  model is a two-equation turbulent model that is used for free shear layer away from surfaces [115], so it is expected to fail to capture the recirculation downward the bluff body. In order to extend the limitations of  $k-\varepsilon$  model for separated flow regions, the  $k-\omega$  SST model can be considered, where  $\omega$  stands for the specific turbulence dissipation rate. Moreover, the Reynolds Stress Turbulence Model solves the transport equations for all components of Reynolds stresses together with dissipation rate. This leads to solve a system of seven equations in 3D flows and for this reason, the computational cost of simulation becomes very high.

The RANS numerical setup of the burner fueled with  $\text{CH}_4$ -air mixture has been used to perform combustion analysis and to select the most suitable turbulence model that matches the experimental findings. Fig. 5.31 shows the comparison between measured (retrieved by [110, 111]) and numerical axial velocity profiles for different axial positions (i.e.,  $y/D = 0.1, 0.3, 0.6$  and  $1$ ).

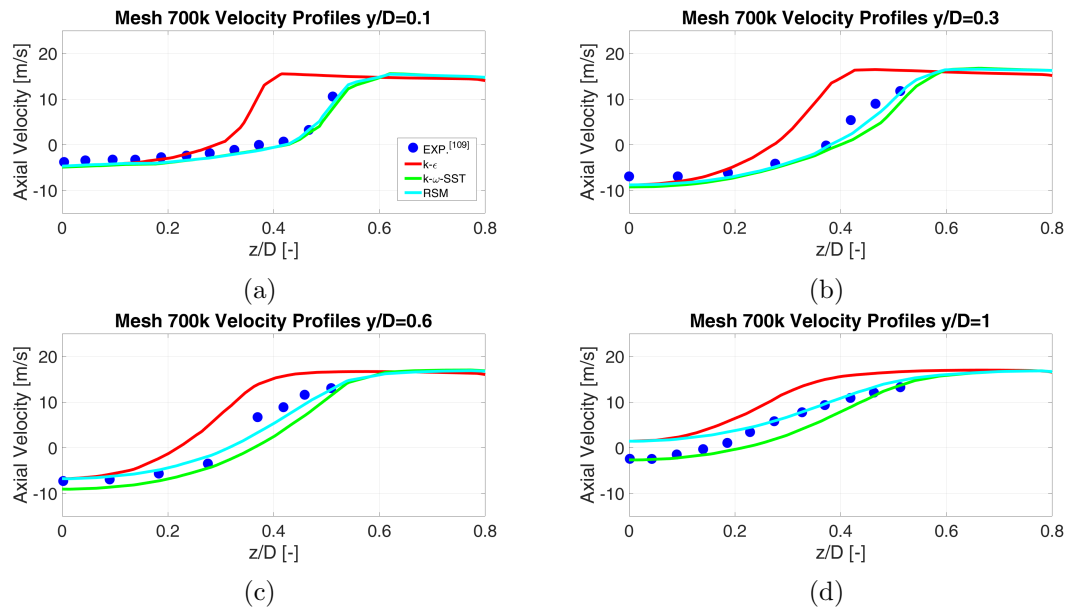


Figure 5.31: Study on turbulent closure: comparison between the exp. Nandula et al. [111] and the numerical results in terms of axial velocity profiles for different turbulence models ( $k-\varepsilon$ ,  $k-\omega$  SST, RSM) at different axial positions ((a)  $y/D = 0.1$ , (b)  $y/D = 0.3$ , (c)  $y/D = 0.6$ , (d)  $y/D = 1$ ) - reacting case

It is possible to note the presence of an internal recirculation zone, which is due to the installation of a bluff body. When the RSM and  $k-\omega$ -SST turbulence models are used, the axial velocity profiles at  $y/D = 0.1$  (cyan and green line, respectively) show a good agreement with the experimental data (see Fig. 5.31a). On the contrary, the  $k-\varepsilon$  model (red line) is not able to catch the right level of flow recirculation as pointed out by the axial velocity profiles compared along the radial direction ( $z/D$ ). Therefore,  $y/D = 0.3$  and  $y/D = 0.6$  (see Fig. 5.31b and 5.31c), highlight the unphysical behavior

of the numerical solution due to the  $k-\varepsilon$  model. Otherwise, the  $k-\omega$ -SST and Reynolds Stress Model solutions show similar results. Finally, at  $y/D = 1.0$  the recirculation zone shrinks, thus the flow is less affected by the turbulence model and the different solutions get closer to the experimental profile (Fig. 5.31d). The three turbulence models listed above have also been compared in terms of temperature (see Fig. 5.32). The turbulence model with the best agreement with experimental results is the  $k-\omega$ -SST [103]. In conclusion, as showed in Fig. 5.31 and 5.32, the predicted velocity profiles obtained with the  $k-\omega$ -SST turbulence model and RSM better approximate the experimental results.

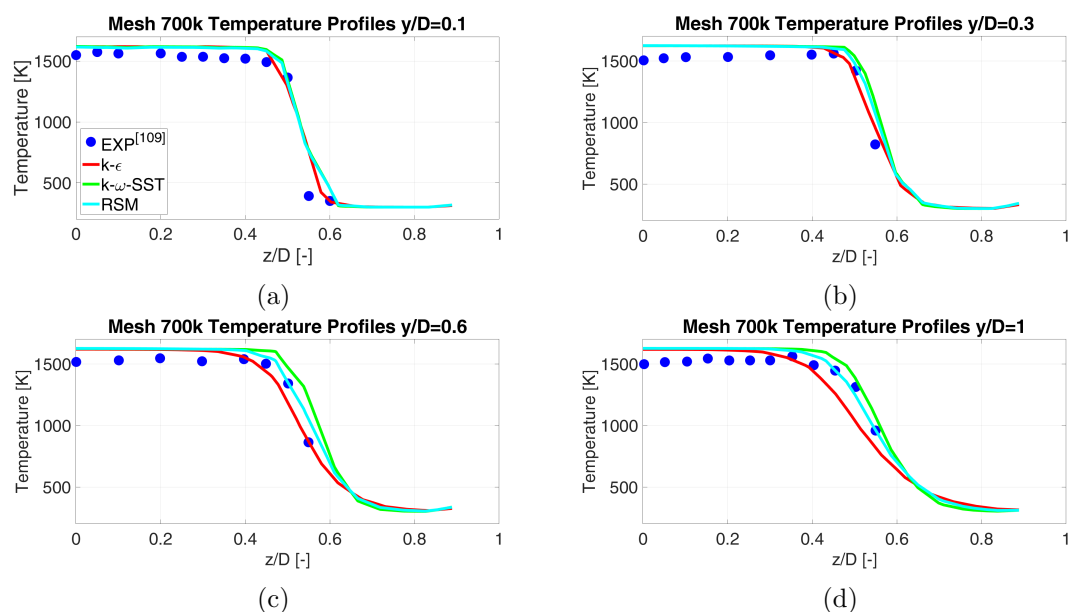


Figure 5.32: Study on turbulent closure: comparison between the exp. Nandula et al. [111] and the numerical results in terms of temperature profiles for different turbulence models ( $k-\varepsilon$ ,  $k-\omega$  SST, RSM) at different axial positions ((a)  $y/D = 0.1$ , (b)  $y/D = 0.3$ , (c)  $y/D = 0.6$ , (d)  $y/D = 1$ ) - reacting case

The computational cost of RANS simulations with Reynolds Stress Model (RSM) turbulence closure is higher than that with the  $k-\omega$ -SST. In fact, the RSM resolves more equations with respect to the  $k-\omega$  SST model because this last model is based on the resolution of only two equations regarding the turbulence kinetic energy ( $k$ ) and the specific turbulence dissipation rate  $\omega$ . Since these two models show similar agreement with the experimentally measured velocity, the  $k-\omega$  SST model has been chosen because it requires less computational effort. Finally, a comparison between RANS simulations of the burner fueled by methane-air mixture and the RANS simulations of the same burner developed by Andreini et al. in [113] was conducted. Fig. 5.33 shows the comparison in terms of progress variable  $\theta$ . The model developed in this work is in good agreement with respect to the RANS simulation of Andreini et al. in [113].

### 5.2.5 Comparison between 100% $CH_4$ vs 100% $H_2$ mixture

The impact of the two fuel mixtures on the performance of the burner has been investigated. In particular, the 100% hydrogen case is compared to the standard methane.

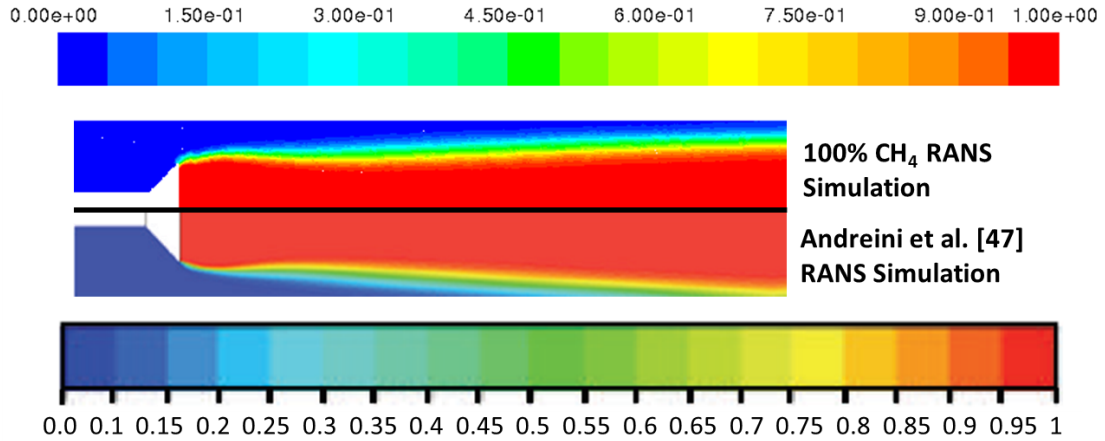


Figure 5.33: Comparison of progress variable  $\theta$  for burner fueled by methane-air mixture respect with the RANS simulation developed by Andreini et al. in [113]

CFD simulations have been carried out in order to perform thermoacoustic analysis via an approach based on the Helmholtz equations. As previously presented, Table 5.6 compares the main parameters of the two fuel mixtures compositions. The inlet axial velocity of the air-hydrogen mixture, has been calculated by assuming the inlet air mass flow rate,  $\dot{m}_{air} = 70.78$  g/s, and the thermal power of the burner,  $P_{burner} = 120$  kW as constants. As result, the air-hydrogen mixture is introduced through the inlet section with an average velocity of 12.26 m/s, which is higher than the one of methane case. Firstly, the comparison in terms of distribution of the heat release rate (HR) between the burner fueled by  $CH_4$ -air and  $H_2$ -air mixtures has been carried out. The heat release rate [ $J/(m^3s)$ ] is calculated by developing a custom field function that multiplies the point values of the reaction rate [ $mol/(m^3s)$ ] by the heating value [ $J/kg$ ] and molecular weight of the fuel [ $g/mol$ ]. The reaction rate is also calculated by a custom field function that multiplies the product formation rate [ $1/s$ ] by the fuel concentration [ $mol/m^3$ ], calculated by RANS simulation. The product formation rate (PFR) (see Eq. (4.21)), in ANSYS Fluent guide [116], is defined as the source term in the progress variable transport equation of premixed combustion model used in order to model the flame propagation front. Fig. 5.34 shows the contours of heat release rate for two mixtures. In detail, the  $H_2$ -air mixture shows a change in flame topology due to the greater reactivity of hydrogen compared to methane. This is a typical problem encountered when adapting burners designed to work with methane to the new  $H_2$ -air mixture: due to the reduction in density of the fuel mixture, its axial speed increases, introducing a variation in the operating point of the burner. Furthermore, Fig.5.34 shows that the heat release rate of the  $H_2$ -air mixture flame is an order of magnitude greater than  $CH_4$ -air mixture. Fig. 5.35 highlights the reaction zone of the combustion chamber, by means the progress variable  $\theta$ , for the two mixtures. The shape of  $\theta$  underlines the greater chemical reactivity of hydrogen-air than methane-air.

Fig. 5.36 shows the comparison of axial velocity profiles between pure methane and pure hydrogen mixture combustion cases at several axial positions (i.e.,  $y/D = 0.1, 0.3, 0.6$  and 1). The two cases have been solved by applying the  $k-\omega$  SST turbulence model. At  $y/D = 0.1$  (Fig. 5.36a), the axial velocity profile for the two cases is different. Specifically, at the smallest radii until  $z/D = 0.25$  the velocity of the pure hydrogen case is smaller than

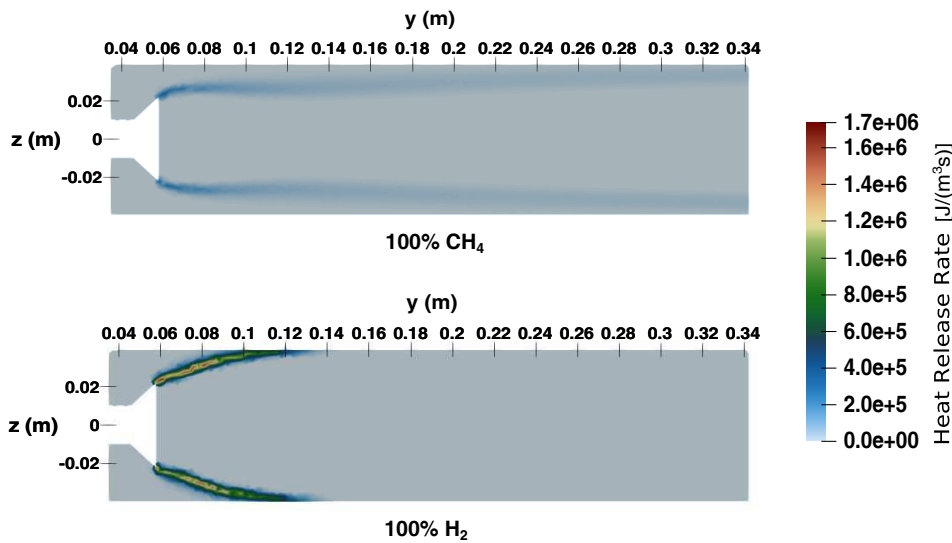


Figure 5.34: Contours of Heat Release Rate for the two different mixtures: methane-air and hydrogen-air

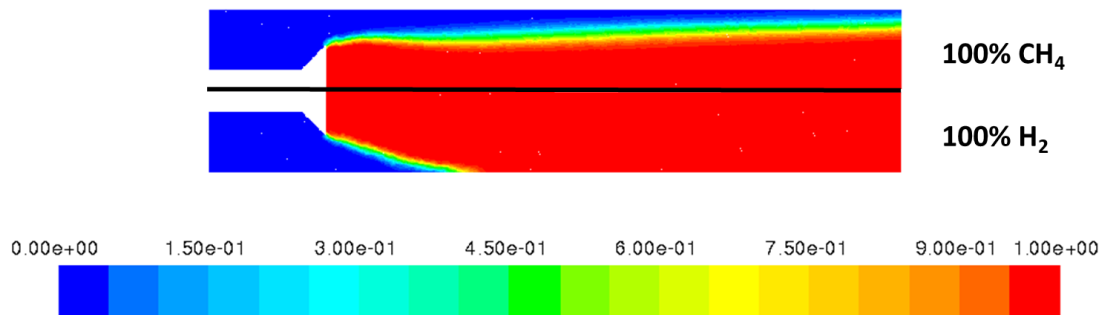


Figure 5.35: Contours of progress variable  $\theta$  for the two different mixtures: methane-air and hydrogen-air

the benchmark. At radii higher than  $z/D = 0.25$ , there is a reversal trend. From the second axial position  $y/D = 0.3$  (Fig. 5.36b) the recirculation zone for the case of  $H_2$ -air mixture becomes smaller with respect to the case of  $CH_4$ -air mixture (the area interested by negative axial velocities reduces). At  $y/D = 0.6$  and  $y/D = 1$  (Fig. 5.36c, 5.36d) in the case of  $H_2$ -air the axial velocities are positive for all coordinates  $z/D$ . Indeed in this case, the recirculation zone is smaller than the one of  $CH_4$ -air mixture as it can be seen in Fig. 5.37. The axial velocity profiles variation between the two cases is due to the differences in input velocity and flame topology which considerably modify the temperature field downstream of the bluff body (see Fig. 5.38). The hydrogen flame is still anchored to the bluff body, but its different opening affects the shape of the recirculation zone. In particular, at the axial positions  $y/D = 0.1$  and  $y/D = 0.3$ , the temperature of the two mixtures is very similar (see Fig. 5.39a and 5.39b), whereas, the temperature of  $H_2$ -air mixture is higher than  $CH_4$ -air mixture at  $y/D = 0.6$  and  $y/D = 1$ , (see Fig. 5.39c and 5.39d). Fig. 5.40 shows the differences between the two mixtures in terms of density at four axial positions along the radial direction. In each section, the density of  $H_2$ -air mixture is less than the one of the  $CH_4$ -air mixture.

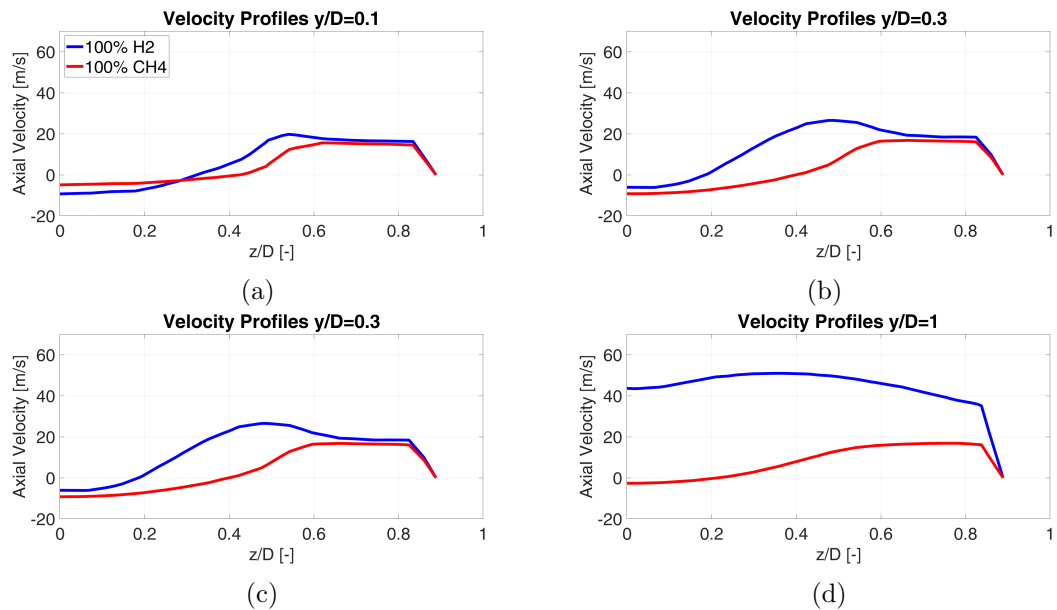


Figure 5.36: Comparison between axial velocity profiles for two different mixtures (red line 100%  $CH_4$ , blue line 100%  $H_2$ ) for reacting flow, at different axial positions ((a)  $y/D = 0.1$ , (b)  $y/D = 0.3$ , (c)  $y/D = 0.6$ , (d)  $y/D = 1$ )

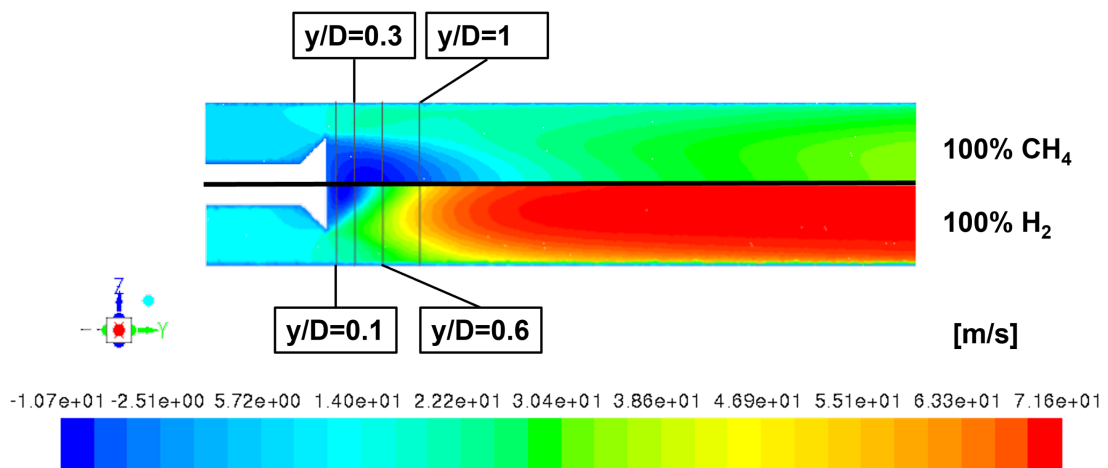


Figure 5.37: Comparison between axial velocity contours for two different mixtures. Transversal lines represent the cross sections where the axial velocity profiles have been compared in Fig. 5.36

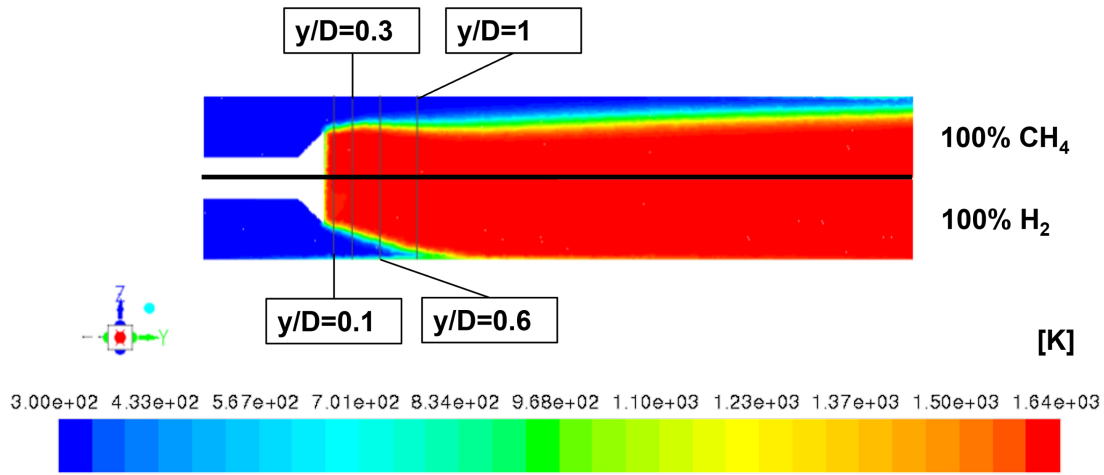


Figure 5.38: Comparison between temperature contours for two different mixtures. Transversal lines represent the cross sections where the temperature profiles have been compared in Fig. 5.36

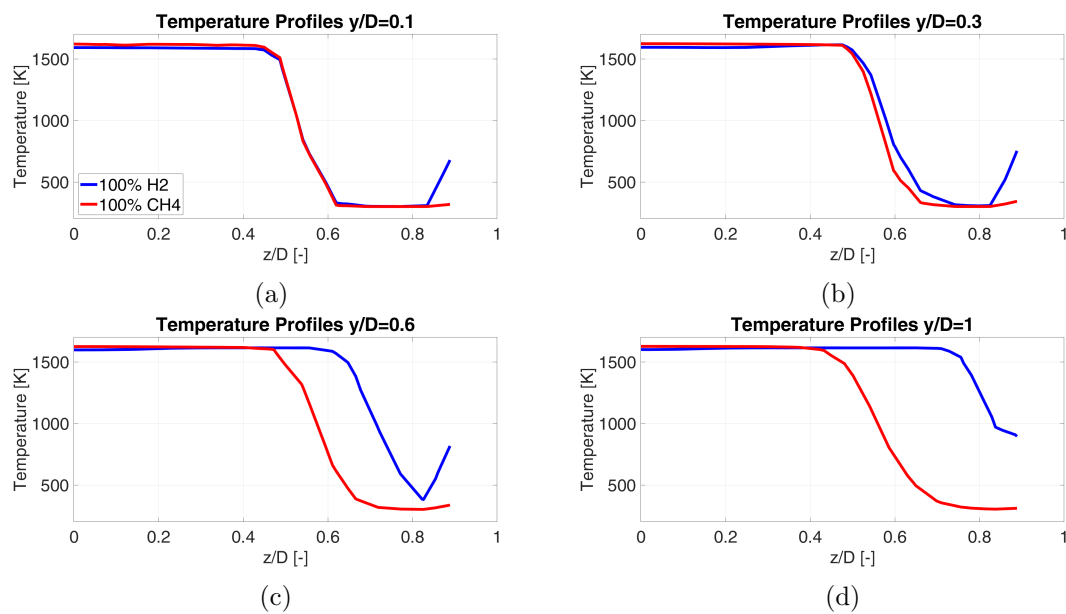


Figure 5.39: Comparison between temperature profiles for two different mixtures (red line 100%  $CH_4$ , blue line 100%  $H_2$ ), at different axial positions ( $y/D = 0.1$ ,  $y/D = 0.3$ ,  $y/D = 0.6$   $y/D = 1$ )



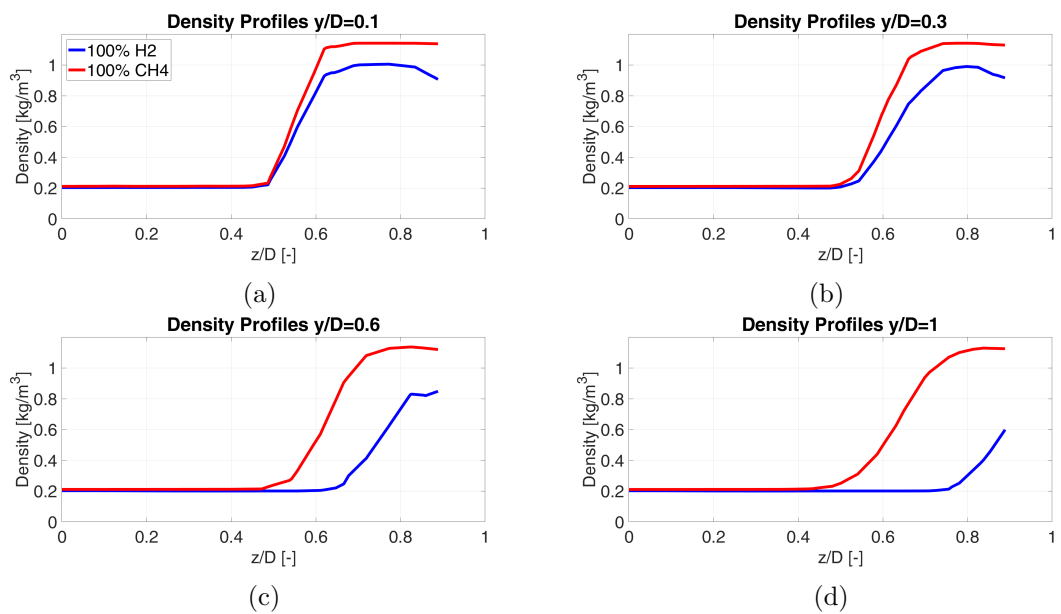


Figure 5.40: Comparison between density profiles for two different mixtures (red line 100%  $CH_4$ , blue line 100%  $H_2$ ), at different axial positions ((a)  $y/D = 0.1$ , (b)  $y/D = 0.3$ , (c)  $y/D = 0.6$ , (d)  $y/D = 1$ )

## Chapter 6

# Thermo-acoustic analysis

In perfectly premixed burners stabilized by bluff body, such as the one under investigation in this thesis, the driving mechanism that mostly leads to the build-up of thermoacoustic instability is Flame Vortex Interaction (see section 2.2). For this reason, in the definition of the most important parameters of FRF for this kind of burner, in first approximation, the chemical time lag can be neglected and only the convective time  $\tau$  is considered. In this chapter an extensive analysis on  $n$  and  $\tau$  used in the module *Acoustic Pressure and Frequency Domain* of COMSOL Multiphysics<sup>®</sup> is presented.

### 6.1 Boundary conditions and Grid refinement

Fig. 6.1 depicts the numerical domain, of Vanderbilt University test-rig, used in COMSOL with all the acoustic boundary conditions applied.

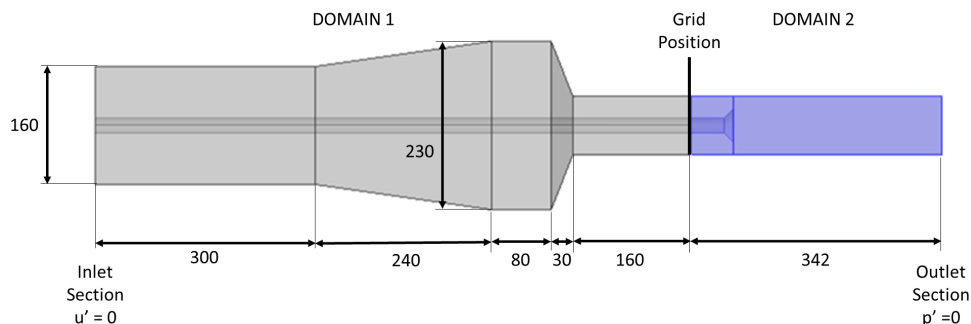


Figure 6.1: Numerical domain and relative boundary conditions used in COMSOL Multiphysics<sup>®</sup> (dimension in mm). The area in light blue represents the domain of Vanderbilt University burner object of the aforementioned CFD simulation (see section 5.2)

In the experimental test-rig described in [110], a turbulence grid was inserted at 58 mm upstream the bluff body. Upstream the turbulent grid there is a volume in which the mixture is injected. In order to acoustically simulate the entire test-rig in the COMSOL numerical model, this volume has been considered and the boundary condition of closed wall is imposed at the inlet section ( $u' = 0$ ). Moreover, the outlet section of the combustion chamber has been considered acoustically open ( $p' = 0$ ) according to the experimental setup [117]. Also for the COMSOL setup, a grid sensitivity analysis has

been carried out. The mesh has been divided in two domains, i.e., upstream (domain 1) and downstream (domain 2) of the turbulence grid. Table 6.1 compares three different meshes in terms of number of elements, element sizing, and computational time.

Table 6.1: Mesh refinement for FEM simulations in COMSOL of Vanderbilt University test-rig

DOMAIN	PARAMETERS	MESH A	MESH B	MESH C	UNITS
	Max elem. size	92	63.4	40.3	mm
Domain 1 (upstream grid)	Min elem. size	11.5	4.61	1.73	mm
	Growth rate	1.45	1.4	1.35	
	Max elem. size	40.3	23	23	mm
Domain 2 (downstream grid)	Min elem. size	1.73	0.24	0.24	mm
	Growth rate	1.35	1.3	1.3	
	N. of elements	31 k	123 k	255 k	
	Comp. time	64	332	623	s

Moreover, the comparison between the three meshes has been carried out also by computing the first four eigenmodes (see Fig. 6.2). Specifically, the Growth Rate (GR) in Fig. 6.2 corresponds to the imaginary part of each eigenmodes and allows the identification of stable ( $GR < 0$ ) and unstable modes ( $GR > 0$ ). The results of the grid sensitivity analysis point out the low sensitivity of the results to the grid size. The largest difference occurs for the 3rd frequency ( $f \sim 460$  Hz) in terms of GR. For the other points, the difference is negligible.

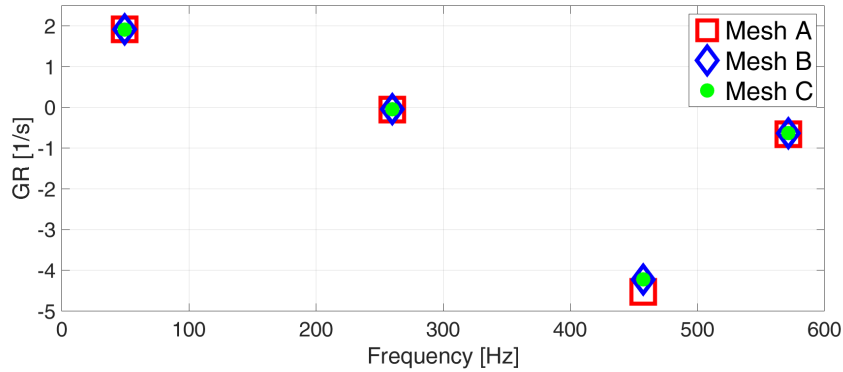


Figure 6.2: Comparison between eigenmodes obtained by using different mesh refinements in COMSOL

Figure 6.3 shows the comparison among the three meshes at the same frequency (the third one  $f \sim 460$  Hz) in terms of the Rayleigh index (defined in Section 2.1.1) plotted against the axial coordinate of the burner. Mesh A shows a different trend with respect to those of Mesh B and C (which present a good agreement).

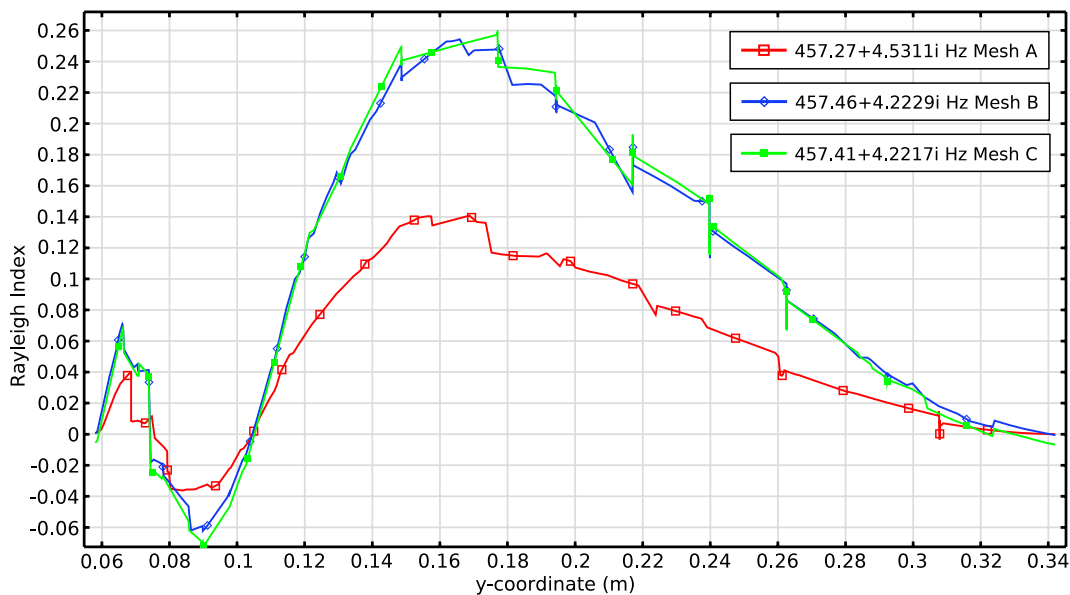


Figure 6.3: Comparison between Rayleigh Index obtained by using different mesh refinements in COMSOL

Hence, Mesh B has been chosen as it provides the best compromise between the reliability of the results and the computational cost. On this grid, the results of the CFD simulations have been transferred to perform accurate FEM analyses. As summarized in Table 6.1, this mesh has a number of elements close to 123000, a maximum element size of 63.4 mm in domain 1, and a maximum element size of 23 mm in domain 2.

## 6.2 Numerical setup of Helmholtz solver Simulations

Starting from Eq. (3.22), the comparison between the burner fueled by methane-air and hydrogen-air mixture has been developed by fixing the value of  $n$  equal to one. This assumption has been done to highlight only the influence of the compactness of the flame shape in the 100% hydrogen case. Naturally, the assumption of  $n = 1$  is very strong but it is necessary in order to develop sensitivity analyses on the different time delay between the two mixtures. Regarding the assumption of the value of  $n$ , a sensitivity analysis on the interaction index  $n$  has been carried out. In Table 6.2 the frequencies and Growth Rate (the imaginary part of complex frequency) have been reported for the first four modes in the case of the burner fueled by  $CH_4$ -air and  $H_2$ -air mixtures. Also in Fig. 6.4 and 6.5, this trend has been confirmed. In particular, the main difference between Growth Rate absolute values has been reached only for the first and third modes. In this case, a flame response function (FRF) (see section 3.2) has been used in order to carry out an acoustic characterization of the Vanderbilt University burner. COMSOL Multiphysics<sup>®</sup> (FEM code used for thermoacoustic simulations) solves the complete wave equation for each cell into which the 3-D acoustic domain is divided. Indicating with  $Q^{CM}$  the monopole source:

$$Q^{CM} = -\frac{(\gamma - 1)}{\rho \bar{c}^2} \lambda \hat{q} \quad (6.1)$$

then the Helmholtz equation (see Eq. (6.2)), solved in the COMSOL code, becomes:

$$\frac{\lambda^2}{\bar{c}^2 \bar{\rho}(\mathbf{x})} \hat{p}(\mathbf{x}) - \frac{\nabla^2 \hat{p}}{\bar{p}} = Q^{\text{CM}} \quad (6.2)$$

Table 6.2: Sensitivity analysis on interaction index  $n$  for Vanderbilt University burner fueled by  $CH_4$ -air and  $H_2$ -air mixtures

VANDERBILT UNIVERSITY BURNER FUELED BY $CH_4$ -AIR MIXTURE				
INTERACTION INDEX $n$				
MODE	0.5	1	1.5	UNITS
First	48.59+0.94i	49.44+1.99i	50.23+3.15i	Hz
Second	259.85+0.08i	259.96+0.17i	260.09+0.26i	Hz
Third	455.75+0.35i	457.74+0.70i	459.86+1.06i	Hz
Forth	571.77-0.017i	571.65-0.038i	571.51-0.07i	Hz
VANDERBILT UNIVERSITY BURNER FUELED BY $H_2$ -AIR MIXTURE				
INTERACTION INDEX $n$				
MODE	0.5	1	1.5	UNITS
First	57.07+1.76i	60.11+4.15i	63.07+7.59i	Hz
Second	281.55+0.45i	281.21+0.87i	280.85+1.26i	Hz
Third	540.43+1.46i	539.06+2.87i	537.69+4.25i	Hz
Forth	628.71+0.16i	628.48+0.30i	628.25+0.437i	Hz

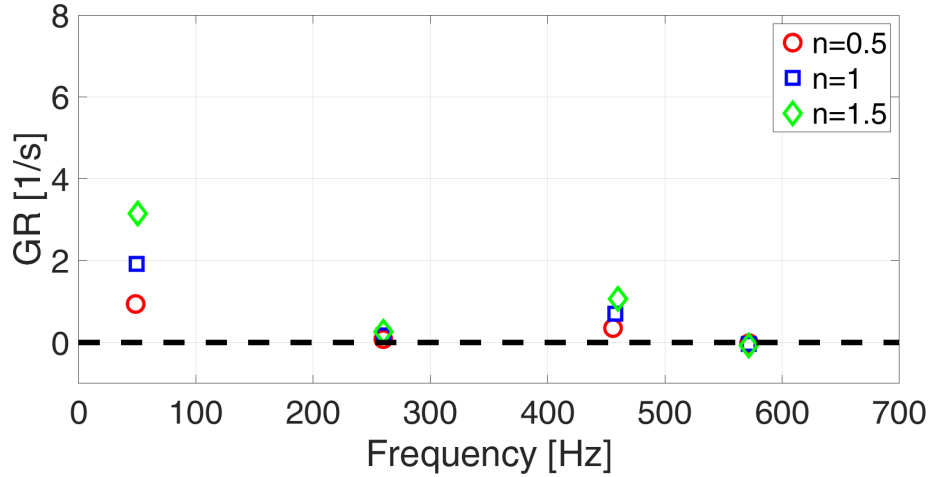


Figure 6.4: Sensivity analysis on interaction index  $n$  for benchmark  $CH_4$ -air mixture

In thermoacoustic analysis, in order to take into account the combustion process, it is necessary to transfer the results obtained from the numerical simulation CFD, carried out using ANSYS Fluent<sup>®</sup> (i.e., flame shape, reaction rate, density, temperature molecular weight and time delay), to the COMSOL Multiphysics<sup>®</sup> FEM code. This procedure requires the development of special MATLAB<sup>®</sup> code. Since the COMSOL mesh is coarse compared to the Fluent one, the code was developed with the purpose of interpolating 3D data from Fluent to COMSOL. The Matlab code works as follows:

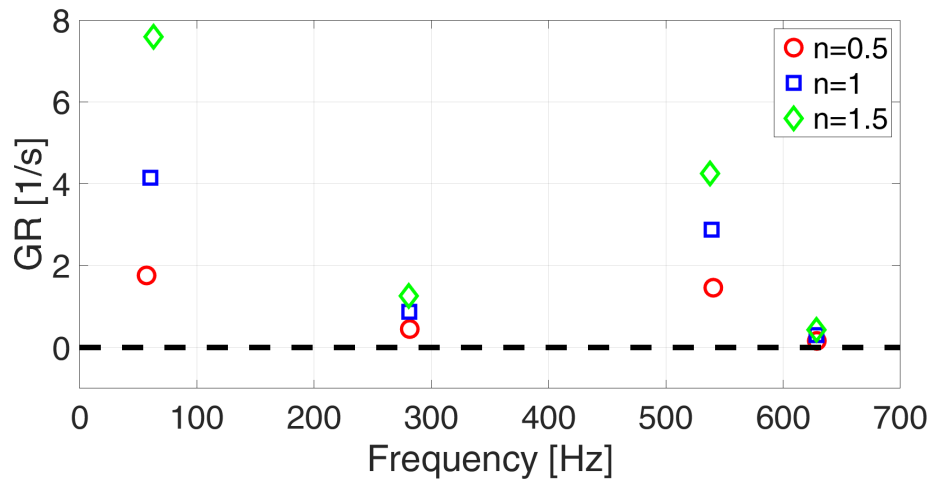


Figure 6.5: Sensivity analysis on interaction index  $n$  for  $H_2$ -air mixture

the nodes of the two meshes are read in terms of their 3D coordinates ( $x$ ,  $y$ ,  $z$ ). It is important to highlight that the coordinate system origins of both meshes are the same. Then, for each node of the COMSOL mesh, the code associates the thermodynamic property value of the Fluent mesh closest node. These fields were used in the monopole source defined in COMSOL. In the Fig. 6.6a and 6.6b, the comparison between the temperature and the reaction rate fields of both CFD solution (lower half section) and the data interpolated on the mesh employed on COMSOL (upper half section) has been reported for the burner fueled by  $CH_4$ -air mixture.

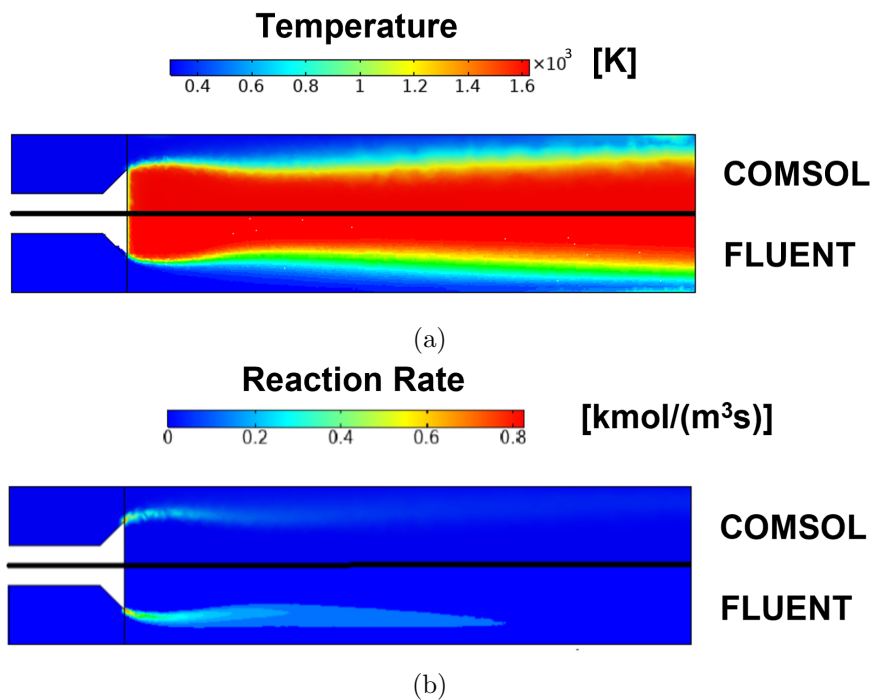


Figure 6.6: Comparison between the CFD solutions and the same fields interpolated on the COMSOL mesh. Vanderbilt University burner fueled by  $CH_4$ -air mixture

The definition of the FRF model requires further attention. Regarding the driving mechanism of the instability in premixed combustion, Fig. 6.7 shows the recirculation zone around the bluff body for the two combinations, CH<sub>4</sub>-air and H<sub>2</sub>-air, that generate the vortical structures that lead to the instability. The FRF is developed in several papers in the literature. For instance, Durox et al. in [118] studied the acoustic response of

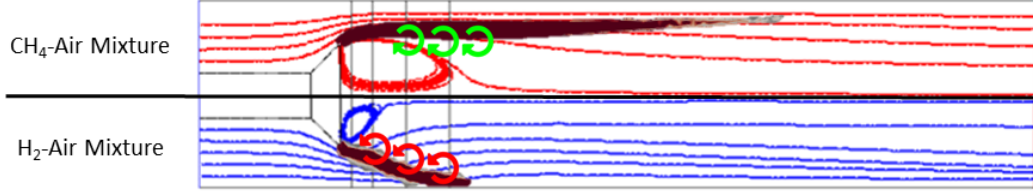


Figure 6.7: Schematic view of vortical structures downstream the bluff body for two different mixtures.

an inverted conical flame anchored on a central bluff body. An experimental campaign highlights that the phase difference between the heat release and velocity evolves almost linearly with frequency. In addition, Gatti et al. [119] investigated the frequency response of three different methane-air flames. The first of them is a flame stabilized with bluff body without swirl (as in our case). The FRF gain curve of this flame shows a typical low-pass filter behavior with a large gain at low frequencies. For high frequencies, the FRF phase increases with constant slope. As reported in [41] (in particular, in Section 3.4, Figure 10), in premixed combustion a mechanism contributing to heat release rate fluctuations is the interaction of velocity perturbations, starting at the flame base, with the flame front. This process is characterized, in first approximation, by a convective time delay  $\tau$  (chemical time scale is neglected). In this thesis, following [4, 88], an estimation of this time delay is computed using particle tracking techniques. Released at  $y/D = 0$ , particles are tracked and a convective time is computed until the flame front is reached ( $Y_{fuel} = 0$ ). This time value, known as "time delay", is assigned to the position of the flame front reached by the particle. This convective delay measurement approach appears physically sound and improving the one used by Alemela et al. in [120], according to which the average convective delay time for premixed flames is directly proportional to the ratio of the distance at which the highest reaction occurs to the effective transport velocity. With particle tracking, fluctuations of heat release due to velocity perturbations were more accurately tracked. Starting from Eq. (6.3), where  $H$  is the flame length and  $u_{bulk}$  is the bulk velocity, the constant time delay developed for CH<sub>4</sub>-air and H<sub>2</sub>-air mixtures are equal, respectively, to 0.0135 s and 0.0059 s.

$$\tau = H/u_{bulk} \quad (6.3)$$

The values of  $H$ , shown in Fig. 6.8, are equal to 0.188 m and 0.0919 m for pure methane and pure hydrogen cases, respectively. The flame length is calculated as the distance between the axial position  $y/D = 0$  and the "center of gravity" of the Heat Release Rate (HRR), as reported in [117] (see Eq. (6.4)). The values of  $u_{bulk}$  are equal to 13.67 m/s and 15.5 m/s for CH<sub>4</sub>-air and H<sub>2</sub>-air mixtures, respectively.

$$H = \frac{\int_V y \text{HRR}(x, y, z) dV}{\int_V \text{HRR}(x, y, z) dV} \quad (6.4)$$

Fig. 6.8 shows the flame length  $H$ , used in Eq. (6.3), for the two different mixtures. The red and blue solid lines represent the flame front in case of pure methane and pure hydrogen, respectively. The flame front is identified by means of those isolines which correspond to the heat release rate equal to 12.5% of max value for both methane-air and hydrogen-air mixture.

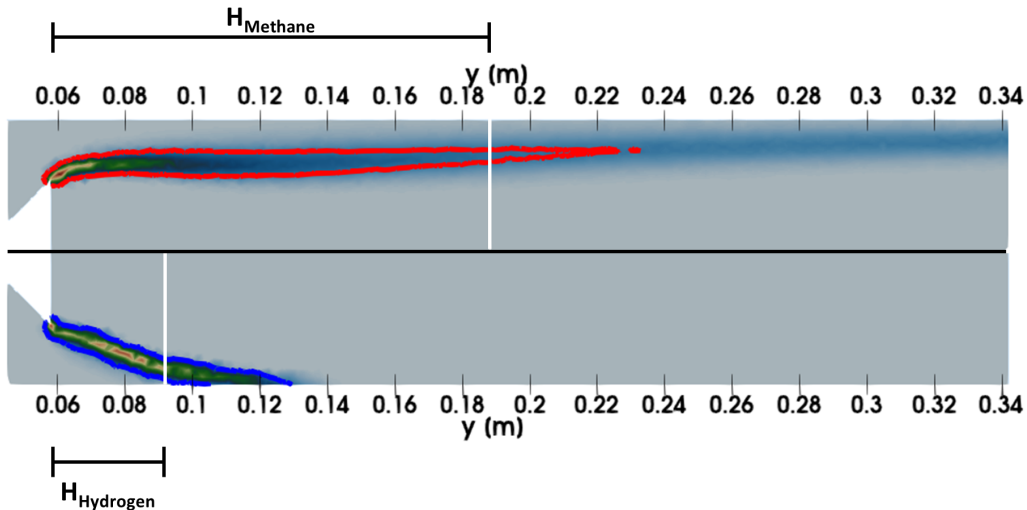


Figure 6.8: Schematic of flame for two different mixtures. The solid line denotes the flame front and  $H$  represents the length of the flame for the two mixtures.

Fig. 6.9 shows the heat release rate against time as obtained by RANS simulations. Colors refer to different particles, which are followed from the base of the flame to the flame front. The peak of the heat release rate in the burner fueled by  $CH_4$ -air (see Fig. 6.9a) is around the value of time equal 0.013 s. In the case fueled by  $H_2$ -air (see Fig. 6.9b) the peak is in correspondence of 0.0058 s. These values, obtained by RANS simulations, are in good agreement with the constant time delay calculated using Eq. (6.3).

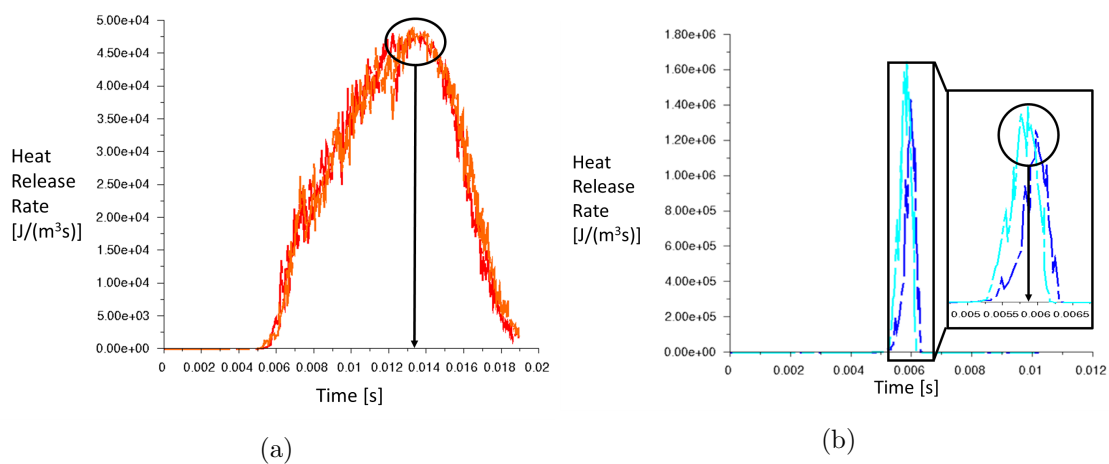


Figure 6.9: Heat release rate trends against time for Vanderbilt University burner: (a)  $CH_4$ -air mixture, (b)  $H_2$ -air mixture



In Fig. 6.10 a scatter plot of the distributed Time Delay against the Heat Release Rate (HRR) for the two mixtures have been reported. The ranges of distributed time delay are  $0.005 \div 0.018$  s and  $0.002 \div 0.008$  s for the pure methane and pure hydrogen mixtures, respectively.

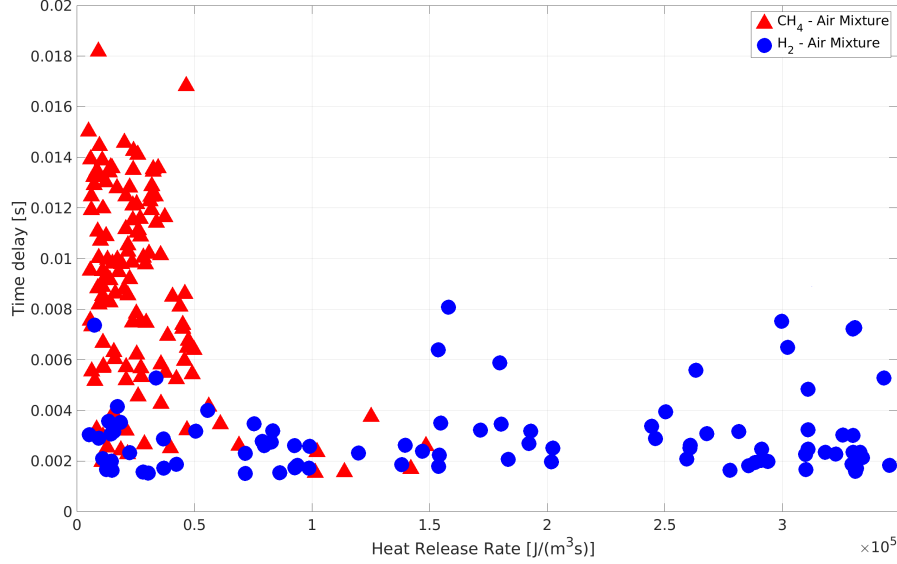


Figure 6.10: Comparison of the Time delay vs. heat release rate for Vanderbilt University burner fueled by methane-air and hydrogen-air mixtures

The constant values computed by means of the formulation proposed by *Æsøy* and *Aguilar* in [41, 117] for both the two cases are within the corresponding ranges of the distributed time delay. The combustion rate of the hydrogen-air mixture in the burner is higher than the one of the methane-air mixture due to the greater LHV of hydrogen compared to methane, see Fig. 5.34 and Fig. 6.9. Therefore, the time delay of the hydrogen-air mixture is slightly lower than that of the methane-air. Those parameters are the most important in order to take into account the actual HRR in *Acoustic Pressure and Frequency Domain* of COMSOL Multiphysics<sup>®</sup>.

### 6.3 Comparison between 100%CH<sub>4</sub> vs 100%H<sub>2</sub> mixture

The general formulation of the Rayleigh index  $\widehat{Ra}$ , in the frequency domain [121, 122], is a good help in order to locate the region of combustion chamber in which the instability occurs. The post-processing COMSOL facilities allow to calculate the real part of Rayleigh index  $\Re(\widehat{Ra})$  as follows:

$$\Re(\widehat{Ra}) = |\hat{p}| |\hat{q}| \cos(\varphi_q - \varphi_p) \quad (6.5)$$

where  $|\hat{p}|$  and  $|\hat{q}|$  indicate the absolute value of  $\hat{p}$  and  $\hat{q}$  respectively,  $\varphi_q$  is the phase of  $q$  and  $\varphi_p$  is the phase of  $p$ . The Fig. 6.11 shows the contour plot of local  $\Re(\widehat{Ra})$  of the Eq. (6.5) in the symmetry plane of the burner in the case of CH<sub>4</sub>-air and H<sub>2</sub>-air mixture. In order to perform a comparison of the results, the maximum value of  $\Re(\widehat{Ra})$

of the fourth mode for the two mixtures, is used as normalization factor. It is possible to notice that the shape is very different between the two mixtures. The higher positive value of  $\Re(\widehat{Ra})$  obtained in case of  $H_2$ -air mixture (Fig. 6.11b) confirms that the use of the hydrogen-air mixture in the burner makes the mode unstable with respect to the burner fueled by  $CH_4$ -air mixture. In Fig. 6.12 a distribution of time delay  $\tau$  in burner fueled by two mixtures is represented. When the  $H_2$ -air mixture is used the time delay  $\tau$  is smaller respect with  $CH_4$ -air mixture (see Fig. 6.12) due to the high combustion velocity of  $H_2$ -air fuel mixture with respect to  $CH_4$ -air mixture.

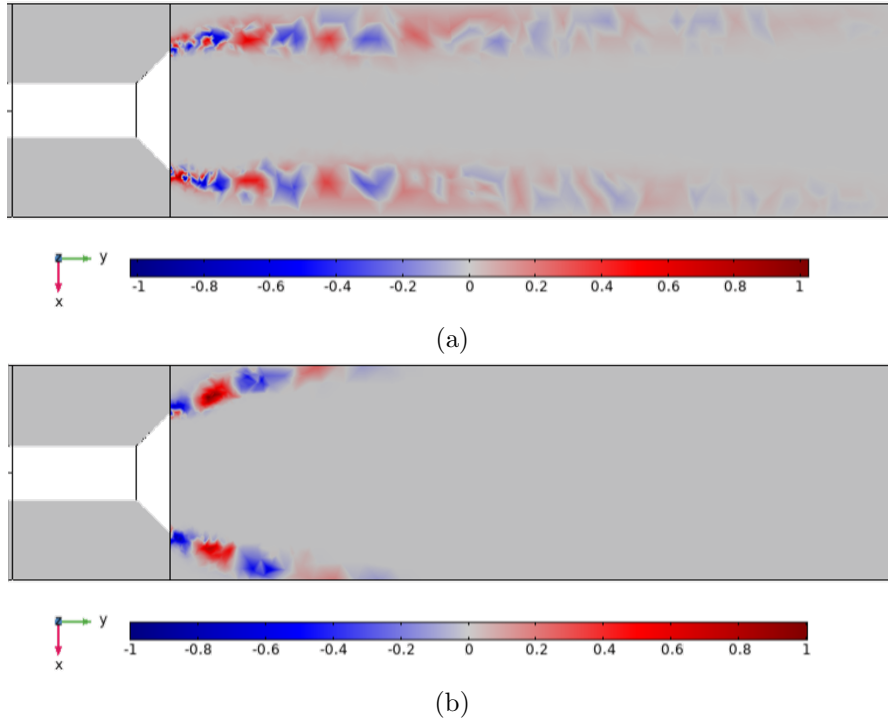


Figure 6.11: Comparison of the real part of Rayleigh index of Vanderbilt University burner fueled by (a) methane-air and (b) hydrogen-air mixtures.

After the studies on the Rayleigh index and time delay, the next step regards the sensitivity of the burner to the different fuel mixtures. In the case of hydrogen-air mixture the burner acoustic modes have been reported in Fig. 6.13. Frequency and growth rate (GR) values are reported in Table 6.3.

Table 6.3: Eigenmodes comparison between Vanderbilt University burner fueled by  $H_2$ -air and  $CH_4$ -air mixture

MODE TYPE	$CH_4$ NO FLAME	$CH_4$ FLAME	$H_2$ NO FLAME	$H_2$ FLAME	UNITS
Longitudinal	47.68	49.44+1.99i	54.18	60.11+4.15i	Hz
Longitudinal	259.73	259.96+0.17i	281.89	281.21+0.87i	Hz
Longitudinal	453.87	457.74+0.70i	541.78	539.06+2.88i	Hz
Longitudinal	571.88	571.65-0.038i	628.95	628.48+0.30i	Hz

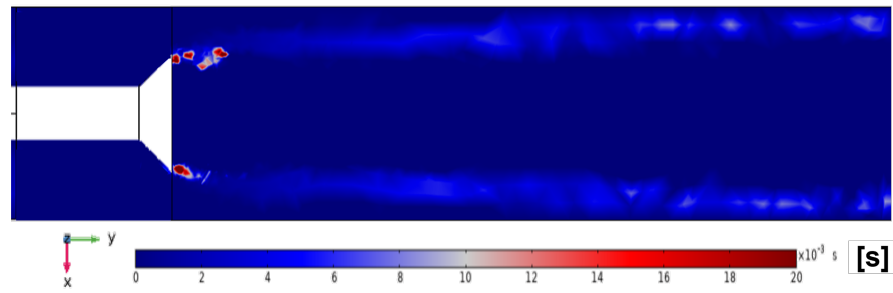
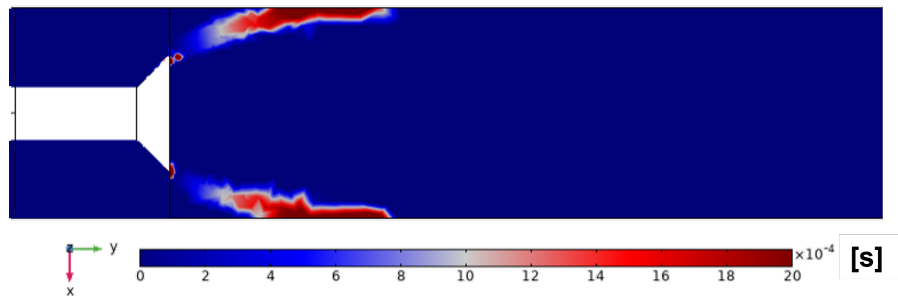
(a) Time delay  $CH_4$ -air mixture(b) Time delay  $H_2$ -air mixture

Figure 6.12: Comparison of the Time Delay  $\tau$  of Vanderbilt University burner fueled by methane-air and hydrogen-air mixtures.

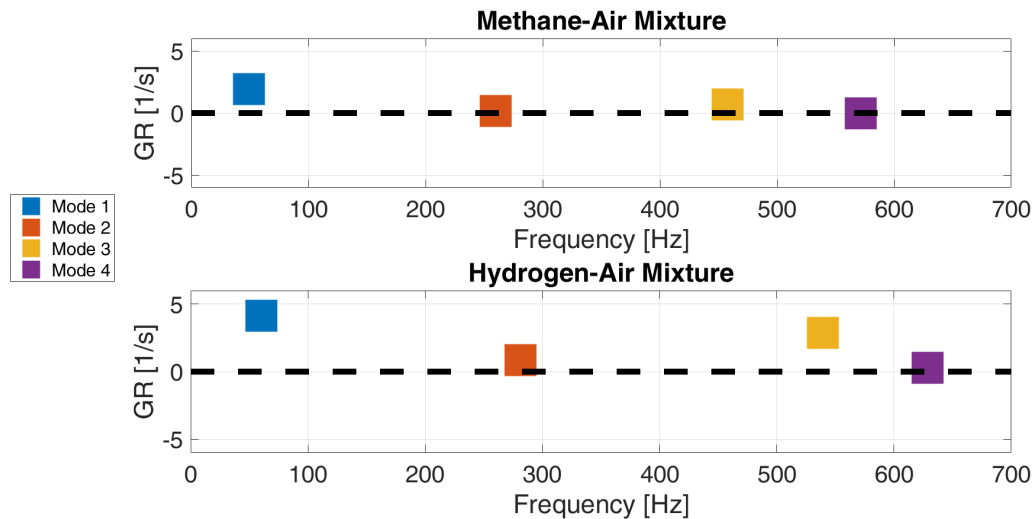


Figure 6.13: Comparison of frequencies and growth-rates for the two cases fueled with  $CH_4$ -air and  $H_2$ -air

In the case fueled by hydrogen-air mixture, the magnitude of frequency and Growth Rate increases with respect to the ones of methane-air mixture. The greater reaction rate and smaller time delay of hydrogen-air mixture stimulate a change in the relationship between pressure fluctuation and unsteady heat release [39]. The compactness of the flame shape in the 100% hydrogen case (see Fig. 5.34) influences the relationship between unsteady heat release and pressure fluctuations and, hence, the thermoacoustic characteristic of

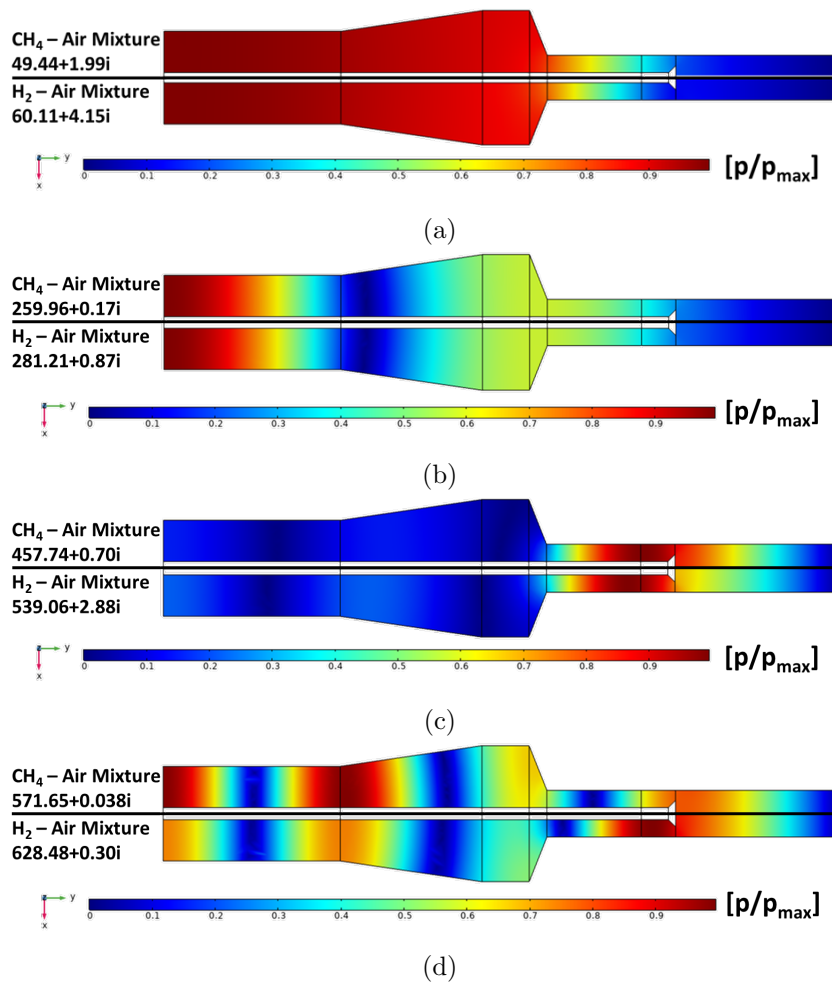


Figure 6.14: Comparison of the acoustic pressure of the first four modes when the two mixtures ( $CH_4$ -air and  $H_2$ -air) are employed

the burner. Therefore, flame position has a crucial role in determining the dynamic state of burner fueled by pure hydrogen. Fig. 6.13 shows the increase in instability of the first two modes in the model fueled with hydrogen-air mixture. For the same mixture, the modes at frequencies greater than 400 Hz shift towards even larger values.

In Fig. 6.14 the total acoustic pressure normalized by the max value for the first four modes in the case of hydrogen-air and methane-air mixture have been reported. For the first two modes (Fig. 6.14a, 6.14b) the values of acoustic pressure for the case of hydrogen-air mixture are similar to the ones of methane-air mixture. Instead, for the third mode (Figure, 6.14c), the position of the acoustic pressure peak shifts towards the inlet section when the  $H_2$ -air mixture is used. In the fourth mode (Fig. 6.14d), the values of the acoustic pressure decrease in the model of pure hydrogen respect the ones of  $CH_4$ -air mixture. This preliminary thermoacoustic analysis shows that due to the change in flame topology, variation of the heat release rate and time delay fields, the modes in the burners fueled by hydrogen-air mixture are more likely to become unstable than the same mode in the case fueled by methane-air mixture. By using a relatively simplified method, the thermoacoustic effects of hydrogen-air mixture on a bluff body

burner originally designed to burn methane are investigated. In the next future, it will be possible to develop the Flame Transfer Function by including perturbations to URANS-LES simulations.

## Chapter 7

# Application on micro-turbine AE-T100

Fuel enrichment with hydrogen is important in the current energy situation that is aimed at decarbonization, as mentioned above. In this context, there are many benefits to use these kinds of blends in a very adaptable and variable application like the micro gas turbine (mGT). The CFD simulations of the AE-T100 burner fueled by three distinct fuel mixtures (100%  $CH_4$ , 90%  $CH_4$  and 10%  $H_2$ , and 70%  $CH_4$  and 30%  $H_2$ ) is described in this chapter. The effects of hydrogen on thermoacoustic instabilities have been highlighted using the fluid-dynamic quantity distributions, created from the RANS simulation results, in the flame response function (FRF). The work on the burner of the micro gas turbine AE-T100, developed during the visiting period of my PhD course (January-August 2022) in partnership with the Thermal Engineering and Combustion Unit of the University of MONS, and in particular with Professor Ward De Paepe, and researchers Jérémy Bompas, and Alessio Pappa, is presented in this chapter.

### 7.1 AE T100 Micro-Turbine Burner

The AE-T100 is the mGT taken into consideration in this dissertation. According to [123], this system generates electrical and thermal power of 100  $kW_e$  and 160  $kW_{th}$  respectively with the corresponding efficiency of 50% and 30%. The mGT AE-T100 operates according to the Brayton cycle. In the centrifugal compressor (1) of Fig. 7.1, the input air is first compressed. The hot gas that is exhausted from the radial turbine (4) heats the air that leaves the compressor by means of a recuperator (2). The air is burned with liquid or gaseous fuel in the combustion chamber (3), to reach the turbine inlet temperature (TIT) to 950°C. The turbine generates the power required to drive the compressor. If the AE-T100 is utilized in combined-heat and power applications (CHP), the leftover heat of the gasses that leave the recuperator is utilized in the economizer (6) of Fig. 7.1 to generate hot water or steam.

The combustion chamber of the AE-T100 is the subject of the CFD and thermoacoustic analysis in this thesis (see Fig. 7.2). The counterflow of the input air in the space between the outer casing and inner walls is reported in Fig. 7.2a. To reduce TIT, the air first enters the dilution holes at the end of the combustion chamber. The length of combustion chamber is three times its diameter ( $D = 103$  mm).

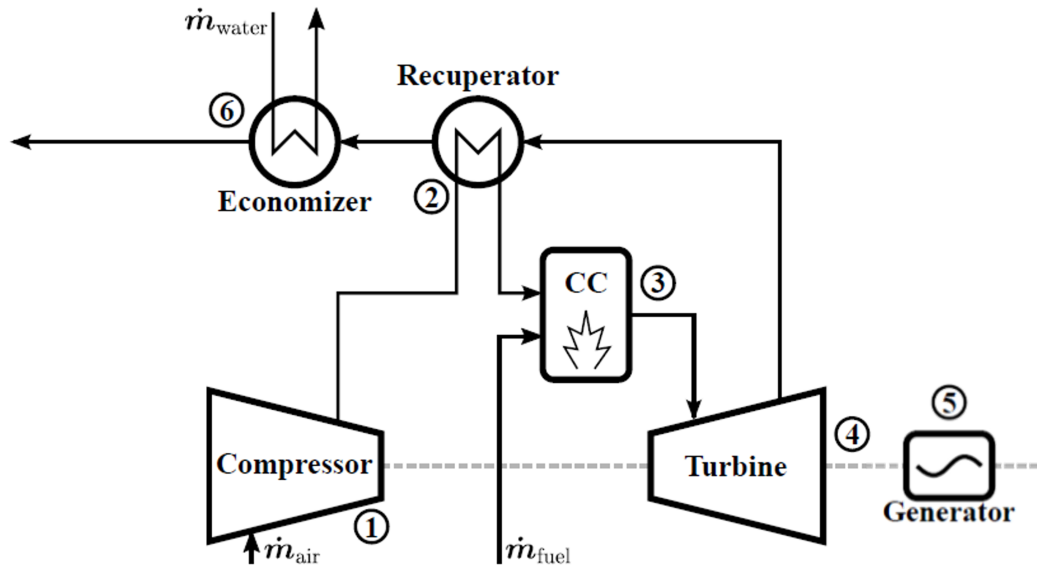


Figure 7.1: Cycle and component of the Turbec T100 mGt system are: (1) centrifugal compressor, (2) recuperator, (3) low- $NO_x$  burner, (4) radial turbine, (5) high speed generator, (6) economizer. (inspired by [124])

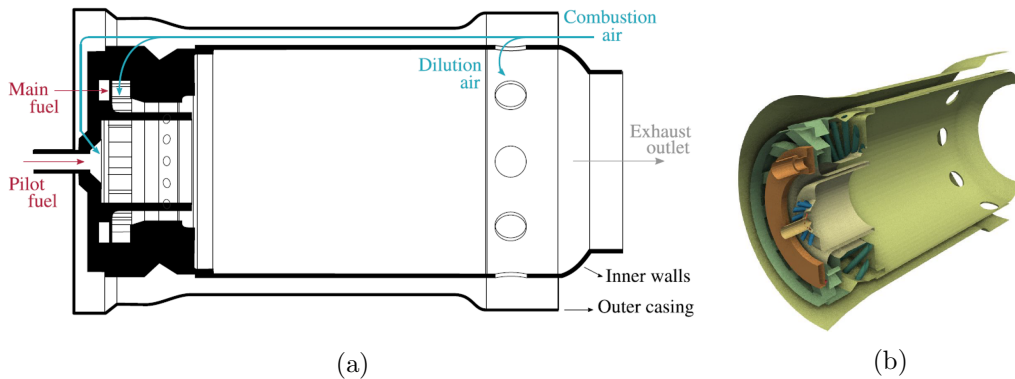


Figure 7.2: Burner AE-T100: (a) Longitudinal view. The air enters in counter-current in the gap between the outer casing and inner walls. The pilot and main fuel enter through injector on the external surface of the inner walls (inspired by [125]), (b) isometric cut the view (reprinted from [126]).

The injected fuel is divided into two lines: the pilot line, which uses 6 nozzles to create the diffusion flame, and the toroidal chamber, which uses 15 nozzles to create the premixed flame (indicated as pilot and main in Figure 7.3 respectively). Through the 12 jet holes of swirler 1, a portion of air (besides the air utilized for the dilution holes) is mixed with the pilot fuel (see Fig. 7.3). The 15 radial vanes of swirler 2 and 30 jet holes of swirler 2', which are highlighted in Fig. 7.3, allow residual air to mix with the main fuel. Table 7.1 summarizes the number of holes or vanes and the dimension of the burner AE-T100.

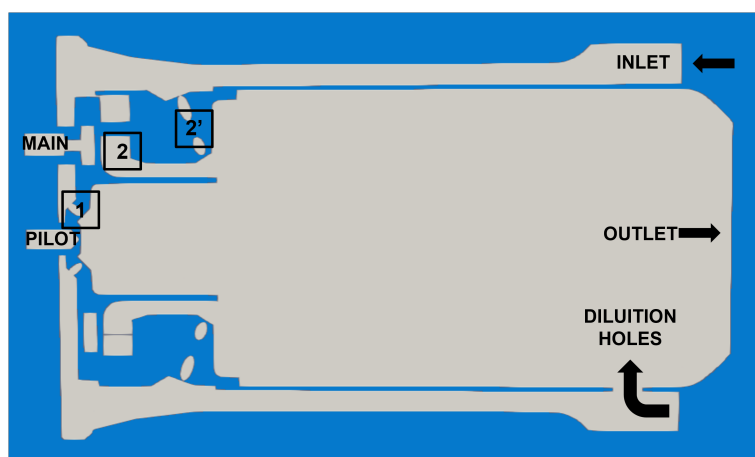


Figure 7.3: Fuel injection system main and pilot through plane highlighting the counter-flow air inlet, the pilot (1) and main (2,2') swirlers, and the dilution holes.

Table 7.1: Air supply in burner AE-T100

	NUMBER OF HOLES/VANES	DIAMETER DIMENSION	UNITS
Dilution holes	9	30	mm
Swirler 1	12	3.5	mm
Swirler 2	15	external diameter 34 inner diameter 28	mm mm
Swirler 2'	30	5	mm

## 7.2 Numerical setup of CFD Simulations

The preliminary RANS simulation has been run using pure methane injection at full load of the AE-T100,  $100 kW_e$ , to describe the flow in the combustion chamber (Table 7.2). A previously verified thermodynamic cycle analysis (De Paepe et al. [127]) was used to establish the total air mass flow rate into the combustion chamber. This case is the reference case, used to validate the CFD simulations. Without altering the geometry of the combustor the main flame in the second case (see Table 7.2) is fueled by methane

Table 7.2: Boundary and inlet conditions of the simulated cases - inlet fuel:  $T_{fuel} = 288$  K, inlet air:  $\dot{m}_{air} = 690$  g/s,  $T_{air} = 865$  K

	PARAMETERS	100% $CH_4$	90% $CH_4$ AND 10% $H_2$	70% $CH_4$ AND 30% $H_2$	UNITS
Pilot	Species	$CH_4$	$CH_4 + H_2$	$CH_4 + H_2$	
	$\dot{m}$	0.8	0.66	0.62	g/s
	LHV	50.1	51.1	53.7	kJ/g
	PARAMETERS	REF-100% $CH_4$	90% $CH_4$ AND 10% $H_2$	70% $CH_4$ AND 30% $H_2$	UNITS
Main	Species	$CH_4$	$CH_4 + H_2$	$CH_4 + H_2$	
	$\dot{m}$	5.98	5.86	5.58	g/s
	LHV	50.1	51.1	53.7	kJ/g



enriched with 10%<sub>v</sub> $H_2$ . The last mixture used in burner of AE-T100 is 70%  $CH_4$  and 30%  $H_2$ . In each mixture, 90% of the total mass flow rate is used into the main and the remaining 10% is used into the pilot. The inlet fuel velocity in the main and pilot of the last two mixtures, has been calculated by assuming the inlet air mass flow rate,  $\dot{m}_{air} = 690$  g/s, and thermal power,  $P_{input-burner} = 333$  kW as constants. The 3D RANS CFD simulations on burner of AE-T100 have been carried out by means open source code OpenFOAM [128]. The reactingFoam solver has been used in order to perform reacting flow simulations. The converge criteria for the chemical transport equation have been set to  $10^{-7}$  for all mixtures, and to  $10^{-8}$  for velocity, enthalpy turbulent kinetic energy, and dissipation of turbulent kinetic energy rate variables. The robustness and reasonable computational cost of the  $k - \epsilon$  turbulence model led to its implementation in the simulations. In the case of this burner, due to the absence of the bluff-body, we do not expect wide flow separation region so (as explained previously in section 5.2.4) the  $k - \epsilon$  turbulence model turns out to be consistent with the case studied. Lean-premix technology is used by the AE-T100 combustor to control the flame temperature and  $NO_x$  emissions. A non-premixed pilot flame is required since the operation point is so close to the lean flammability limit to stop the blow-off. Due to the presence of premixed and diffusion flames in this burner, the combustion regime cannot be called entirely premixed. An analysis on combustion model implemented on burner of AE-T100 has been carried out by Giuntini et al. [129]. The Steady Laminar Flamelet (SLF) model predicts species and temperature fields with poor accuracy. In terms of temperature field, Flamelets Generated Manifold (FGM) performs better, but it overestimates  $NO_x$  emissions and handles  $CO$  in an inconsistent manner. Eddy Dissipation Concept (EDC) gives accurate predictions on the combustor behavior with good predictions on  $NO_x$  and  $CO$  when paired with the *GRI-mech* 3.0 chemical mechanism [108]. Since the AE-T100 combustor has both a diffusive (pilot) and a premixed flame (main), the EDC model was chosen as the combustion model. The dissipation of turbulence kinetic energy into heat is known to occur in fine structures where the smallest eddies are dissipated due to the work done by molecular forces, according to the turbulence energy cascade theory [130]. These tiny structures have dimensions typical of the Kolmogorov scales. The reacting part is treated as a perfectly stirred reactor since the speed of a chemical reaction largely depends on how long it takes to mix the reagents in a molecular fine structure. The EDC model implies that chemical reactions take place in these small structures where reactants are combined at the molecular level and react at high temperatures. For all mixtures, the simulation of the AE-T100 burner has been performed by using the *GRI-mech* 3.0 chemical mechanism [108] that consists of 53 chemical species and 325 reactions. However, the computational resources are usually exceeded by the system of ordinary differential equations (ODE) for chemical kinetics equations. By choosing the dominating active species, it is possible to dynamically reduce the number of species. On the other hand, in cells where conditions are judged to be sufficiently comparable, the outcomes of previously computed solutions are tabulated and interpolated. These two reduction strategies are combined by the Tabulation of Dynamic Adaptive Chemistry (TDAC) algorithm, which is used in our research [131].

### 7.2.1 CFD Grid refinement

In this study, the mesh of the burner includes all fluid domains of the combustion chamber. Fully 3D hexahedral grids, from 1.7 to 7.3 million cells, have been used in order to

conduct a mesh sensitivity analysis on the temperature and velocity field of the reference case (see Table 7.2). On the complex shapes of the swirlers and the primary combustion zone, a specific refinement has been set. For the small elements of pilot and main fuel nozzles, a finer discretization has been used (see Fig. 7.5a). Furthermore, Fig. 7.5b shows that the results in terms of temperature and velocity at  $0.19D$  downstream of the pilot injectors section (see arrow in Fig. 7.5a and the red line in Fig. 7.4) obtained using respectively a mesh of 4.3M cells and 7.3M cells are very close.

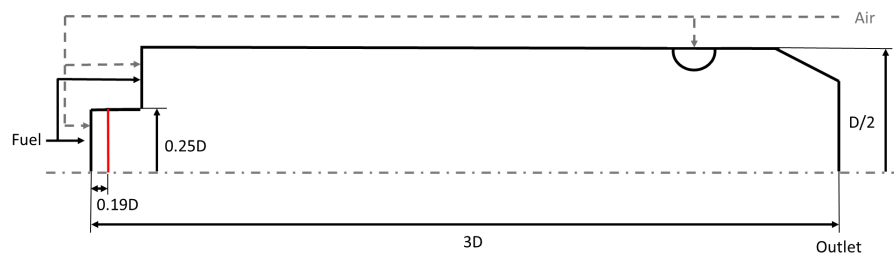


Figure 7.4: 2D geometry of AE-T100 burner. The red line highlights the section  $0.19D$  downstream the pilot injector on which the mesh sensitivity analysis has been carried out.

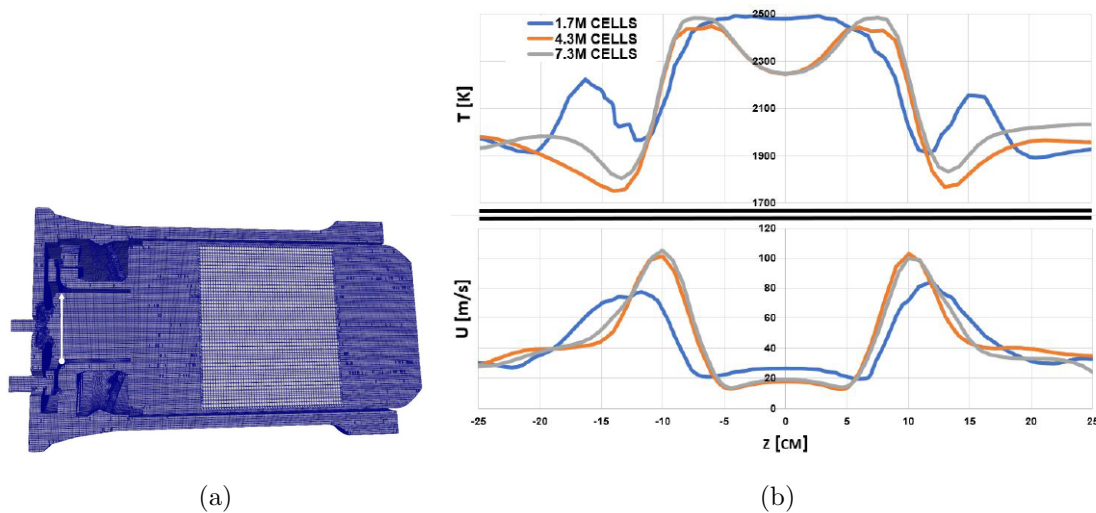


Figure 7.5: Burner AE-T100: 3D hexahedral mesh of AE-T100 burner. The mesh is made up of 4.3M cells, with refinement in the injectors, counter-flow air channel, first part of the primary flame zone, pilot and zone around the dilution holes, (b) mesh sensitivity analysis on temperature and velocity field in the flame zone, in the plane of the pilot combustion chamber  $0.19D$  downstream the pilot injectors section (see the arrow in Fig. 7.5a and the red line in Fig. 7.4) (inspired by [126]).

### 7.3 CFD comparison between 100% $CH_4$ mixture vs $H_2$ - $CH_4$ blends

In the RANS study on burner of AE-T100, the aim is to develop the field of fluid-dynamic quantities in order to use it in the thermoacoustic simulations, as well as studying the impact of progressive increase of hydrogen, until 30% by volume, in the fuel blend. Starting with a constant air flow rate of  $\dot{m}_{air} = 690$  g/s and a constant thermal power of  $P_{th} = 333$  kW, the fluid-dynamic parameters of RANS simulations for the three mixtures are set. Fig. 7.6a shows the difference in axial velocity between three mixtures. Vortex positions remain unaltered but the velocities near the dilution holes change between the three mixtures.

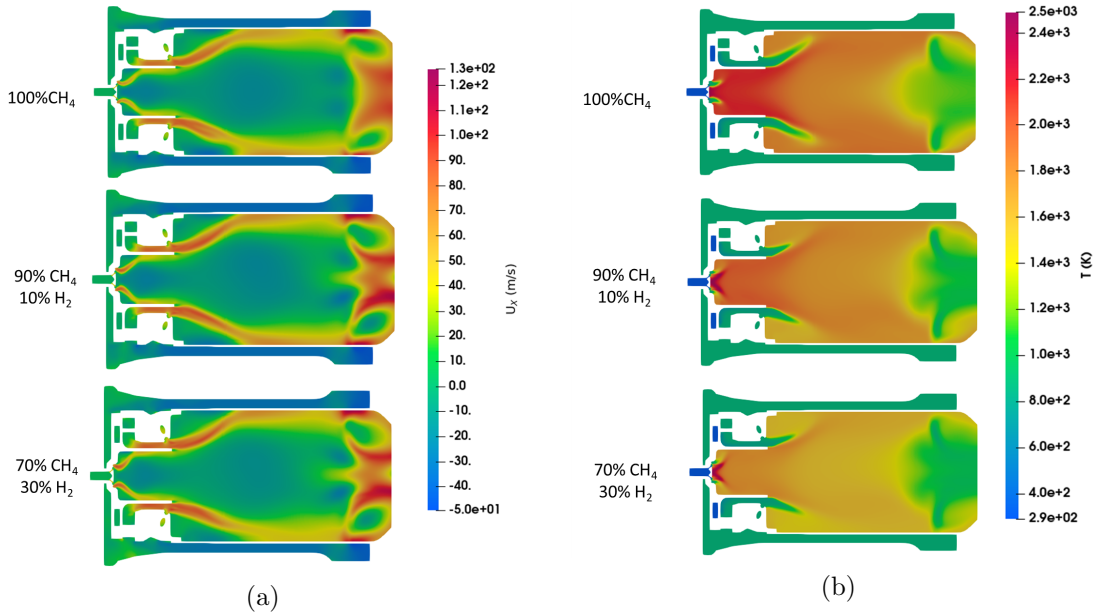


Figure 7.6: Comparison between three mixtures on longitudinal plane in terms of: (a) axial velocity contours, (b) temperature contours.

The temperature distribution is clearly influenced by the degree of hydrogen content in the mixture as Fig. 7.6b shows. The reference case fueled by pure methane is shown in the first image of Fig. 7.6b in which the peak of temperature  $T_{max} = 2507$  K, in the longitudinal plane, is in perfect agreement with reference case described by De Santis et al. in [132]. When the volume of hydrogen in the mixture increases, a higher temperature peak is observed close to the pilot flame whereas the temperature slightly drops inside the main combustor chamber, as shown in Fig. 7.6b. By maintaining a constant air mass flow rate and thermal power, the equivalence ratio will change when the mixture's hydrogen content rises (Fig. 7.7a), resulting in a leaner mixture characterized by a lower adiabatic temperature. In Fig. 7.7b the contours of equivalence ratio in the plane of the combustion chamber  $0.30D$  downstream of the pilot injectors section have been reported. The values of equivalence ratio decrease as the volume of hydrogen in the mixture increases. This aspect highlights that the increase of hydrogen content leads to a leaner flame.

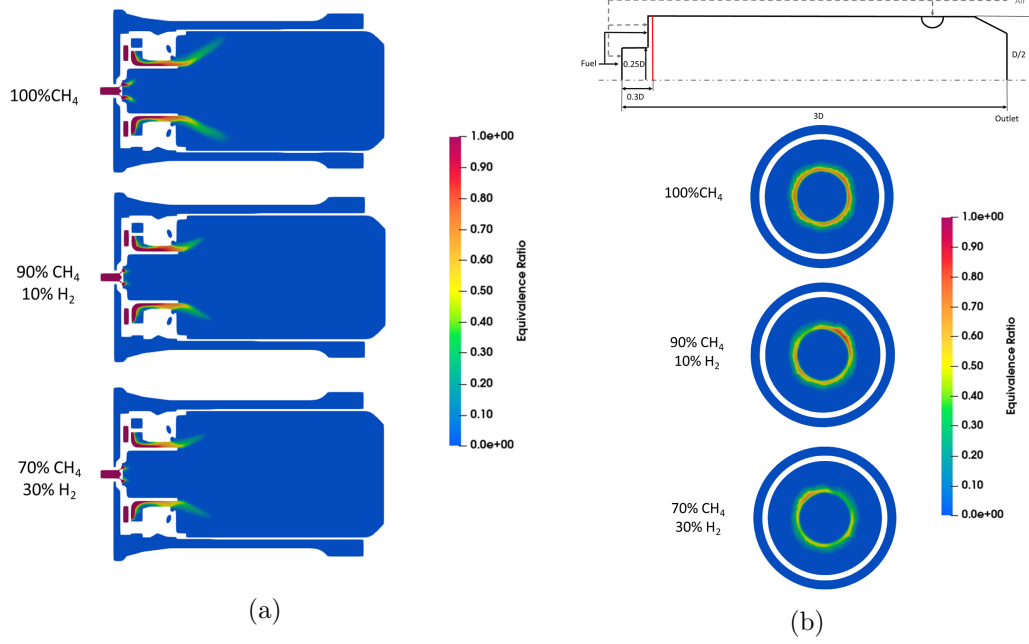


Figure 7.7: Comparison between three mixtures in terms of equivalence ratio contours: (a) in the longitudinal plane, (b) in the plane of the combustion chamber  $0.30D$  downstream of the pilot injectors section.

## 7.4 Natural frequencies of the AE-T100 burner

Starting from a wave equation in one-dimensional form (see Eq. (7.1)):

$$\frac{\partial^2 \hat{p}}{\partial t^2} - c^2 \frac{\partial^2 \hat{p}}{\partial x^2} = 0 \quad (7.1)$$

where  $x$  is the axial coordinate, the general solution of Eq. (7.1) is the following:

$$\hat{p}(x, t) = \hat{A} \cdot f(x - ct) + \hat{B} \cdot g(x + ct) \quad (7.2)$$

where  $A$  and  $B$  are arbitrary constants (real and complex) determined by the boundary conditions, and  $f$  and  $g$  are generic functions. Assuming that the time dependence is exponential type  $e^{i\omega t}$ , Eq. (7.2) becomes:

$$\hat{p}(x, t) = \hat{A} \cdot e^{i\omega t - \frac{x}{c}} + \hat{B} \cdot e^{i\omega t + \frac{x}{c}} \quad (7.3)$$

The first term of RHS of Eq. (7.3) is equal to  $A$  equally for  $x = t = 0$  and for  $x = c \cdot t$  and, hence, depicts a forward-propagating wave in the positive direction of  $x$  with velocity  $c$ . While, the second part of RHS of Eq. (7.3) depicts a backward-propagating wave in the negative direction of  $x$  with velocity  $c$ . For this reason, the velocity  $c$  is the result of superposition of two progressive waves in opposite directions. Eq. (7.3) can be rewritten as follows:

$$\hat{p}(x, t) = \hat{A} \cdot e^{-ikx} + \hat{B} \cdot e^{+ikx} \cdot e^{i\omega t} \quad (7.4)$$

where  $k = \omega/c = 2\pi/\lambda$  is the wave number and  $\lambda$  is the wave length. The corresponding acoustic velocity  $\hat{u}$  is:

$$\hat{u}(x, t) = (\hat{C} \cdot e^{-ikx} + \hat{D} \cdot e^{+ikx}) \cdot e^{i\omega t} \quad (7.5)$$

where  $\hat{C} = \frac{\hat{A}}{\rho \bar{c}}$  and  $\hat{D} = -\frac{\hat{B}}{\rho \bar{c}}$ . By rearranging the denominator Eq. (7.5) becomes:

$$\hat{u}(x, t) = \frac{1}{Z} (\hat{A} \cdot e^{-ikx} - \hat{B} \cdot e^{+ikx}) \cdot e^{i\omega t} \quad (7.6)$$

where  $Z = \rho \bar{c}$  in the acoustic impedance defined as ratio between acoustic pressure and the acoustic velocity of progressive wave. By using the aforementioned equations in matrix form, an analysis of frequencies of the AE-T100 1D burner has been carried out by means a simple Matlab code. Thermoacoustic simulations are only performed on the internal portion of the combustor, not considering the gap between the outer casing and the inner walls and the swirlers (see Fig. 7.2a and 7.3). In this code the input is the pressure ( $p = 400000$  Pa) and temperature ( $T = 955$  K) in inlet section and the length of duct (see Fig. 7.8). The code finds the value of matrix determinant as a function of angular frequency  $\omega$  and plots the first four natural modes of the burner (see Fig. 7.5b). The natural frequencies of Fig. 7.8 are summarized in Table 7.3.

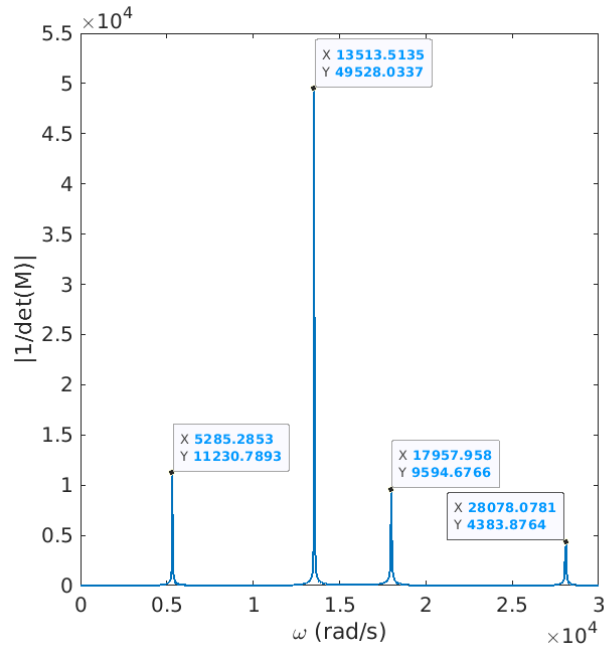


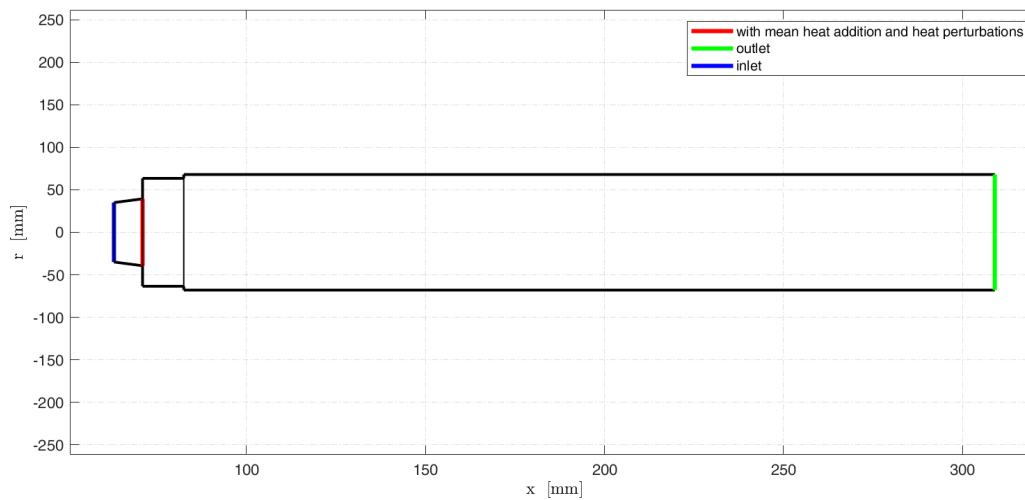
Figure 7.8: First four natural frequencies of AE-T100 burner.

Table 7.3: Natural frequencies calculated by matlab code.

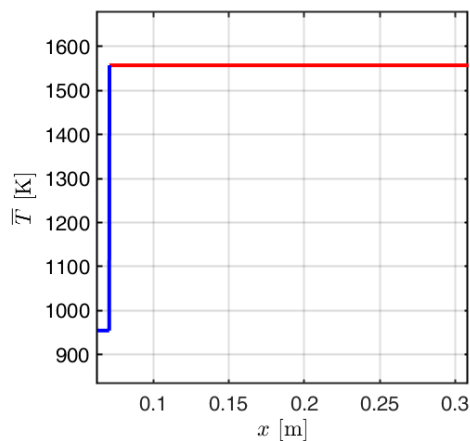
MODES	FREQUENCIES IN <i>rad/s</i>	FREQUENCIES IN <i>Hz</i>
First	5285.28	841.18
Second	13513.51	2150.74
Third	17957.96	2858.09
Fourth	28078.08	4468.76

## 7.5 Numerical setup of Low Order solver

In order to validate the thermoacoustic 3D simulations, developed by means Helmholtz solver, a preliminary analysis by using a low order code has been carried out. OSCILOS is a low-order simulator wrote in Matlab<sup>®</sup>/Simulink<sup>®</sup> (see section 3.5.1). In the case of AE-T100 burner, by using the flame sheet model described in section 3.5.1, the code has been set with a Mach number of 0.001, a pressure inlet of 400000 Pa and a ratio between the temperature of the burnt and unburnt gas  $T_b/T_u = 1.63$ , as Fig. 7.9b shows.



(a)

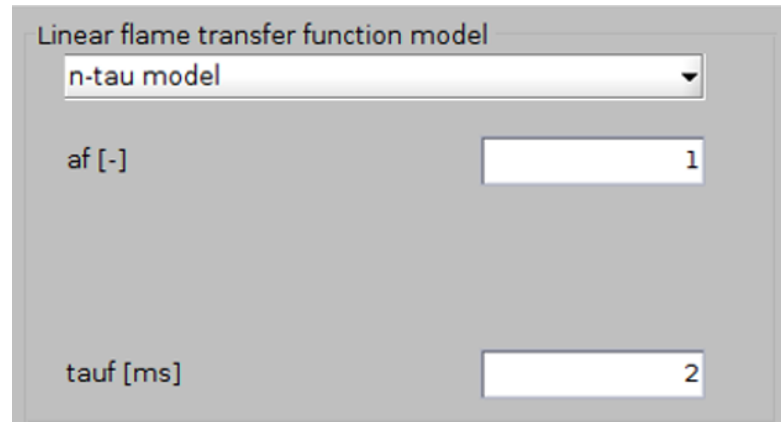


(b)

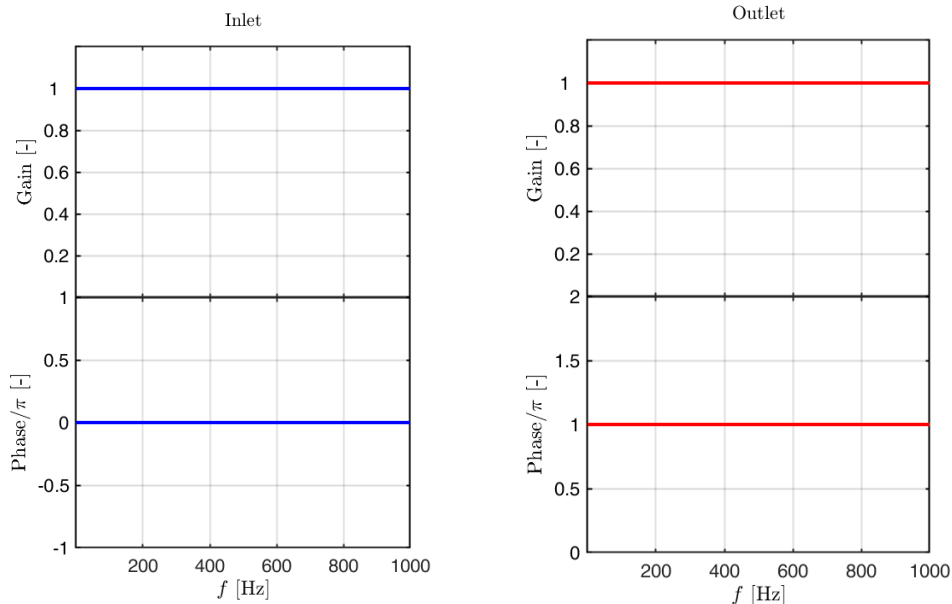
Figure 7.9: Settings of AE-T100 burner in OSCILOS Simulator:(a) Geometry (b) thermal proprieties.

Flame model and boundary condition of the low order model of AE-T100 burner are summarized in Fig. 7.10. The  $n - \tau$  flame model has been used by setting  $n = 1$  and

$\tau = 2$  ms (see Fig. 7.10a). The boundary conditions of inlet closed and outlet open have been chosen (see Fig. 7.10b and 7.10c).



(a)



(b)

(c)

Figure 7.10: Settings of AE-T100 burner in OSCILOS Simulator:(a)  $n - \tau$  parameters (b) inlet boundary (c) outlet boundary.

The results of simulation with OSCILOS code are summarized in Fig. 7.11. The real part of this modes is close to natural frequencies calculated by the Matlab code (see Table 7.4). The difference between the results of two codes is due to the introduction of flame sheet in the model developed by OSCILOS code.

Table 7.4: Comparison between natural modes calculated by Matlab code and modes calculated by OSCILOS code.

MODES	NATURAL MODES BY MATLAB CODE	MODES BY OSCILOS CODE	UNITS
First	841.18	803.82 + 2.83i	Hz
Second	2150.74	2396.30 + 12.08i	Hz
Third	2858.09	3974.30 + 7.25i	Hz
Fourth	4468.76	5542.60 - 26.61i	Hz

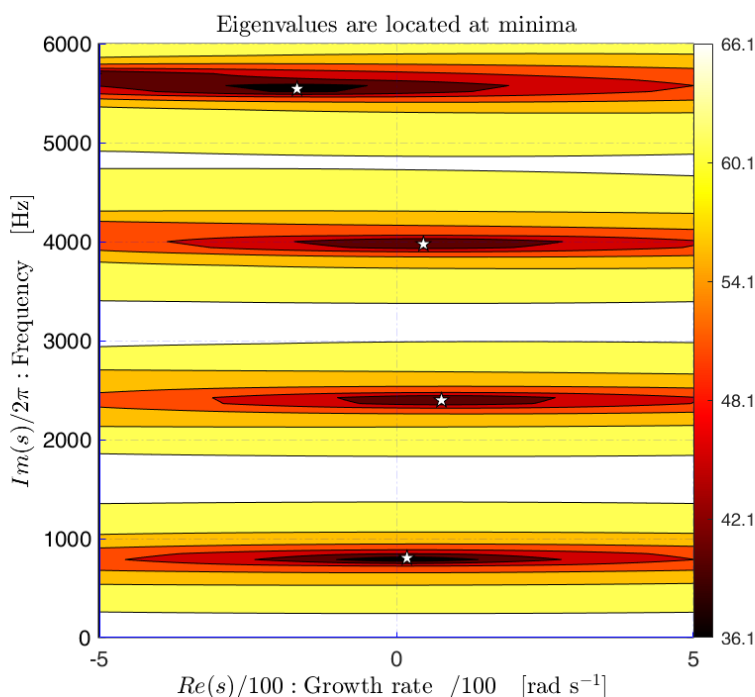


Figure 7.11: First four frequencies of AE-T100 burner calculated by OSCILOS code.

## 7.6 Validation of Helmholtz solver

The first Helmholtz solver simulation by using the flame sheet model, described in section 3.5.2, has been carried out in order to validate the setting respect with the results from OSCILOS code. The benchmark case is the burner fueled by methane-air mixture. For this kind of 3D simulations module Pressure Acoustic and Frequency Domain of Helmholtz solver COMSOL Multiphysics<sup>®</sup> has been used. The only component of the geometry taken into account in this validation study is the combustion chamber, as Fig. 7.12 shows. The boundary condition of closed wall was imposed at the inlet section ( $u' = 0$ ). Moreover, the outlet section of the combustion chamber has been considered acoustically open ( $p' = 0$ ). The parameters of the simulations are summarized in Table 7.5. The factor  $\beta$  is calculated in the same way as section 3.5.2.

The frequencies of the first four longitudinal modes calculated by low order code and



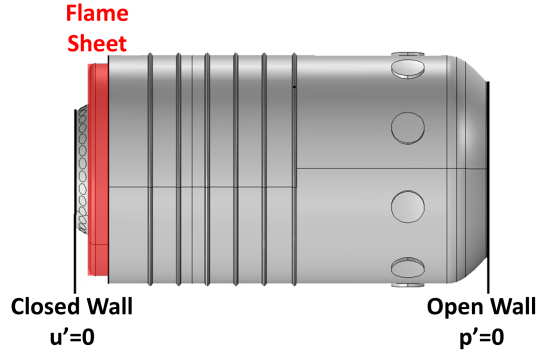


Figure 7.12: Geometry and boundary conditions for the AE-T100 burner validation scenario in COMSOL Multiphysics<sup>®</sup>.

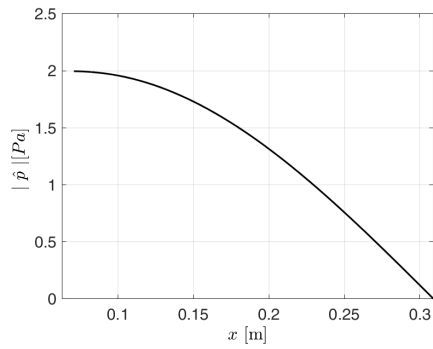
Table 7.5: Parameters of COMSOL Multiphysics<sup>®</sup> simulations of AE-T100 burner by using the flame sheet model.

PARAMETERS	VALUES	UNITS
$T_{air}$ = air temperature	865	K
$T_{fuel}$ = fuel temperature	300	K
$T_{mix}$ = temperature upstream flame sheet	955	K
$\rho_{mix}$ = density upstream flame sheet	1.2685	$kg/m^3$
$c_{mix}$ = speed of sound upstream flame sheet	687.76	m/s
$p$ = pressure	$4 \times 10^5$	Pa
$MW_{mix}$ = molecular weight upstream flame sheet	0.02518	kg/mol
$T_m$ = temperature from the flame sheet	1700	K
$\rho_m$ = density from flame sheet	1.0453	$kg/m^3$
$MW_m$ = molecular weight from flame sheet	0.02813	kg/mol
$c_m$ = speed of sound from flame sheet	817.49	m/s
$\tau$ = time delay	0.002	s
$\beta$ = factor provides a measure of the intensity of the heat release	0.53	
$s$ = thickness of the heat release zone	0.0115	m

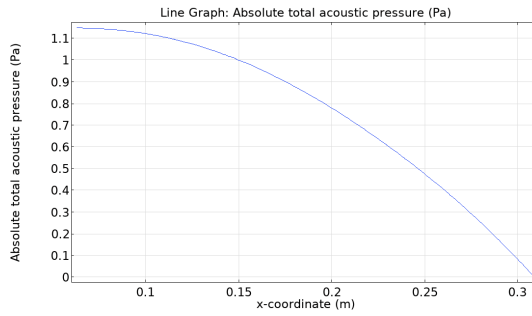
Table 7.6: Comparison between modes calculated by two code.

MODES	MODES BY OSCILOS CODE	MODES BY HELMHOLTZ SOLVER	UNITS
First	803.82 + 2.83i	825.12+8.89i	Hz
Second	2396.30 + 12.08i	2439.0432 + 19.63i	Hz
Third	3974.30 + 7.25i	3640.5868 +0.27i	Hz
Fourth	5542.60 - 26.61i	4019.09 -22.28i	Hz

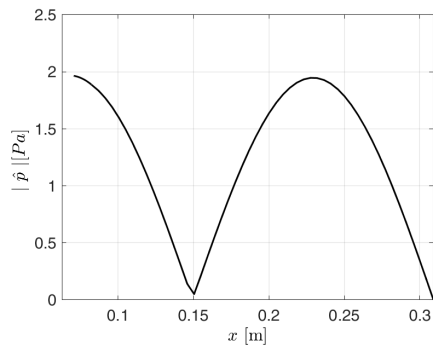
Helmholtz solver code are summarized in Table 7.6. The results of this first simulation are very close to the modes found by the low-order model (see Fig. 7.13). The difference between the curves is due to the difference between 2D simulation developed by OSCILOS and 3D simulation developed by COMSOL Multiphysics<sup>®</sup>.



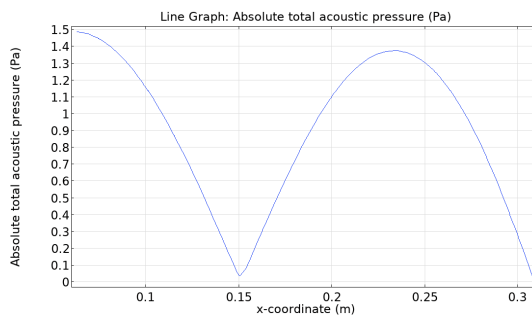
(a)



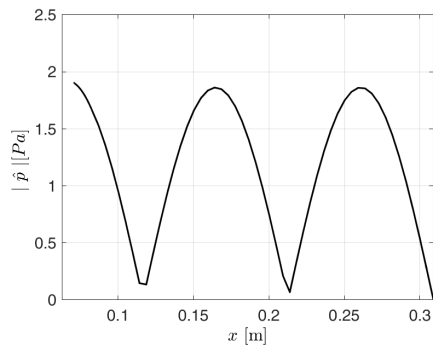
(b)



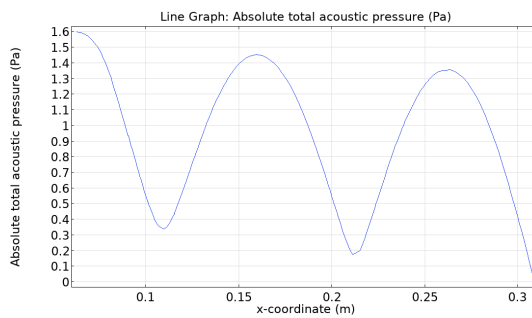
(c)



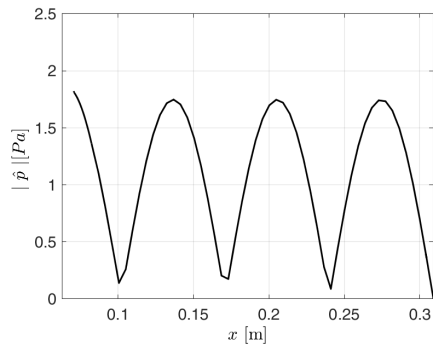
(d)



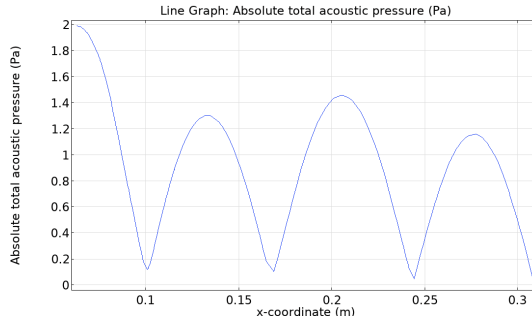
(e)



(f)



(g)



(h)

Figure 7.13: Comparison between first four modes of AE-T100 burner fueled by methane-air mixture calculated by: (a)(c)(e)(g) OSCILOS code, (b)(d)(f)(h) COMSOL Multiphysics<sup>®</sup> solver.

## 7.7 Numerical setup of Helmholtz solver Simulations

After the numerical assessment, a simplified AE-T100 burner model was considered. To properly model the instabilities during the combustion process, the information on heat release, time delay, flow field, pressure, and temperature from OpenFOAM CFD simulations are used in the Helmholtz solver. Also, the field of axial velocity is used in Helmholtz solver in order to take into account the mean flow (in the same way described from Eq (3.40) in section 3.5.2). Therefore, in this simulation, the flame sheet model is replaced by the distribution fields of the above-mentioned properties. The only components of the geometry taken into account in the thermoacoustic study are the combustion chamber and the pilot chamber duct. This decision was made since the section variation in this type of investigation is quite important. Fig. 7.14 shows the geometry and boundary conditions. In the inlet section closed wall ( $u' = 0$ ) was imposed. Moreover, the outlet section of the combustion chamber has been considered acoustically open ( $p' = 0$ ). The parameters of the simulations are summarized in Table 7.7.

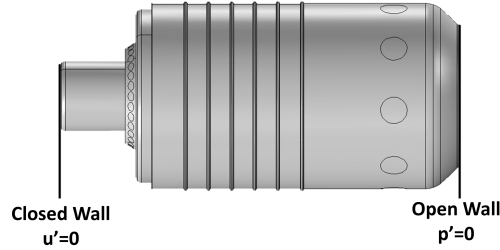


Figure 7.14: Geometry and boundary conditions of the AE-T100 burner in thermoacoustic simulation in COMSOL Multiphysics<sup>®</sup>.

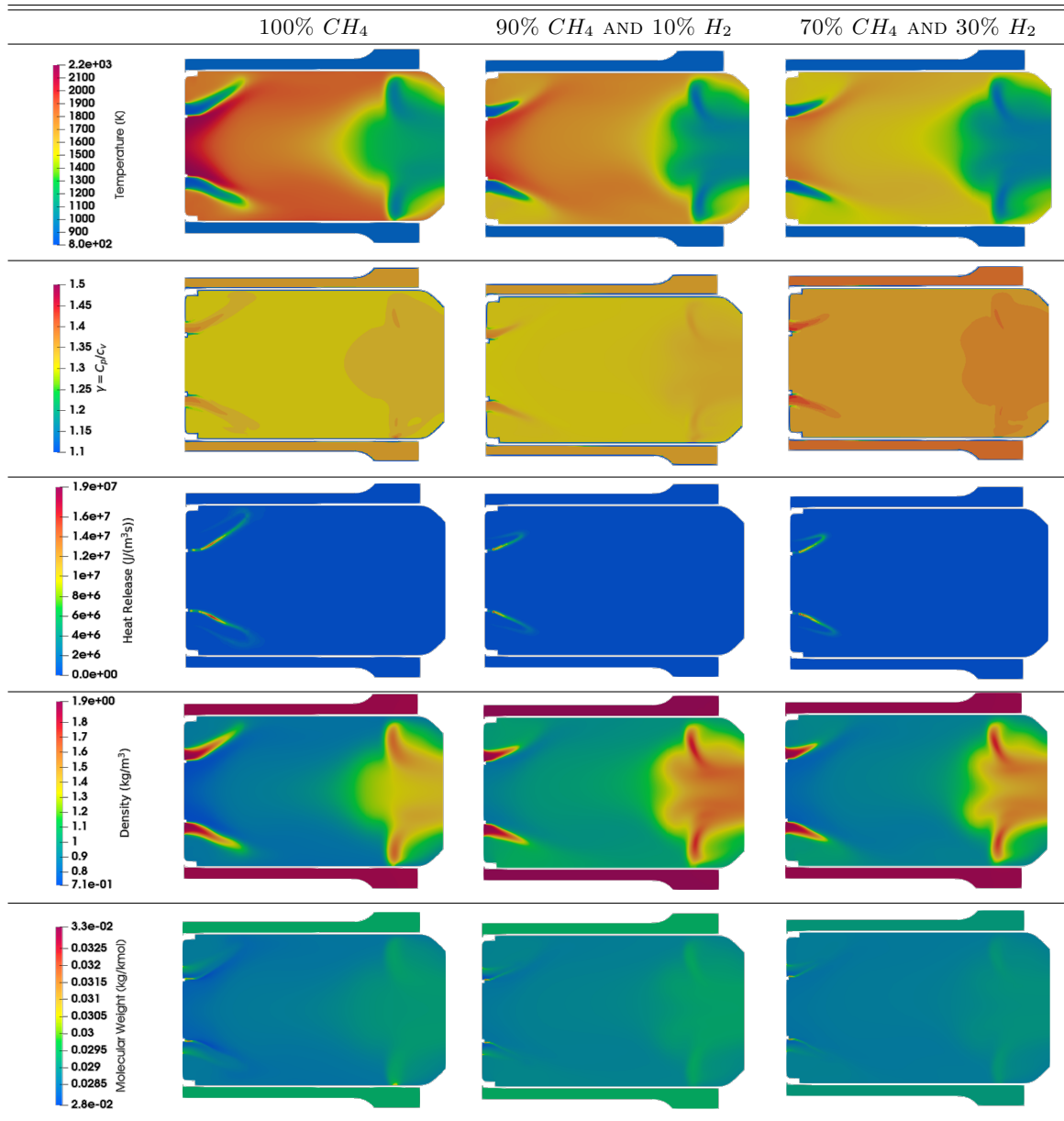
Table 7.7: Parameters of COMSOL Multiphysics<sup>®</sup> simulations of AE-T100 burner by using the field of fluid-dynamic quantities as parameters in main combustion chamber.

PARAMETERS	100% $CH_4$	90% $CH_4$ AND 10% $H_2$	70% $CH_4$ AND 30% $H_2$	UNITS
$T_{air}$	865	865	865	K
$T_{fuel}$	300	300	300	K
$T_{pilot}$	975	970.6	963.18	K
$\rho_{pilot}$	1.2336	1.2292	1.1938	$kg/m^3$
$c_{pilot}$	697.42	707.9	741.3	m/s
$p$	$4 \times 10^5$	$4 \times 10^5$	$4 \times 10^5$	Pa
$MW_{pilot}$	0.025	0.0284	0.0239	kg/mol

The conditions in the main combustion chamber have been interpolated, from CFD simulations, on the COMSOL mesh in order to develop the distributed fields of fluid dynamic properties. These fields are used in monopole source in COMSOL Multiphysics<sup>®</sup> in order to take into account the combustion process in the same way described in section 6.2. In OpenFOAM, through the command line that includes data processing, data on density, velocity magnitude, and Mach number in the combustion chamber obtained from CFD simulations have been extrapolated. By using the open-source post-processing software Paraview, it was possible to isolate the volume relative to the main combustion

chamber of the burner. The same software was used to calculate the fields the distributed fields of temperature, density, molecular weight, time delay, heat release, and the ratio between specific heat at constant pressure and constant volume  $\gamma = c_p/c_v$ , using filter calculator of Paraview.

Table 7.8: Fields of fluid-dynamic properties of the AE-T100 main combustion chamber interpolated on COMSOL Multiphysics<sup>®</sup>.



In Table 7.8 the fields used in the Helmholtz solver are summarized. For the AE-T100 burner, following [4, 88], an estimation of this time delay is computed using particle tracking techniques. From the injection point in the burner exit, particles are tracked and a time is computed until the flame front is reached. In order to follow this particle, it was necessary to convert the velocity field to point data using a filter of Paraview called

“Point Data to Cell Data”. Then, using the Stream Tracer tool, time was extrapolated. For all the nodes in which the fuel mass fraction is null, hence also the heat release is equal to zero,  $\tau$  is set equal to zero. In this way a distribution of time delay in combustion chamber has been obtained. These fields have been used in the monopole source defined in COMSOL. In this AE-T100 burner the driving mechanism that mostly leads to the establishment of thermoacoustic instability is Equivalence ratio oscillations (see section 2.2).

## 7.8 Thermo-acoustic comparison between 100% $CH_4$ mixture vs $H_2$ - $CH_4$ blends

From this preliminary study, no big differences between the thermoacoustic behavior of AE-T100 burner fueled by three different mixtures have been observed. There is a significant difference between the results of the AE-T100 burner fueled by pure methane mixture simulated using the fields created by the RANS simulation and those created by the flame sheet model (compare the imaginary part of frequencies of Table 7.9 respect with Table 7.6).

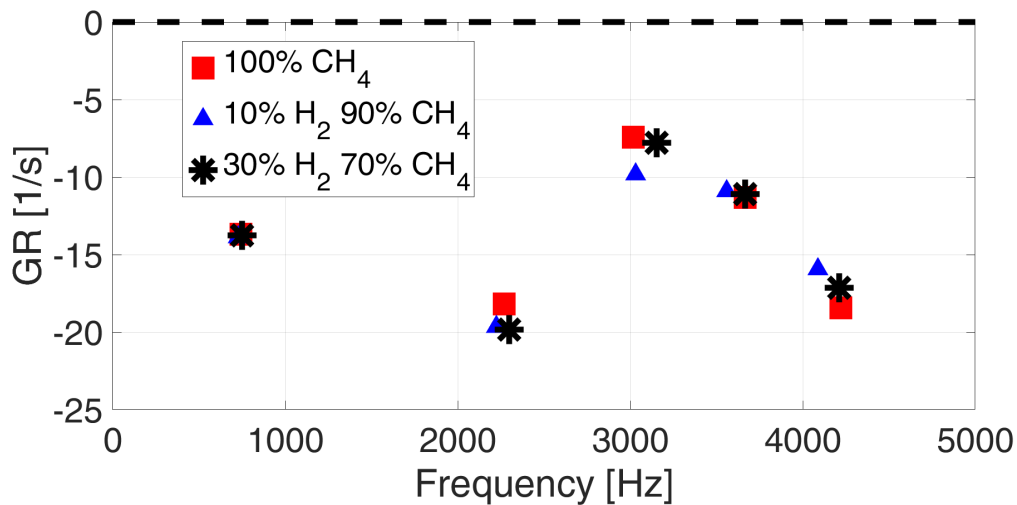
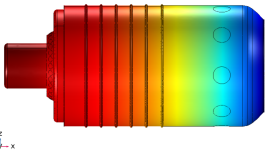
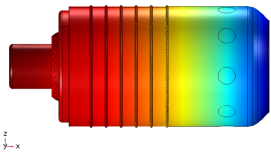
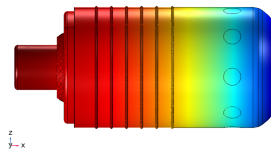
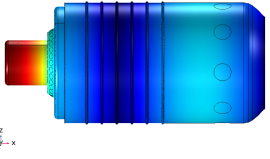
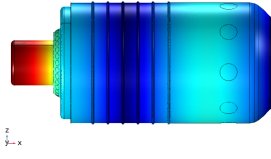
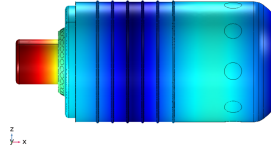
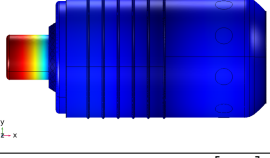
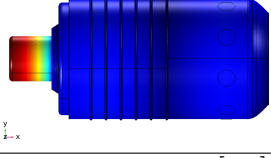
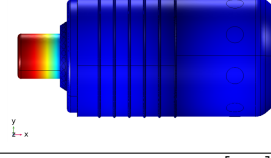
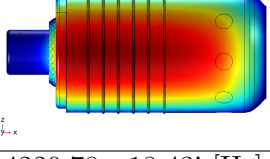
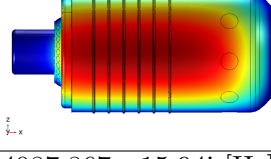
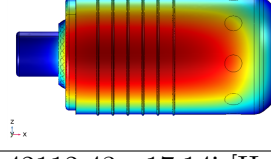
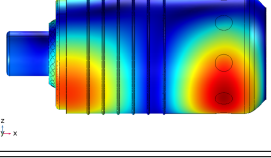
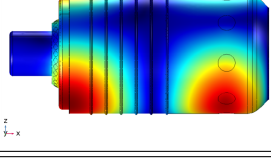
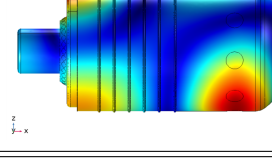


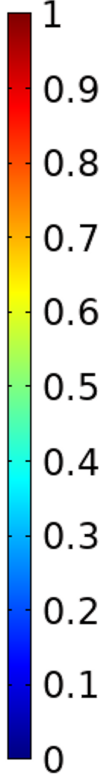
Figure 7.15: Frequency and Growth Rate for the AE-T100 burner fueled by three different mixtures.

The frequencies in the simulation using the flame sheet are all unstable, except the last one. On the contrary, the frequencies are all stable in the simulation in which the fields estimated from the CFD simulation were employed to account for the combustion process parameters. Table 7.9 shows the acoustic pressure normalized by the max value between the burner fueled by the three different mixtures. There is no significant difference between the three mixtures because the content of hydrogen is very low and does not lead to a significant change in flame shape. Additionally, Fig. 7.15 demonstrates that there are minimal variations in the frequencies and growth rates of the burners powered by the three different mixtures.

Table 7.9: First five modes of AE-T100 fueled by three mixtures.

MODE	100% $CH_4$	90% $CH_4$ AND 10% $H_2$	70% $CH_4$ AND 30% $H_2$
I	747.84 - 13.68i [Hz] 	727.57 - 13.87i [Hz] 	748.91 - 13.76i [Hz] 
II	2267.81 - 18.18i [Hz] 	2224.06 - 19.66i [Hz] 	2297.87 - 19.83i [Hz] 
III	3018.04 - 7.44i [Hz] 	3031.35 - 9.82i [Hz] 	3152.82 - 7.79i [Hz] 
IV	3666.24 - 10.27i [Hz] 	3559.01 - 10.90i [Hz] 	3657.06 - 11.09i [Hz] 
V	4220.78 - 18.43i [Hz] 	4087.867 - 15.94i [Hz] 	42112.43 - 17.14i [Hz] 

**[p/p<sub>max</sub>]**





# Conclusions

The study discussed in this thesis has drawn attention to the effects of hydrogen or a mixture of methane and hydrogen in gas turbine and micro gas turbine burners in terms of fluid-dynamic properties and thermoacoustic behavior. In order to carry out the CFD simulations on a burner fueled by different mixtures, different codes have been used (Ansys Fluent, OpenFOAM). Investigations have been done about how various flame stabilization procedures affect mixtures of hydrogen-enriched methane or hydrogen-air. In order to assess the fluid-dynamic quantity distributions in the combustion chamber, the fields of fluid-dynamic properties from these RANS simulations have been interpolated on the mesh of the Helmholtz solver (module Acoustic Pressure and Frequency Domain of COMSOL Multiphysics<sup>®</sup>). The parameters that affect thermoacoustic simulations have been accurately analyzed. In order to validate the 3D FEM simulations, a comparison between various thermoacoustic codes has been developed. In general, the LHV of hydrogen affects burner behavior due to the higher temperature in the combustion chamber. The comparison of mixtures is done in this study maintaining constant mass flow rate of air and thermal power for each type of burner. This causes the distribution of equivalence ratio and velocity of the various mixtures in the combustion chamber to shift. This difference in distribution fields affects the interplay between pressure fluctuations and heat release fluctuations and, as a result, the thermoacoustic behavior of various mixtures. The outcomes of the investigation into several burners are given in the summary that follows.

- **Simulations on Louisiana University laboratory burner:** The analysis of the cold flow of the hydrogen-methane mixture-fueled burner shows a larger gradient of equivalence ratio in the radial direction than the burner fueled by pure methane mixture. Regarding the reaction case, the pollutant of  $CO_2$  in the case fueled by methane enriched with 30%<sub>v</sub> of hydrogen decreased by around 10% compared to the case fueled by 100% methane mixture.
- **Simulations on Vanderbilt University laboratory burner:** The difference in flame topology and velocity that affects the temperature and recirculation zone downstream of the bluff body is highlighted by the CFD analysis between two mixtures of pure methane and pure hydrogen. The interaction of velocity fluctuations, beginning at the flame base with the flame front, is the process that mostly causes fluctuations of the heat release rate in premixed combustion. A convective time delay  $\tau$  can be used to describe this process. By taking this into account, RANS simulations were used to calculate the distributed time delay. Thermoacoustic investigation of the burner, using two different fuel mixtures, has highlighted the increase in instability in the case of using hydrogen-air mixture as fuel.



- **Simulations on micro-turbine AE-T100 burner:** By comparing three combinations (100% $CH_4$ , 90% $CH_4 - 10\%H_2$ , and 70% $CH_4 - 30\%H_2$ ) using CFD, the main changes were discovered in temperature and equivalence ratio contours because the flame becomes leaner as the hydrogen content increases. For the burner fueled by the three distinct mixtures, thermoacoustic research found no significant changes in the stability of the modes.

A numerical analysis on the ability of burners built to burn methane fuel to work with hydrogen mixtures or blends of methane and hydrogen has been reported in this thesis. In conclusion, this thermoacoustic analysis of several burners has highlighted the substantial flexibility of the micro-turbine burner developed for methane-air fuel when mixtures enriched with hydrogen up to 30% $_v$  are used. The findings of this thesis are a suitable starting point for future investigations. These may include the development of a Flame Transfer Function, in order to forecast in a more precise way the thermoacoustic response of these burners.

# References

- [1] L. Crocco, S.-I. Cheng, Theory of combustion instability in liquid propellant rocket motors, Tech. rep., Princeton Univ Nj (1956).
- [2] D. Laera, P. W. Agostinelli, L. Selle, Q. Cazères, G. Oztarlik, T. Schuller, L. Gicquel, T. Poinsot, Stabilization mechanisms of ch4 premixed swirled flame enriched with a non-premixed hydrogen injection, Proceedings of the Combustion Institute 38 (4) (2021) 6355–6363.
- [3] S. Camporeale, B. Fortunato, G. Campa, A finite element method for three-dimensional analysis of thermo-acoustic combustion instability, Journal of Engineering for Gas Turbines and Power 133 (1) (2011).
- [4] L. Davide, S. M. Camporeale, Numerical and experimental studies on self sustained thermo-acoustic combustion instabilities of an experimental rig for full-scale industrial burners, International Journal of Gas Turbine, Propulsion and Power Systems 9 (1) (2017) 37–46.
- [5] S. R. Stow, A. P. Dowling, Low-order modelling of thermoacoustic limit cycles, in: Turbo Expo: Power for Land, Sea, and Air, Vol. 41669, 2004, pp. 775–786.
- [6] S. p. Evesque, W. Polifke, Low-order acoustic modelling for annular combustors: validation and inclusion of modal coupling, in: Turbo Expo: Power for Land, Sea, and Air, Vol. 36061, 2002, pp. 321–331.
- [7] A. Andreini, B. Facchini, L. Mangani, F. Simonetti, Development and validation of a 1-d tool for thermoacoustic instabilities analysis in gas turbine combustors, in: Turbo Expo: Power for Land, Sea, and Air, Vol. 43130, 2008, pp. 951–960.
- [8] P. Moin, S. V. Apte, Large-eddy simulation of realistic gas turbine combustors, AIAA journal 44 (4) (2006) 698–708.
- [9] G. Boudier, L. Gicquel, T. Poinsot, D. Bissieres, C. Bérat, Comparison of les, rans and experiments in an aeronautical gas turbine combustion chamber, Proceedings of the Combustion Institute 31 (2) (2007) 3075–3082.
- [10] A. Sengissen, J. Van Kampen, R. Huls, G. G. Stoffels, J. B. Kok, T. Poinsot, Les and experimental studies of cold and reacting flow in a swirled partially premixed burner with and without fuel modulation, Combustion and Flame 150 (1-2) (2007) 40–53.
- [11] G. Staffelbach, L. Gicquel, G. Boudier, T. Poinsot, Large eddy simulation of self excited azimuthal modes in annular combustors, Proceedings of the Combustion Institute 32 (2) (2009) 2909–2916.

- [12] P. Wolf, R. Balakrishnan, G. Staffelbach, L. Y. Gicquel, T. Poinso, Using les to study reacting flows and instabilities in annular combustion chambers, *Flow, turbulence and combustion* 88 (1) (2012) 191–206.
- [13] F. Nicoud, L. Benoit, C. Sensiau, T. Poinso, Acoustic modes in combustors with complex impedances and multidimensional active flames, *AIAA journal* 45 (2) (2007) 426–441.
- [14] D. Laera, S. M. Camporeale, A weakly nonlinear approach based on a distributed flame describing function to study the combustion dynamics of a full-scale lean-premixed swirled burner, *Journal of Engineering for Gas Turbines and Power* 139 (9) (2017).
- [15] V. Ceglie, T. Capurso, P. Oresta, S. M. Camporeale, Analysis of the influence of the mean flow field mach number on thermo-acoustic combustion instability, in: *E3S Web of Conferences*, Vol. 197, EDP Sciences, 2020, p. 11004.
- [16] Irena, *Global renewables outlook: Energy transformation 2050* (2020).
- [17] M. Olczak, A. Piebalgs, *Sector coupling: the new eu climate and energy paradigm?* (2018).
- [18] J. LISELOTTE, *Cop27 climate change conference in egypt* (2022).
- [19] D. Gielen, R. Gorini, N. Wagner, R. Leme, L. Gutierrez, G. Prakash, E. Asmelash, L. Janeiro, G. Gallina, G. Vale, et al., *Global energy transformation: a roadmap to 2050* (2019).
- [20] L. Van Nuffel, J. G. Dedecca, T. Smit, K. Rademaekers, *Sector coupling: how can it be enhanced in the EU to foster grid stability and decarbonise?*, European Parliaent Brussels, Belgium, 2018.
- [21] P. Kutne, *The path towards a zero-carbon gas turbine*, Tech. rep., European Turbine Network (ETN Global) (2020).
- [22] M. Stefanizzi, T. Capurso, G. Filomeno, M. Torresi, G. Pascazio, Recent combustion strategies in gas turbines for propulsion and power generation toward a zero-emissions future: Fuels, burners, and combustion techniques, *Energies* 14 (20) (2021) 6694.
- [23] T. Capurso, M. Stefanizzi, M. Torresi, S. Camporeale, Perspective of the role of hydrogen in the 21st century energy transition, *Energy Conversion and Management* 251 (2022) 114898.
- [24] L. Chen, Z. Qi, S. Zhang, J. Su, G. A. Somorjai, Catalytic hydrogen production from methane: A review on recent progress and prospect, *Catalysts* 10 (8) (2020) 858.
- [25] S. Taamallah, K. Vogiatzaki, F. M. Alzahrani, E. M. Mokheimer, M. Habib, A. F. Ghoniem, Fuel flexibility, stability and emissions in premixed hydrogen-rich gas turbine combustion: Technology, fundamentals, and numerical simulations, *Applied energy* 154 (2015) 1020–1047.

- [26] P. Griebel, Gas turbines and hydrogen, *Hydrogen Science and Engineering: Materials, Processes, Systems and Technology* (2016) 1011–1032.
- [27] P. Jansohn, Overview of gas turbine types and applications, in: *Modern Gas Turbine Systems*, Elsevier, 2013, pp. 21–43.
- [28] J. Goldmeer, Fuel flexible gas turbines as enablers for a low or reduced carbon energy ecosystem, *Electrify Europe: Vienna, Austria* (2018).
- [29] G. Gahleitner, Hydrogen from renewable electricity: An international review of power-to-gas pilot plants for stationary applications, *international Journal of hydrogen energy* 38 (5) (2013) 2039–2061.
- [30] R. Winkler-Goldstein, A. Rastetter, Power to gas: the final breakthrough for the hydrogen economy?, *Green* 3 (1) (2013) 69–78.
- [31] L. Figura, J. G. Lee, B. D. Quay, D. A. Santavicca, The effects of fuel composition on flame structure and combustion dynamics in a lean premixed combustor, in: *Turbo Expo: Power for Land, Sea, and Air*, Vol. 47918, 2007, pp. 181–187.
- [32] T. Lieuwen, V. McDonell, D. Santavicca, T. Sattelmayer, Burner development and operability issues associated with steady flowing syngas fired combustors, *Combustion Science and Technology* 180 (6) (2008) 1169–1192.
- [33] S. Shanbhogue, Y. Sanusi, S. Taamallah, M. Habib, E. Mokheimer, A. Ghoniem, Flame macrostructures, combustion instability and extinction strain scaling in swirl-stabilized premixed  $\text{CH}_4/\text{H}_2$  combustion, *Combustion and Flame* 163 (2016) 494–507.
- [34] R. W. Schefer, D. Wicksall, A. K. Agrawal, Combustion of hydrogen-enriched methane in a lean premixed swirl-stabilized burner, *Proceedings of the combustion institute* 29 (1) (2002) 843–851.
- [35] A. Lantz, R. Collin, M. Aldén, A. Lindholm, J. Larfeldt, D. Lörstad, Investigation of hydrogen enriched natural gas flames in a sgt-700/800 burner using oh plif and chemiluminescence imaging, *Journal of Engineering for Gas Turbines and Power* 137 (3) (2015).
- [36] A. Subash, H. Kim, S. Moller, M. Richter, C. Brackmann, M. Alden, A. Lantz, A. Lindholm, J. Larfeldt, D. Lorstad, Investigation of fuel and load flexibility in a sgt-600/700/800 burner under atmospheric pressure conditions using high-speed oh-plif and oh chemiluminescence imaging, in: *ASME Turbo Expo 2020: Turbomachinery Technical Conference and Exposition*, 2021.
- [37] K. T. Kim, J. G. Lee, H. J. Lee, B. D. Quay, D. A. Santavicca, Characterization of forced flame response of swirl-stabilized turbulent lean-premixed flames in a gas turbine combustor, *Journal of engineering for gas turbines and power* 132 (4) (2010).
- [38] T. F. Guiberti, D. Durox, P. Scouflaire, T. Schuller, Impact of heat loss and hydrogen enrichment on the shape of confined swirling flames, *Proceedings of the Combustion Institute* 35 (2) (2015) 1385–1392.

- [39] J. Beita, M. Talibi, S. Sadasivuni, R. Balachandran, Thermoacoustic instability considerations for high hydrogen combustion in lean premixed gas turbine combustors: A review, *Hydrogen* 2 (1) (2021) 33–57.
- [40] M. C. Janus, G. A. Richards, M. J. Yip, E. H. Robey, Effects of ambient conditions and fuel composition on combustion stability, in: *Turbo Expo: Power for Land, Sea, and Air*, Vol. 78699, American Society of Mechanical Engineers, 1997, p. V002T06A035.
- [41] E. Æsøy, J. G. Aguilar, S. Wiseman, M. R. Bothien, N. A. Worth, J. R. Dawson, Scaling and prediction of transfer functions in lean premixed h<sub>2</sub>/ch<sub>4</sub>-flames, *Combustion and Flame* 215 (2020) 269–282.
- [42] D. Wicksall, A. Agrawal, Acoustics measurements in a lean premixed combustor operated on hydrogen/hydrocarbon fuel mixtures, *International Journal of Hydrogen Energy* 32 (8) (2007) 1103–1112.
- [43] B. Ahn, T. Indlekofer, J. Dawson, N. Worth, Transient thermo-acoustic responses of methane/hydrogen flames in a pressurized annular combustor, *Journal of Engineering for Gas Turbines and Power* 144 (1) (2022).
- [44] Y. Huang, V. Yang, Dynamics and stability of lean-premixed swirl-stabilized combustion, *Progress in energy and combustion science* 35 (4) (2009) 293–364.
- [45] S. Ducruix, T. Schuller, D. Durox, S. Candel, Combustion dynamics and instabilities: Elementary coupling and driving mechanisms, *Journal of propulsion and power* 19 (5) (2003) 722–734.
- [46] J. Zhang, A. Ratner, Experimental study on the excitation of thermoacoustic instability of hydrogen-methane/air premixed flames under atmospheric and elevated pressure conditions, *International Journal of Hydrogen Energy* 44 (39) (2019) 21324–21335.
- [47] O. Tuncer, S. Acharya, J. Uhm, Dynamics, nox and flashback characteristics of confined premixed hydrogen-enriched methane flames, *International Journal of hydrogen energy* 34 (1) (2009) 496–506.
- [48] T. García-Armingol, J. Ballester, Operational issues in premixed combustion of hydrogen-enriched and syngas fuels, *International Journal of Hydrogen Energy* 40 (2) (2015) 1229–1243.
- [49] T. C. Lieuwen, V. Yang, *Combustion instabilities in gas turbine engines: operational experience, fundamental mechanisms, and modeling*, American Institute of Aeronautics and Astronautics, 2005.
- [50] J. W. S. B. Rayleigh, *The theory of sound*, Vol. 2, Macmillan & Company, 1896.
- [51] M. L. Munjal, *Acoustics of ducts and mufflers with application to exhaust and ventilation system design*, John Wiley & Sons, 1987.
- [52] W. Polifke, *Combustion instabilities, von kármán institute lecture series* (2004).

- 
- [53] D. Kendrick, T. Anderson, W. Sowa, T. Snyder, Acoustic sensitivities of lean-premixed fuel injectors in a single nozzle rig (1999).
- [54] T. Lieuwen, H. Torres, C. Johnson, B. Zinn, A mechanism of combustion instability in lean premixed gas turbine combustors, *J. Eng. Gas Turbines Power* 123 (1) (2001) 182–189.
- [55] S. Candel, Combustion dynamics and control: progress and challenges, *Proceedings of the combustion institute* 29 (1) (2002) 1–28.
- [56] K. Schadow, E. Gutmark, Combustion instability related to vortex shedding in dump combustors and their passive control, *Progress in Energy and Combustion Science* 18 (2) (1992) 117–132.
- [57] T. J. Poinso, A. C. Trouve, D. P. Veynante, S. M. Candel, E. J. Esposito, Vortex-driven acoustically coupled combustion instabilities, *Journal of fluid mechanics* 177 (1987) 265–292.
- [58] K. I. Matveev, F. Culick, A model for combustion instability involving vortex shedding, *Combustion Science and Technology* 175 (6) (2003) 1059–1083.
- [59] M. Peters, A. Hirschberg, A. Reijnen, A. Wijnands, Damping and reflection coefficient measurements for an open pipe at low mach and low helmholtz numbers, *Journal of Fluid Mechanics* 256 (1993) 499–534.
- [60] D. Ronneberger, C. Ahrens, Wall shear stress caused by small amplitude perturbations of turbulent boundary-layer flow: an experimental investigation, *Journal of Fluid Mechanics* 83 (3) (1977) 433–464.
- [61] T. Poinso, D. Veynante, *Theoretical and numerical combustion*, RT Edwards, Inc., 2005.
- [62] F. Culick, Some recent results for nonlinear acoustics in combustion chambers, *AIAA journal* 32 (1) (1994) 146–169.
- [63] A. P. Dowling, S. R. Stow, Acoustic analysis of gas turbine combustors, *Journal of propulsion and power* 19 (5) (2003) 751–764.
- [64] W. Krebs, H. Krediet, E. Portillo, S. Hermeth, T. Poinso, S. Schimek, O. Paschereit, Comparison of nonlinear to linear thermoacoustic stability analysis of a gas turbine combustion system, *Journal of Engineering for Gas Turbines and Power* 135 (8) (2013).
- [65] S. H. Strogatz, *Nonlinear dynamics and chaos: with applications to physics, Biology, Chemistry and Engineering* (1994) 1.
- [66] F. Nicoud, K. Wiczeorek, About the zero mach number assumption in the calculation of thermoacoustic instabilities, *International journal of spray and combustion dynamics* 1 (1) (2009) 67–111.
- [67] A. P. Dowling, The calculation of thermoacoustic oscillations, *Journal of sound and vibration* 180 (4) (1995) 557–581.

- [68] S. Hermeth, G. Staffelbach, L. Y. Gicquel, V. Anisimov, C. Cirigliano, T. Poinsot, Bistable swirled flames and influence on flame transfer functions, *Combustion and Flame* 161 (1) (2014) 184–196.
- [69] A. P. Dowling, Nonlinear self-excited oscillations of a ducted flame, *Journal of fluid mechanics* 346 (1997) 271–290.
- [70] J. Li, A. S. Morgans, Time domain simulations of nonlinear thermoacoustic behaviour in a simple combustor using a wave-based approach, *Journal of Sound and Vibration* 346 (2015) 345–360.
- [71] K. Balachandran, Fundamentals of gas turbine combustor thermo-acoustics, von kármán institute lecture series (2010).
- [72] H. Merk, Analysis of heat-driven oscillations of gas flows, *Applied Scientific Research, Section A* 6 (4) (1957) 317–336.
- [73] G. Bloxsidge, A. Dowling, P. Langhorne, Reheat buzz: an acoustically coupled combustion instability. part 2. theory, *Journal of Fluid mechanics* 193 (1988) 445–473.
- [74] M. A. Heckl, Active control of the noise from a rijke tube, *Journal of Sound and Vibration* 124 (1) (1988) 117–133.
- [75] J. J. Keller, Thermoacoustic oscillations in combustion chambers of gas turbines, *AIAA journal* 33 (12) (1995) 2280–2287.
- [76] T. C. Lieuwen, Experimental investigation of limit-cycle oscillations in an unstable gas turbine combustor, *Journal of Propulsion and Power* 18 (1) (2002) 61–67.
- [77] F. Giuliani, P. Gajan, O. Diers, M. Ledoux, Influence of pulsed entries on a spray generated by an air-blast injection device: An experimental analysis on combustion instability processes in aeroengines, *Proceedings of the combustion institute* 29 (1) (2002) 91–98.
- [78] S. R. Stow, A. P. Dowling, Thermoacoustic oscillations in an annular combustor, in: *Turbo Expo: Power for Land, Sea, and Air*, Vol. 78514, American Society of Mechanical Engineers, 2001, p. V002T02A004.
- [79] G. Campa, S. M. Camporeale, A. s. Guaus, J. Favier, M. Bargiacchi, A. Bottaro, E. Cosatto, G. Mori, A quantitative comparison between a low order model and a 3d fem code for the study of thermoacoustic combustion instabilities, in: *Turbo Expo: Power for Land, Sea, and Air*, Vol. 54624, 2011, pp. 859–869.
- [80] D. Bohn, E. Deuker, An acoustical model to predict combustion driven oscillations (1993).
- [81] A. P. Dowling, A kinematic model of a ducted flame, *Journal of fluid mechanics* 394 (1999) 51–72.
- [82] T. Schuller, D. Durox, P. Palies, S. Candel, Acoustic decoupling of longitudinal modes in generic combustion systems, *Combustion and Flame* 159 (5) (2012) 1921–1931.

- [83] J.-F. Parmentier, P. Salas, P. Wolf, G. Staffelbach, F. Nicoud, T. Poinso, A simple analytical model to study and control azimuthal instabilities in annular combustion chambers, *Combustion and Flame* 159 (7) (2012) 2374–2387.
- [84] M. Bauerheim, J.-F. Parmentier, P. Salas, F. Nicoud, T. Poinso, An analytical model for azimuthal thermoacoustic modes in an annular chamber fed by an annular plenum, *Combustion and Flame* 161 (5) (2014) 1374–1389.
- [85] M. Heckl, A new perspective on the flame describing function of a matrix flame, *International Journal of Spray and Combustion Dynamics* 7 (2) (2015) 91–112.
- [86] J.-F. Bourgouin, D. Durox, J. Moeck, T. Schuller, S. Candel, A new pattern of instability observed in an annular combustor: The slanted mode, *Proceedings of the Combustion Institute* 35 (3) (2015) 3237–3244.
- [87] L. Li, X. Sun, Effect of vorticity waves on azimuthal instabilities in annular chambers, *Combustion and Flame* 162 (3) (2015) 628–641.
- [88] G. Campa, S. M. Camporeale, Prediction of the thermoacoustic combustion instabilities in practical annular combustors, *Journal of Engineering for Gas Turbines and Power* 136 (9) (2014).
- [89] A. Cuquel, C. Silva, F. Nicoud, D. Durox, T. Schuller, Prediction of the non-linear dynamics of a multiple flame combustor by coupling the describing function methodology with a helmholtz solver, in: *Turbo Expo: Power for Land, Sea, and Air*, Vol. 55119, American Society of Mechanical Engineers, 2013, p. V01BT04A049.
- [90] A. Comsol, Comsol multiphysics user’s guide, Version: September 10 (2005) 333.
- [91] R. B. Lehoucq, D. C. Sorensen, C. Yang, *ARPACK users’ guide: solution of large-scale eigenvalue problems with implicitly restarted Arnoldi methods*, SIAM, 1998.
- [92] C. Martin, L. Benoit, F. Nicoud, T. Poinso, Analysis of acoustic energy and modes in a turbulent swirled combustor, in: *Proceedings of the summer program, 2004*, pp. 377–394.
- [93] A. Giaque, L. SELLE, L. Gicquel, T. Poinso, H. Buechner, P. Kaufmann, W. Krebs, System identification of a large-scale swirled partially premixed combustor using les and measurements, *Journal of Turbulence* (6) (2005) N21.
- [94] C. E. Martin, L. Benoit, Y. Sommerer, F. Nicoud, T. Poinso, Large-eddy simulation and acoustic analysis of a swirled staged turbulent combustor, *AIAA journal* 44 (4) (2006) 741–750.
- [95] L. Selle, L. Benoit, T. Poinso, F. Nicoud, W. Krebs, Joint use of compressible large-eddy simulation and helmholtz solvers for the analysis of rotating modes in an industrial swirled burner, *Combustion and Flame* 145 (1-2) (2006) 194–205.
- [96] J. Gikadi, T. Sattelmayer, A. Peschiulli, Effects of the mean flow field on the thermo-acoustic stability of aero-engine combustion chambers, in: *Turbo Expo: Power for Land, Sea, and Air*, Vol. 44687, American Society of Mechanical Engineers, 2012, pp. 1203–1211.



- [97] G. Campa, Prediction of the thermoacoustic combustion instability in gas turbines, Ph.D. thesis (2012).
- [98] J. Li, D. Yang, C. Luzzato, A. S. Morgans, Open source combustion instability low order simulator (oscilos-long) technical report (2015).
- [99] G. Campa, S. Camporeale, A novel fem method for predicting thermoacoustic combustion instability, in: European COMSOL Conference, 2009.
- [100] A. Innocenti, A. Andreini, B. Facchini, M. Cerutti, Numerical analysis of the dynamic flame response and thermo-acoustic stability of a full-annular lean partially-premixed combustor, in: Turbo Expo: Power for Land, Sea, and Air, Vol. 49767, American Society of Mechanical Engineers, 2016, p. V04BT04A003.
- [101] C. Pankiewitz, T. Sattelmayer, Time domain simulation of combustion instabilities in annular combustors, *J. Eng. Gas Turbines Power* 125 (3) (2003) 677–685.
- [102] M. Stefanizzi, S. Stefanizzi, V. Ceglie, T. Capurso, M. Torresi, S. M. Camporeale, Analysis of the partially premixed combustion in a lab-scale swirl-stabilized burner fueled by a methane-hydrogen mixture, in: E3S Web of Conferences, Vol. 312, EDP Sciences, 2021, p. 11004.
- [103] V. Ceglie, M. Stefanizzi, T. Capurso, F. Fornarelli, S. M. Camporeale, Thermoacoustic combustion stability analysis of a bluff body-stabilized burner fueled by methane-air and hydrogen-air mixtures, *Energies* 16 (7) (2023) 3272.
- [104] O. Tuncer, S. Acharya, J. H. Uhm, Effects of hydrogen enrichment on confined methane flame behavior, in: ASME Power Conference, Vol. 42053, 2006, pp. 465–476.
- [105] A. De, S. Acharya, Dynamics of upstream flame propagation in a hydrogen-enriched premixed flame, *International journal of hydrogen energy* 37 (22) (2012) 17294–17309.
- [106] A. De, S. Zhu, S. Acharya, An experimental and computational study of a swirl-stabilized premixed flame, in: Turbo Expo: Power for Land, Sea, and Air, Vol. 48838, 2009, pp. 951–968.
- [107] C. Bowman, R. Hanson, D. Davidson, J. Gardiner, V. Lissianski, G. Smith, D. Golden, M. Frenklach, M. Goldenberg, *Gri-mech 2.11*. 1999, URL: <http://www.me.berkeley.edu/gri-mech>.
- [108] G. P. Smith, *Gri-mech 3.0*, [http://www.me.berkeley.edu/gri\\_mech/](http://www.me.berkeley.edu/gri_mech/) (1999).
- [109] D. Mira, O. Lehmkuhl, A. Both, P. Stathopoulos, T. Tanneberger, T. G. Reichel, C. O. Paschereit, M. Vázquez, G. Houzeaux, Numerical characterization of a pre-mixed hydrogen flame under conditions close to flashback, *Flow, Turbulence and Combustion* 104 (2) (2020) 479–507.
- [110] J. Pan, M. Vangsness, D. Ballal, Aerodynamics of bluff-body stabilized confined turbulent premixed flames (1992).

- [111] S. Nandula, R. Pitz, R. Barlow, G. Fiechtner, Rayleigh/Raman/LIF measurements in a turbulent lean premixed combustor, in: 34th Aerospace Sciences Meeting and Exhibit, 1996, p. 937.
- [112] S. Cannon, B. Brewster, L. Smoot, Pdf modeling of lean premixed combustion using in situ tabulated chemistry, *Combustion and flame* 119 (3) (1999) 233–252.
- [113] A. Andreini, C. Bianchini, A. Innocenti, Large eddy simulation of a bluff body stabilized lean premixed flame, *Journal of Combustion* 2014 (2014).
- [114] A. Sudarma, RANS numerical simulation of lean premixed bluff body stabilized combustor: Comparison of turbulence models, *Journal of Thermal Engineering* 3 (6) (2017) 1561–1573.
- [115] F. R. Menter, Two-equation eddy-viscosity turbulence models for engineering applications, *AIAA journal* 32 (8) (1994) 1598–1605.
- [116] Ansys Fluent Theory Guide, ANSYS, Inc., 2022.
- [117] J. G. Aguilar, E. Aesøy, J. R. Dawson, The influence of hydrogen on the stability of a perfectly premixed combustor, *Combustion and Flame* 245 (2022) 112323.
- [118] D. Durox, T. Schuller, S. Candel, Combustion dynamics of inverted conical flames, *Proceedings of the combustion Institute* 30 (2) (2005) 1717–1724.
- [119] M. Gatti, R. Gaudron, C. Mirat, L. Zimmer, T. Schuller, Impact of swirl and bluff-body on the transfer function of premixed flames, *Proceedings of the Combustion Institute* 37 (4) (2019) 5197–5204.
- [120] P. Alemela, D. Fanaca, C. Hirsch, T. Sattelmayer, B. Schuermans, Determination and scaling of thermo acoustic characteristics of premixed flames, *International journal of spray and combustion dynamics* 2 (2) (2010) 169–198.
- [121] E. Lo Schiavo, D. Laera, E. Riber, L. Gicquel, T. Poinsot, On the impact of fuel injection angle in Euler-Lagrange large eddy simulations of swirling spray flames exhibiting thermoacoustic instabilities, *Combustion and Flame* 227 (2021) 359–370.
- [122] L. Magri, M. P. Juniper, J. P. Moeck, Sensitivity of the Rayleigh criterion in thermoacoustics, *Journal of Fluid Mechanics* 882 (2020).
- [123] AE-T100NG: Technical description, <http://ariatermo.com/wp-content/uploads/2016/06/Ansaldo-Energia.pdf>.
- [124] W. De Paepe, M. Montero Carrero, S. Bram, A. Parente, F. Contino, Towards higher micro gas turbine efficiency and flexibility: Humidified mgts—a review, *Turbo Expo: Power for Land, Sea, and Air* 50831 (2017) V003T06A030.
- [125] A. Pappa, L. Brieteux, P. Bénard, W. De Paepe, Can water dilution avoid flashback on a hydrogen-enriched micro-gas turbine combustion?—a large eddy simulations study, *Journal of Engineering for Gas Turbines and Power* 143 (4) (2021).

- [126] J. Bompas, A. Pappa, W. De Paepe, Analysis of combustion performance of non-conventional syngas in mgt combustor: Assessment of the impact of the quality of synthesis gas towards flame stability and emissions, in: Turbo Expo: Power for Land, Sea, and Air, Vol. 86052, American Society of Mechanical Engineers, 2022, p. V007T18A019.
- [127] W. De Paepe, M. Montero Carrero, S. Giorgetti, A. Parente, S. Bram, F. Contino, Exhaust gas recirculation on humidified flexible micro gas turbines for carbon capture applications, in: Turbo Expo: Power for Land, Sea, and Air, Vol. 49743, American Society of Mechanical Engineers, 2016, p. V003T06A011.
- [128] ESI-OpenCFD, OpenCFDLtd, <https://www.openfoam.com/news/main-news/openfoam-v2212>.
- [129] L. Giuntini, C. Galletti, A. Parente, Feeding h<sub>2</sub> admixtures in a micro-gas turbine: A cfd study, Proceedings of Global Power and Propulsion Society (2021).
- [130] S. B. Pope, S. B. Pope, Turbulent flows, Cambridge university press, 2000.
- [131] F. Contino, H. Jeanmart, T. Lucchini, G. D'Errico, Coupling of in situ adaptive tabulation and dynamic adaptive chemistry: An effective method for solving combustion in engine simulations, Proceedings of the Combustion Institute 33 (2) (2011) 3057–3064.
- [132] A. De Santis, D. B. Ingham, L. Ma, M. Pourkashanian, Cfd analysis of exhaust gas recirculation in a micro gas turbine combustor for co<sub>2</sub> capture, Fuel 173 (2016) 146–154.

# Publications

## Journal paper:

- V. Ceglie, M. Stefanizzi, T. Capurso, F. Fornarelli, S. M. Camporeale, Thermoacoustic Combustion Stability Analysis of a Bluff Body-Stabilized Burner Fueled by Methane–Air and Hydrogen–Air Mixtures, *Energies* 16 (7) (2023) 3207.

## Conferences paper:

- M. Stefanizzi, S. Stefanizzi, V. Ceglie, T. Capurso, M. Torresi, S. M. Camporeale, Analysis of the partially premixed combustion in a lab-scale swirl-stabilized burner fueled by a methane-hydrogen mixture, in: *E3S Web of Conferences*, Vol. 312, EDP Sciences, 2021, p. 11004.
- T. Capurso, V. Ceglie, F. Fornarelli, M. Torresi, S. M. Camporeale, CFD analysis of the combustion in the BERL burner fueled with a hydrogen-natural gas mixture, in: *E3S Web of Conferences*, Vol. 197, EDP Sciences, 2020, p. 10002.
- V. Ceglie, T. Capurso, P. Oresta, S. M. Camporeale, Analysis of the influence of the mean flow field mach number on thermo-acoustic combustion instability, in: *E3S Web of Conferences*, Vol. 197, EDP Sciences, 2020, p. 11004.



# Acknowledgments

This PhD work has been carried out in the Department of Mechanical, Mathematical and Management of the Politecnico di Bari (Italy). Part of it is also the result of a collaboration with the ANSALDO ENERGIA, (Genova, Italy). First of all, I would like to express my gratitude to Prof. S. M. Camporeale and Prof. Marco Torresi, advisors that gave me the possibility of this PhD. Thank you for your guide and for all the advises that you gave me during the last three years. I want also to thank the people of ANSALDO ENERGIA who worked with me on the CFD Simulation of turbo gas laboratory scale burners. In particular, a special thanks to Giovanni Campa of ANSALDO ENERGIA. Finally, I want to acknowledge Prof. Ward De Paepe for the possibility of the visiting period at the University of MONS (Belgium). Under his guidance I have learned a lot and confronted myself with very skilled people ready to help and advice me in every occasion. Special thanks also to Jérémy Bompas and Alessio Pappa for the support with the numerical results on burner of the AE-T100 micro gas turbine. Last but not least, I have to thank my family and my girlfriend Katia for always being there for me and for helping me all the time of my PhD. To the friends who have encouraged me over the years I owe my sincerest thanks. I won't be included you on the typical list of individuals to thank! I will shortly personally thank each of you if I haven't already done! I will remember the people I spent my working days at the Polytechnic University of Bari with, as well as the enjoyable time I spent outside the Campus with them.